DEVELOPMENT OF A LEAKAGE MODEL FOR SOLID OXIDE FUEL CELL COMPRESSIVE SEALS

A Dissertation
Presented to
The Academic Faculty

by

Christopher K. Green

In Partial Fulfillment
of the Requirements for the Degree
Doctor of Philosophy in the
School of Mechanical Engineering

Georgia Institute of Technology
December 2007

DEVELOPMENT OF A LEAKAGE MODEL FOR SOLID OXIDE FUEL CELL COMPRESSIVE SEALS

Approved by:

Dr. Jeffrey Streator, Advisor
School of Mechanical Engineering
Georgia Institute of Technology

Dr. Samuel Graham
School of Mechanical Engineering
Georgia Institute of Technology

Dr. Comas Haynes, Co-Advisor
Georgia Tech Research Institute
Georgia Institute of Technology

Dr. Meilin Liu
School of Material Science and Engineering
Georgia Institute of Technology

Dr. Richard Salant
School of Mechanical Engineering
Georgia Institute of Technology

Dr. Edgar Lara-Curzio
High Temperature Material Laboratory
Oak Ridge National Laboratory

Date Approved: November 12, 2007

ACKNOWLEDGEMENTS

I would like to express my sincere appreciation to my advisors, Dr. Jeffrey Streator and Dr. Comas Haynes, for their guidance and mentorship throughout this process. Dr. Streator forced me to question items more deeply in my quest for the “right answer”. In addition to his guidance, my co-advisor, Dr. Comas Haynes, has been very instrumental in ensuring that I was connected with the right people, and received the proper training to complete this endeavor.

Thanks also goes to my thesis reading committee members, Dr. Richard Salant, Dr. Samuel Graham, Dr. Meilin Liu, and Dr. Edgar Lara-Curzio, for offering suggestions for further developing this work. The High Temperature Materials Laboratory staff, especially Rosa Trejo, Randy Parten, Christine Goudy, and Dr. Edgar Lara-Curzio, has been critical component of the compressive seal leakage experiment development and execution as well as the material characterization. This work would have not been possible without my involvement in the High Temperature Materials Laboratory User Program at Oak Ridge National Laboratory.

I would also like to acknowledge support of this work from the Taiho Kogyo Tribology Research Fund.

I am forever indebted to my wife, Lorieal. She has been the primary reason I have been able to realize this achievement. This honor was made possible through her encouragement. Lastly, I would like thank my mother and father, who taught me to set my aspirations just beyond reach and with faith I can accomplish anything.

TABLE OF CONTENTS

LIST OF TABLES

LIST OF FIGURES

LIST OF SYMBOLS

A_k	nominal contact area
(A_r)	real contact area
c_{max}	unloaded maximum surface separation
C	integration constant
Δr	distance between adjacent nodes along r
h	surface separation
$h_{loss}(r)$	loss in surface separation at nodal location r
h_{max}	height of maximum asperity peak in nominal contact zone
$h(r)$	mean surface separation at radial distance r
E	elastic modulus
E^*	reduced elastic modulus of interface
$F(k_x,k_y)$	2D square FFT matrix
$\overline{F_k}$	load borne by a single asperity at frequency level k
G	normalized surface separation
i	imaginary number
$\nu_{1,2}$	Poisson ratios of bodies 1 and 2, respectively
$f(x,y)$	least squares plane
L	scan length
N_x	total number of sample points in x
N_y	total number of sample points in y

P	absolute fluid pressure (mixed lubrication model)
p_i	fluid pressure at the inner radius of the annulus
p_{mm}	average nodal contact pressure via macro model
p_o	fluid pressure at the outer radius of the annulus
$\bar{p}(r)$	mean pressure at radial location r
$p^*(r)$	pressure amplitude at radial location r
q	volumetric leakage rate
r'	dummy variable of integration
r_i	annulus inner radius
r_o	annulus outer radius
r	radial distance from origin
R	ideal gas constant
T	absolute temperature of fluid
V	volume of reservoir
V_{loss}	trapped volume loss
$z(x,y)$	raw surface profile
$\zeta(x,y)$	residual surface profile
β	FFT amplitude
Δ_k	amplitude of the residual profile at frequency level k
Δp	differential pressure
Δr	distance between adjacent nodes from macro model
u	dummy variable of integration
η	areal density of asperities at frequency level

σ	standard deviation of asperity heights
μ	dynamic viscosity
φ	transverse isotropic pressure flow factor
ρ	density of working fluid

Subscripts

f	furnace
j	index for radial nodes
k	frequency level
kv	known volume
c	critical value at onset of plastic deformation
ep	elastic plastic deformation

SUMMARY

Fuel cells represent a promising energy alternative to the traditional combustion of fossil fuels. In particular, solid oxide fuel cells (SOFCs) have been of interest due to their high energy densities and potential for stationary power applications. One of the key obstacles precluding the maturation and commercialization of planar SOFCs has been the absence of a robust sealant. A leakage computational model has been developed and refined in conjunction with leakage experiments and material characterization tests at Oak Ridge National Laboratory to predict leakage in a single interface metal-metal compressive seal assembly as well as multi-interface mica compressive seal assemblies.

The computational model consists of three submodels: a macroscopic model, a microscopic model, and a mixed lubrication model. The macroscopic model is a finite element representation of a preloaded compressive seal interface, which is used to ascertain macroscopic stresses and deformations. The micro scale contact mechanics model accounts for the role of surface roughness in determining the mean interfacial gap at each discretized node within the sealing interface. An averaged Reynolds equation derived from mixed lubrication theory is applied to approximate the leakage flow across the rough, annular interface. The composite model is applied as a predictive tool for assessing how certain parameters (i.e., temperature, applied compressive stress, surface finish, and elastic thermo physical properties) affect seal leakage rates.

1. INTRODUCTION

1.1. Description of Solid Oxide Fuel Cells

Fuel cells provide an innovative means of producing electricity by using substantially different principles from those used in the combustion of fossil fuels. Traditionally, fossil fuels are burned, and then a significant portion of the heat generated during the combustion process is converted into mechanical energy, which is ultimately converted into electrical energy. The balance is emitted into the environment as waste heat. Fuel cells, on the other hand, transform chemical energy directly into electrical energy. As a result, they offer a more energy efficient and environmentally friendly method of producing electricity than conventional power generation methods. Currently, the average coal–based power plant has an operating efficiency of approximately 35%, while fuel cell-hybrid systems are expected to have at a least a 50% efficiency in converting the energy stored in coal to electrical energy [1]. In addition to being inherently more efficient than traditional combustion processes, fuel cells offer the following advantages: modular construction, potential for cogeneration, high efficiency at partial loads and lower pollutant emissions [2].

Although there are a variety of fuel cells, this research will focus on the development of solid oxide fuel cells (SOFCs). SOFCs have received growing interest in the literature, because of the following salient features that distinguish them from other fuels cells: nonprecious metal composition, invariant electrolyte,

and high temperature operation (greater than 600°C). The use of a solid electrolyte inhibits the corrosion of constitutive fuel cell components. In addition, solid components may be sliced into very fine layers, which enable flexible configurations. High operating temperatures facilitate internal reforming and bolster reaction kinetics with relatively inexpensive materials.

Through a chemical reaction, SOFC's convert chemical energy into electrical energy. These cells operate similarly in principle to a battery except for the fact that the products and reactants employed to produce energy are constantly being replenished and are not allowed to deplete during operation. Each cell consists of three major parts: anode, electrolyte, and cathode. Hydrogen-rich fuel is continuously supplied to the porous anode, while air is supplied in a similar fashion to the cathode. To produce electricity, the air (oxidant) is reduced in the cathode, and oxide ions migrate across a dense permeable membrane- the electrolyte. Once the oxygen ions reach the anode, they react with hydrogen and oxidation occurs, which prompts the release of electrons to an external circuit. A depiction of the chemical reaction along with the direction of electron flow appears in Figure 1.

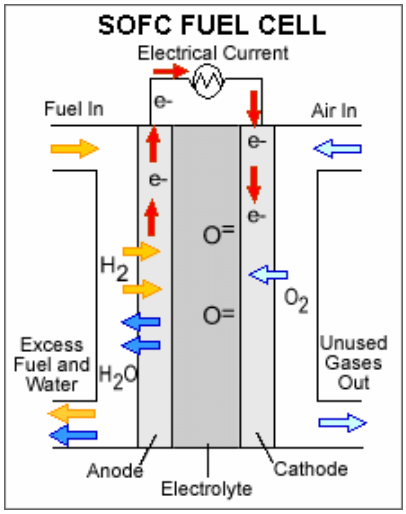

Figure 1: Depiction of Electrochemical Reaction in SOFC Fuel Cell [3]

The solid-state composition of SOFCs in theory allows for multiple configurations. Over the years, SOFCs have been assembled into ball-and-spigot, corrugated, tubular, and flat plate arrangements [4]. Nevertheless, in practice, SOFCs are most commonly manufactured in two arrangements: tubular and planar. The tubular configuration has the advantage of not requiring seals for operation. However, its power density and performance is limited mainly due to the long circumferential paths current must travel. The planar configuration, on the other hand, allows current to flow in series between neighboring cells. As a result, this configuration experiences fewer ohmic losses and ultimately yields higher power density than the tubular configuration. The planar, or flat plate, unit cell configuration also may be fabricated using techniques that are relatively inexpensive as compared to the tubular arrangement. To achieve acceptable operating voltages, the cells in each configuration must be "stacked" together; that is, the cells are arranged in series. A depiction of both the tubular and flat plate configurations is included as Figure 2.

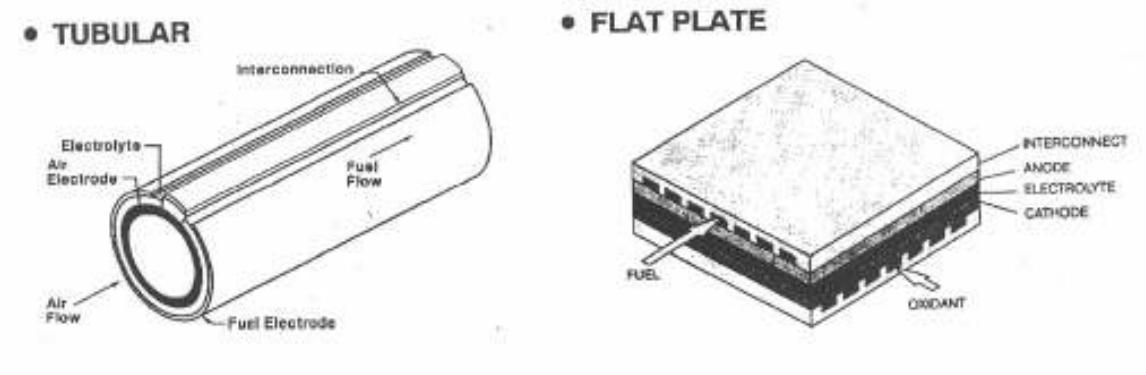

Figure 2: Depiction of Tubular and Flat Plate SOFC Configurations [5]

1.2. Mica Compressive Seals

The chief drawback to the planar configuration is the need for hermetic seals. SOFC seals have a variety of functions. Seals are required to electrically isolate the cells within the stack, provide mechanical bonding of stack components, prevent leakage of fuel and oxidant from the stack, and ensure separation of fuel and oxidant within the stack. Due to the adverse operating environment, stringent characteristics are required for candidate seal materials. SOFC seals must minimize coefficient of thermal expansion mismatch, maintain stability in extreme conditions (i.e., oxidizing, reducing, and humid environments), exhibit thermal shock resistance, be resilient to transient stresses that are present during startup and shutdown, and be both electrically and ionically nonconductive.

To ensure SOFCs maintain acceptable performance, several kinds of seals including metal-metal, metal-ceramic, and ceramic-ceramic, are required to withstand long durations (5000 to 40,000 hours) of thermal cycling at

temperatures as high as 1000 C. Of the aforementioned seal types, metal-metal seals are the most easily fabricated, but these seals are also the most susceptible to oxidation at high temperatures. Currently, metal-ceramic and ceramic-ceramic seals require the most development. Not only are the aforementioned much more difficult to manufacture than their metal-metal counterparts, but they also suffer from a loss of functionality over time due to the inherent brittle nature of ceramics [6].

As far as SOFC seal development is concerned, three approaches have dominated the literature: rigid glass, metallic brazes, and compressive seals. State-of-the-art planar SOFCs primarily utilize glass or are glass-ceramic based components for sealing. The aforementioned establish a seal by rigidly adhering components together. Although glass-ceramic seals are most often used in SOFC assemblies, the glass-ceramic sealing technology must overcome several technical challenges. Such seals become brittle and experience cracks below the glass transition temperature. In addition, the degradation of these seals facilitates interfacial reactions and solid-state diffusion, which inhibit electrolyte performance. Alternatively, researchers have been investigating the feasibility of mica based compressive, or preloaded, seals as a viable replacement for glass-ceramic seals [4].

Compressive seals offer several benefits as compared to their glass-ceramic counterparts. First, the seals are designed to undergo interfacial slip, thereby accommodating differential lateral expansion of sealed components. As a result, the added constraint of minimizing the coefficient of thermal expansion

is eliminated. In addition, this sealing technology expands the choices for potential interconnect materials. Although research is in its developmental stages, researchers have been able to achieve promising results [7-19]. For example, Stevenson and Chou [16] have demonstrated a very low leakage rate of ~1.6 x 10-4 sccm/cm at 800 °C and a stress of 100 psi, which was ~4300 times lower than previously published studies by Simner and Stevenson for the same loading conditions [20].

1.3. Compressive Seal Leakage Modeling

Leakage experiments have been the primary means for the development and maturation of compressive seal technology in SOFCs. To date, there have been only a few published modeling studies as it pertains to SOFCs. Koeppel et. al. developed a viscoelastic damage model to predict the accumulated damage rigidly bonded glass ceramic seals experience after repeated thermal cycling [21, 22]. Wuillemin et. al [23] use modeling and experimentation to demonstrate the effect imperfect sealing has on SOFC stack open circuit voltage by altering the porosity of a medium, which served as the sealing material. Through their work, it was shown that an increase in porosity results in a reduction in the voltage output in an SOFC stack. Moreover, most of the modeling studies deal with stack level implications that occur with glass-ceramic seals and these studies have been somewhat limited in scope. Nevertheless, compressive seal leakage modeling could enhance the technology's development in several ways. First, modeling could reduce the time associated with evaluating various compressive seal alternatives. For example, in order to assess the mid-term stability (e.g., 3600

hours of continuous operation) of the compressive seals, leakage experiments require several thousands of hours to obtain data regarding the viability of a particular seal configuration or sealing component. If the aforementioned seal configuration were accurately captured via a leakage model, these models could then be used to eliminate unsatisfactory sealing alternatives without squandering time and resources on testing. Next, leakage modeling used in a complementary fashion with experiments can elucidate and confirm experimental trends in a more systematic fashion. Presently, trial-and-error has been employed to improve compressive seals. Not only can models can be used to extract trends, but they also could be used to demonstrate future proof-of-principle sealing designs for solid oxide fuel cells.

1.4. Research Objectives

The primary objective of this study was to develop a contact mechanics based computational leakage model, which would be validated through leakage experiments and material characterization studies that elucidates how several features (i.e., surface topography, mechanical deformation, and elastic material properties) affect the sealing characteristics and average surface separation in a compressive seal assembly. It was decided that two fundamental configurations should be analyzed: a single interface metal-metal compressive seal arrangement and a multiple interface mica-based compressive seal arrangement. The metal-metal configuration will be used primarily to demonstrate the effect of surface topography on leakage, but also to provide a framework for modeling leakage in multiple interfaces. In addition, the model development associated

with the metal-metal configuration allowed adequate proof-of-principle for later analyzing leakage rates in the more complicated mica compressive seal configuration. Allowing movement along basal planes and having voids throughout its cross section, mica's microstructure is very complicated as compared to stainless steel. Moreover, one of the consequences of applying the subsequently presented leakage computational model on a mica-based compressive seal assembly is that primary and secondary leakage paths can then be quantitatively identified directly.

The intent of the leakage studies presented in this document was not only to provide pertinent information regarding the salient features that must be present for adequate sealing to take place, but these results should also prove to be useful in assessing the operating condition that facilitates acceptable long-term performance of mica-based compressive seals for SOFC applications. Presently, there have been limited SOFC seal leakage studies that quantify the minimum acceptable leakage rate for satisfactory fuel cell performance [8], and there have been no models that characterize leakage rates in compressive SOFC seals. As a result, a secondary objective was to define and specify the physical features that are needed to achieve acceptable seal performance in a simulated SOFC environment. The following research questions have been investigated:

Compressive Seals in General:

- How does temperature, applied compressive load, and surface roughness impact leakage in a single interface compressive seal?

- Does the Jackson-Streator [24] micro-contact model adequately approximate the interfacial separation of a single interface compressive seal over a wide range of compressive loads and temperatures?
- What is the role of surface topography in regards to the efficacy of compressive seals? Is it reasonable to conclude, a particular surface topography can be maintained over the life of the compressive seal to ensure hermeticity is not compromised?

Mica-based Compressive Seals:

- With regard to conventional mica-based compressive seals, is it satisfactory to model a mica layer as a continuous sheet without any regard for its porous microstructure?
- Does the number of mica layers used in a conventional mica-based compressive seals have any impact on the overall leakage? If so, is it possible to mitigate such leakage?
- What are the implications for future compressive seal design that can be gleaned from the mica-based compressive seal study?

Answering the above questions should not only provide insight regarding the nature of leakage in current state-of-the-art compressive seals, but it should also provide guidance as it pertains to the relative effect operating conditions have on seal performance. In addition, SOFC developers could then use the current

modeling approach as a means of disqualifying various candidate compressive seal designs without excessive hours of experimental testing.

2. RESEARCH BACKGROUND

2.1. Compressive Seal Experimental Studies

In order to demonstrate the viability of mica-based compressive seals as a legitimate alternative to rigidly bonded seals, several researchers have conducted leakage experiments. Such experiments served not only to establish the efficacy and hasten the evolution of compressive seals in SOFC assemblies but also to simulate how well the aforementioned seals can withstand the simultaneous oxidizing and reducing environment over repeated thermal cycles. In early studies, Chou and Stevenson investigated the effect of load and mica layer thickness [11, 16]. Based on the aforementioned study, it was determined that leakage rates increased as mica layer thickness increased. In addition for the same loading conditions, the leakage rates exhibited in the plain mica seal assembly were considerably higher than the hybrid mica assembly, which includes a glass interlayer between the mica and its metal interlayer. These and other tests revealed that the primary leakage paths were between the mica layer and the adjacent metal interface instead of amongst the distinct mica layers.

Although adding glass interlayers resulted in a substantial reduction in short-term leakage rates, there was concern as to whether or not these glass interlayers could withstand repeated thermal cycling without introducing undesirable interfacial reactions in the hybrid compressive seal assembly. As a result, Chou and Stevenson investigated the mid-term stability of hybrid mica-

based compressive seals using three different interlayers [25]. Each set of interlayers exhibited very limited interfacial reactions after experiencing 350 to 700 hours of thermal cycling. However, after repeated cycling the glass interlayers were shown to break down. As a result, glass interlayers were then replaced with silver and gold interlayers. Although the silver based hybrid compressive seals were more stable and did not exhibit any interfacial reactions, the leakage rates were a bit higher than its glass interlayer counterparts [10, 26]. The latter studies reduced secondary leakage paths within the mica layers themselves by impregnating phlogopite mica layers with a metal-forming infiltrant. The leakage rates were one or two orders of magnitudes lower than as–received micas for the same loading conditions [9]. Subsequent studies by Stevenson and Chou using compressive seal studies have demonstrated the long-term effectiveness of “infiltrated” micas. The hybrid compressive seals were subjected to more than 1000 cycles in a reducing environment, and seal performance was deemed acceptable by way of constant open circuit voltage measurements throughout the duration of the study. Although the infiltrated hybrid mica seals demonstrated their feasibility in the above study, it should be noted that the infiltrant used is not stable in an actual SOFC environment [14]. As a result, an undesirable by-product of mica infiltration was that the infiltrants were responsible for interfacial reactions that resulted in premature seal degradation. Most recently, Stevenson and Chou have developed an alkaline earth glass interlayer whose CTE is designed to closely match adjacent anode-electrolyte components and is nonreactive with the previously mentioned

components [27]. By incorporating an alkaline earth glass interlayer into the hybrid compressive seal, the resulting compressive seal was able to demonstrate hermeticity at 1050 C after full reduction and 10 thermal cycles[28]. This mica compressive seal configuration seems the most viable for eventual implementation within SOFC stacks.

2.2. Relevant Seal Modeling Studies

A mixed lubrication model is needed to relate the pressurized gas flow to the mean interfacial spacing. Patir and Cheng [29] used numerical flow simulations to derive an average Reynolds equation for rough surfaces in terms of shear and pressure flow factors. Tripp [30] later extended the flow factor concept using a perturbation solution, and the work established an analytical basis for the average flow model. Although several researchers who have modeled leakage rates in static seals have employed Patir and Cheng's flow factor approach, there has been controversy regarding the appropriateness and effectiveness of the aforementioned pressure factors. Teale and Lebeck [31] along with Tonder [32] both conducted average flow model calculations under the flow conditions reported by Patir and Cheng, but derived flow factors that were quite different from those proposed by the latter. Yuanzhong and Lingqing [33] were able to resolve the aforementioned differences, and concluded that boundary conditions, grid systems, and surface statistics contributed to the discrepancies. In addition, they were able to show that for surface separations normalized with respect to the root-mean-square roughness greater than 2.5,

Patir and Cheng's pressure flow factors yield predictions within the uncertainty range of more recent perturbation-based models by Elrod [34] and Tripp [30] when the normalized surface separation exceeded 2. Most recently, Peeken et al. [35] employed more sophisticated procedures for surface generation and flow simulation, and in turn, were not only able to resolve the differences between the analytical solutions authored by Elrod [34] and Tripp [30], but they were also able to produce flow factor charts for two types of surfaces – a standard Gaussian and a sintered surface with high skewness.

Several seal leakage models have employed Patir and Cheng's flow factors to evaluate seal performance. When developing a model to evaluate the performance of end face seals, Etsion and Front [36] employed an elastic-plastic contact model and average flow model. Although thermal effects were not considered, they did indicate that at a certain loading threshold, surface roughness had diminishing effects on the leakage rates in end face seals. Afterwards, Polycarpou and Etsion [37] extended the above leakage model for static seals to include rarefaction effects. More recently, Ruan et al. [38] developed a model that incorporated the effects of various coupled physical mechanisms including surface roughness, elastic-plastic contact, face deformation, thermal deformation, and phase change. Surface deformation was approximated in mechanical face seals using mechanical and thermal influence coefficients, which yielded a greatly reduced computation time as compared to performing repeated finite element calculations for each updated configuration. Harp and Salant [39] incorporated the previously mentioned flow factors in the

rough surface induced asperity model that also included the effects of both inter-asperity and macroscopic cavitation. The model was later used to investigate how cavitation affects the sealing mechanism of two rotating shaft seals – lips and mechanical end seals [40].

The leakage studies discussed in the present study investigate the effect surface roughness, applied compressive load, and temperature has on leakage in a static compressive seal; more specifically, the implications of surface finished is examined in metal-metal compressive seal leakage studies, the applied compressive load is varied at average stress levels of 100 (0.689 MPa), 300 (2.068 MPa), and 500 psi (3.447 MPa), and temperature is varied at levels of 25, 250, and 500^{o}C, respectively. In addition to the temperature analysis, the macro portion of the leakage model accounts for mechanical deformations, while Patir and Cheng's isotropic roughness pressure flow factors are used to incorporate mixed lubrication effects on the Reynolds equation. Due to the fact that friction is neglected in the modeling approach, thermal deformation effects by way of lateral expansion and contraction are not captured in any of the subsequently leakage models. All the surfaces that are presented have normalized surface separation in excess of 2.0. According to the literature, at normalized surface separations greater than 2, Patir and Cheng's pressure flow factors are within the bounds of error as compared to flow factors determined using more sophisticated numerical techniques [35]. Thus, the isotropic flow factors developed by Patir and Cheng have been included in the current leakage model due to their accuracy and ease of calculation. The computational leakage

model employs an axisymmetric finite element approach to obtain the contact pressure distribution within the sealing interface. The operative contact model (e.g., GW model [41] or Jackson-Streator model [42]) is then applied on a nodal basis to ascertain the mean surface separation at each point along the discretized nominal contact domain. Such an approach contrasts the typical application of micro contact models throughout the literature, which often average the mean surface separation over the entire nominal contact region instead. The mixed lubrication model is then applied in a similar fashion as the seal model studies above.

3. LEAKAGE MODEL APPROACH AND REFINEMENTS

The computational leakage model presented throughout this document has been enhanced and refined through surface roughness characterization studies as well as experimental leakage tests. Although the modeling effort has evolved to include effects such as elastic-plastic deformation and three-dimensional surface roughness, conceptually, the functions of its three submodels have been unaltered. The macro contact model is finite element-based and it is used to determine the pressure distribution in the annular contact zone. Next, a micro contact model is employed to approximate the mean interfacial separation at each of the discretized nodes within the annular contact zone, which is then fed into a mixed lubrication based average Reynolds equation. Using the mixed lubrication corrected Reynolds equation, it is then possible to determine the volumetric leakage rate for a compressive seal configuration under the specified operating conditions.

While the modeling effort is the central focus of this dissertation, the aforementioned leakage experiments and surface roughness characterization studies were critical for its evolution. The aging of stainless steel substrates has been documented through each forthcoming leakage study as a means of determining the limitations of the leakage computational model as it relates to surface roughness. In addition, leakage results and surface roughness scans provided the context and often the justification for implementing various modifications in the previously mentioned submodels. These experiments have

been used to isolate the effects of physical parameters such as applied compressive load, temperature, and surface finish. It is of great importance to note, that the stainless steel substrates used in the metal-metal compressive seal studies were machined to a particular finish prior to the onset of all leakage studies, and neither of the two substrates were ever reprocessed at any instance during the leakage study. As a result, surface roughness scans have also been used to literally document the changes each substrate experiences as a result of repeated loading and exposure to heat; that is, scans and material characterization tests have been performed throughout the computational model's evolution to document the degree of plasticity present at asperity peaks. In the case of the mica-based compressive seal studies, which will be discussed in greater deal subsequently, surface roughness scans were performed prior to each leakage test. When the number of mica layers used or the temperature was changed, new phlogopite substrates were inserted into the compressive assembly to replace the "used" mica substrates. Thus, scans were used in mica-based and metal-metal compressive seals to assess surface characteristics a priori. The leakage computational model is then employed to predict the leakage based on the loading and surface conditions. The three chapters immediately following the current chapter elucidate critical aspects of the modeling and experimental approach, respectively.

4. LEAKAGE MODELING – ELASTIC ONLY

4.1. Leakage Model Overview

In this chapter the elastic computational leakage model is introduced. The leakage modeling approach is modular consisting of three interacting submodels, although the Jackson-Streator [24] micro contact model is applied exclusively throughout this document to predict the average surface separation due to the fact that it provides a single unambiguous solution as compared to its statistically based counterpart. A single interface metal-metal compressive seal assembly is used to demonstrate how leakage is approximated in the current elastic only computational model. Once this model is introduced, a more sophisticated computational leakage model extends the current formulation to assess elastic-plastic deformation in Chapter 5.

Reiterating the modeling objectives, the chief aim of the leakage studies is to investigate how the applied compressive load, temperature, and interfacial surface roughness affect the volumetric leakage rates that occur within a metal-metal compressive seal assembly. In addition to facilitating greater insight as to how these parameters affect leakage, the leakage results from the study will also be used as a basis for evaluating the validity and effectiveness of a new micro contact model over a wide range of loads and temperatures, which, presently, is the most critical and uncertain component for predicting leakage. In contrast to the conventional mica-based compressive seals (that will be modeled and

discussed in subsequent chapters), which have several different interfaces through which leakage can occur, the metal-metal seal depicted in Figure 3 and discussed throughout this chapter consists of a single interface across which a sealed gas can flow. A compressive load, P, is applied so that the annulus contacts the stainless steel substrate with a prespecified average compressive stress. The gas encased by the annulus is pressurized above atmospheric pressure, which causes the gas to seep out the annulus-substrate interface. Furthermore, the leakage model results discussed throughout this document are assumed to occur in an isothermal, steady flow environment. Temperatures are investigated at 25, 250 and 500 °C, while pressures no more than 3.5 kPa above atmospheric pressure are considered. The loading and flow conditions considered in each parametric study mirror those conditions used in the metal-metal compressive leakage experiments presented subsequently for comparative purposes. Leakage results were obtained using the Fast Fourier Transform (FFT) based Jackson-Streator model[24]. In comparison to a previous leakage computational model presented by Green et al.[43], the present computational leakage model has several improvements. First, the working fluid is treated as a compressible fluid. Next, the macro contact model uses a flexible-flexible modeling approach in lieu of the rigid–flexible arrangement in the previous study to more accurately capture the interfacial pressures and deformation in the seal interface. Moreover, the flexible-flexible approach incorporates the Inconel annulus's elastic properties into the finite element model, while the rigid-flexible

arrangement assumes that the Inconel's modulus in infinite, and in turn, does not allow any deflection.

Suppose an Inconel annulus deforms a SS 316 substrate. The procedure used to quantify leakage is detailed as follows:

- Prescribe the magnitude of the average compressive stress and the ambient temperature within the annular contact region of the SS 316 substrate.
- Compute the contact pressure distribution along the surface of the SS 316 substrate from the macro-contact model.
- Compute the average interfacial separation at each node using the Jackson-Streator JS model.
- Use the contact pressure, flow factor, and surface separation values to integrate the average Reynolds Equation and quantify the volumetric leakage rate.

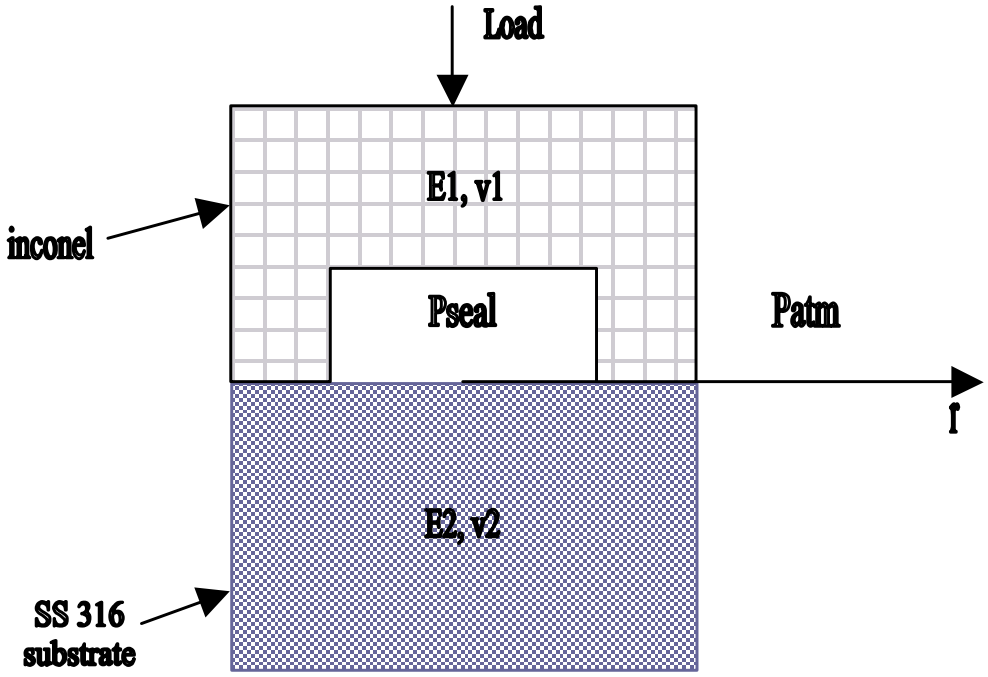

Figure 3: Depiction of metal-metal seal used throughout the current leakage model demonstration.

4.2. Macro-Contact Model

The macro-contact model is used to determine the pressure distribution within the annular contact zone. Thermal and mechanical deformations are considered in this model. However, surface roughness effects are neglected; thus, the annulus-substrate interface is considered to be nominally smooth. The "macro-contact model" represents the gross dimensions of the annulus-substrate interface exclusively. Thus, surface roughness effects are in fact removed from the overall seal geometry, and are subsequently evaluated in the micro-contact model. Due to the inherent symmetry of the annulus on flat configuration, an

axisymmetric ½ finite element model is used to determine the pressure distribution along the surface of the stainless steel substrate.

A global-local approach has been employed for mesh refinement. As depicted in Figure 4, in the contact zone along the surface of the steel substrate, there are 101 nodes. The ANSYS finite element package is used to determine macroscopic results. A linear element with axisymmetric key options (e.g. Plane 42) is then used to mesh both the SS substrate and Inconel. The mesh is refined so that it becomes coarser further away from the contact zone. Symmetric boundary conditions are employed along the axial direction of the steel substrate and annulus. In the radial direction along the bottom of the steel, the nodes are constrained so that no axial displacement is allowed. A uniform temperature equal to the furnace temperature is applied to all nodes in the contact model. Care was taken to apply the coefficient of thermal expansion correctly based on CTE values found in material handbooks [44]. The pressure distribution in the contact zone is determined in the macro model and is subsequently used in the micro contact model.

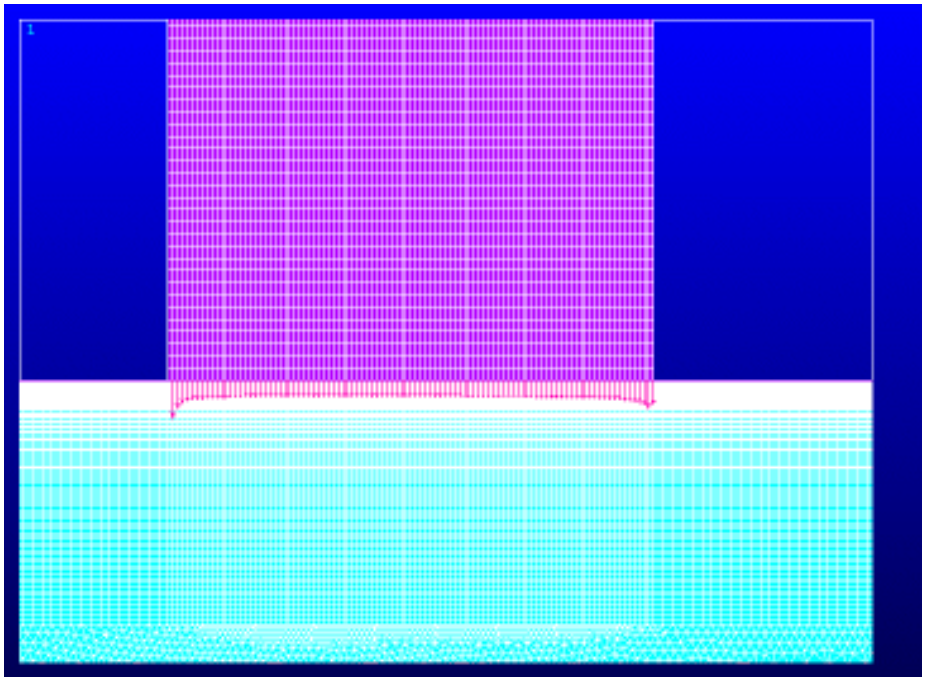

Figure 4: Depiction of global-local mesh used in macro contact model involving a single interface.

4.3. Micro-Contact Model

On a micro level, all surfaces have some degree of waviness or roughness. In the current model, the effect of the previously neglected surface imperfections is now assessed. The parameter of interest that needs to be determined is the average surface separation at each of the discretized nodes in the contact zone. There have been several approaches to approximating the aforementioned gap including statistically-based [45, 46] and fractal [47, 48] models, which have evolved to account for various effects including adhesion [49] and plasticity [50]. Due to the fact that the compressive loads discussed in this study are significantly lower than those required to produce bulk plastic deformation, it is assumed that the asperity contact is elastic. Thus, an elastic

contact approach is employed in the micro-contact model. Nevertheless, the validity of the previous assumption will be evaluated in the comparison with experimental leakage results. In an effort to address the well-documented ambiguity of scale associated with statistically based models like the well-known Greenwood-Williamson model [41], an FFT-based model, namely the Jackson-Streator model, is used as the micro-contact model in hopes of more accurately capturing the multi-scale nature of contact. This model was chosen over statistically–based models in general, because it provides a single unambiguous solution as opposed to a family of solutions. In general, additional specifications are needed (e.g., an arbitrary autocorrelation length, corresponding radius of curvature, and amplitude) to specify a particular solution using the previously mentioned statistically based models. As a result, a given pressure distribution will have multiple solutions for the average surface separation unless an arbitrary set of metrics are introduced to further specify the solution. For example, metrics like an autocorrelation length of 0.1 have been used as means of adding specificity to the predicted results as the modeling problem dictates as long as the predictions compared favorably. Rather than institute an ad hoc approach to specifying the scale of observation, the JS model is used to provide a systematic, single solution for a set of loading conditions. Later, the validity of the elastic contact assumption is assessed by comparing the contact pressure at a given frequency level k to that of the critical pressure required to initiate plasticity.

In order to implement the JS model, a 3D surface roughness scan was conducted. The axisymmetry of the metal-metal configuration along with the

assumption that the elastic material properties and surface roughness are isotropic allows for a subset of the Inconel-Stainless Steel topography to be analyzed as an adequate representation of the entire stainless steel surface. A ¼ surface scan is used throughout this study, primarily, because this area is large enough to capture the dominant longer wavelengths associated with the aforementioned stainless steel substrates, while also allowing a manageable sample set with an acceptable spatial resolution. The metal-metal configuration depicted in Figure 3 is modeled as an annular flat loading a rough isotropic surface. The Inconel annulus is modeled as a perfectly smooth flat for two reasons. First, the said annulus's surface finish is considerably smoother than either of the substrates, which was determined after viewing each of the two surfaces under a microscope. Next, performing surface roughness scans on the nominal annular contact zone was impractical with the Rodenstock laser spectrometer, because surface scans would be confined to a short scan length (e.g. the annular radial distance is 0.125" or 3.175 mm) since circumferential scans are not possible with this particular profilometer. Such scans are critical due to the fact that the longer range wavelengths ultimately dominate the leakage at the annular interface. As a result, it would be impractical to obtain an accurate representation of the annular region with a series of radial scans using the Rodenstock spectrometer. Future studies should employ a microscope-based laser profilometer so that the Inconel's roughness may be adequately captured. Nevertheless, the Rodenstock laser profilometer was used to assess the roughness of the stainless steel substrate since it is modeled as the rough

surface in the current model. Once the raw surface roughness data, $z(x,y)$, is determined, the discretized residual surface, $\zeta(x,y)$, is then calculated by subtracting the least squares mean plane, $f(x,y,)$ from $z(x,y)$ in the same fashion as Dong et al. [51]. Since the stainless steel substrate is nominally planar, the least squares adjustment provides an appropriate means of transforming the raw data. In addition, the residual surface is convenient, because it establishes a zero reference plane that coincides with the least squares plane. Another consequence of the aforementioned selection is that the mean of our residual surface is zero. All subsequent surface profile parameters and FFT calculations are determined using the residual surface. The digitized surface used throughout this study is a 256 by 256- point discretized representation of a 16 mm by 16 mm SS316 surface scan, which in effect, corresponds to a scanned point every 62.5 microns. Prior to settling on the number of points per scan length, a preliminary study was conducted to ascertain how key surface parameters were affected by the resolution. After observing the resulting FFT spectrum along with the root-mean-square roughness, it was determined that a scanned point every 62.5 microns was suffice for modeling purposes. A representative depiction of the said surface is included as Figure 5. Although the previously mentioned residual surface scan is used for all calculations, it should be noted that no additional adjustments are performed on the raw surface scan data, which indicates if a surface defect is in fact present, its influence will also be included in the subsequently determined frequency spectrum.

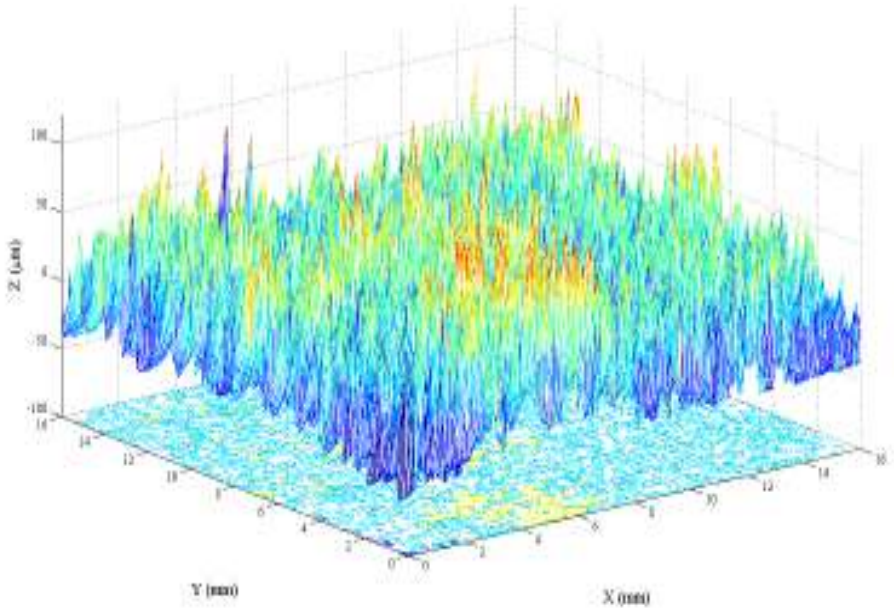

Figure 5: Residual surface of a lapped 100 grit SS 316 substrate is depicted.

A two dimensional FFT is then performed on the residual surface, using the following equation:

$$F(k_x,k_y)=\frac{1}{N_xN_y}\sum_{N_x=0}^{N_x-1}\sum_{N_y=0}^{N_y-1}\zeta(n_x,n_y)e^{-i2\pi(\frac{k_xn_x}{N_x}+\frac{k_yn_y}{N_y})} \quad (1)$$

where: k_x and k_y are the indices corresponding to spatial frequencies in *x* and *y*, while n_x and n_y are indices corresponding to the spatial coordinates in *x* and *y*. The result is a 256 by 256 matrix, *F*, whose entries are complex numbers. To eliminate any ambiguity regarding the interpretation of spatial frequencies and their corresponding amplitudes, the diagonal of FFT, F_{ii}, are used in the Jackson-Streator Model in lieu of the entire matrix. The implication of this selection is that the scanned surface's frequency spectrum will be reduced from 65536 elements

to 128 elements. Specifically, the amplitude Δ_k at frequency number $k_x = k_y = k$ is set equal to 4 times the magnitude of the complex coefficient F(k,k). The reason for the factor of 4 comes from noting that a signal of the form $A\cos(2\pi k n_x/N_x)\cos(2\pi k n_y/N_y)$ will have a corresponding coefficient *F(k,k)* equal to *A*/4. The amplitudes so determined, are later used to determine the average surface separation at each of the 101 nodes along the surface of the Inconel–substrate interface. Although F is indeed an N by N matrix, one consequence of defining Δ_k as indicated above is that we are now no longer able to map a given amplitude to its corresponding spatial frequency in x and y. Thus, even though the frequency spectrum content by it very definition is obtained in a deterministic fashion, the extracted spectrum content is then applied as a measure of the overall surface characteristics rather than a particular areal domain on the surface. Moreover, it is argued that these diagonal amplitudes are sufficient to characterize the gap. Thus, the entries are used to assign a single amplitude to a given frequency and are employed to determine the average surface separation at each of the nodes along the surface of the Inconel–substrate interface. The JS model employs a trapped volume approach to obtain the average surface separation at a given nodal location, Which is an extension of a 1D rough contact solved by Westergaard [52]. Later, Johnson et al. [53] employed Kalker's method to determine a numerical solution for elastic contact between a 2D sinusoidal surface with a flat. Johnson's numerical results for approximating the real area of contact and mean surface separation are used extensively with the application of the JS model.

The JS Model in the present study has been applied in a recursive fashion to determine the average gap along circumferential bands of thickness Δr at each nodal location in the annular contact zone. The steps in the calculation are indicated by the flow chart in Figure 6. First, the scan length, L, of the roughness measurements is specified. Then, a 2D FFT is performed using Equation (1), which yields β_k, the FFT amplitude at a given frequency level k. Over the annular contact zone, the asperity density at each frequency level k is equal to twice the square of the spatial frequency; that is, $\eta_k = 2f_k^2$ where f_k denotes the reciprocal of the wavelength associated with frequency level k.

The iteration begins at the inner radius and steps through each of the nodal radii, r_j. The iteration on the radius serves as the outer loop. For a given radial location, the base level nominal contact area A_0 is set to the area of the nodal annulus, namely $(2\pi r_j)\Delta r$. The base level mean pressure p_0 is set to the nodal pressure from the macroscopic model. Next, k is set to 1 and the inner loop of the iteration begins.

Within this inner loop, for a given frequency level, the number of asperities in contact N_k is calculated from the asperity density and the nominal contact area associated with the frequency level, namely A_{k-1}. For k = 1, the nominal contact area is just the base level A_0. Next, the contact area $\bar{A}_k$ of a single k-level asperity is computed using the following the approach of JS model, which is detailed below. Next the (real) contact area (A_k) for the frequency level k is set equal the number of k-level contacting asperities (N_k) times the contact area per

k-level asperity $\bar{A}_k$. When this value exceeds the nominal contact area ($A_{k\text{-}1}$) associated with frequency level *k*, the A_k is re-set to equal $A_{k\text{-}1}$. (This latter condition is done to enforce one of the assumptions of the JS model: namely, that a given frequency level cannot experience a contact area greater than the frequency level below it since the lower frequency level provides the nominal contact area for the given frequency level.)

Next the static load balance is applied to obtain the mean contact pressure ($\bar{p}_k$) at frequency level *k*. This mean pressure is defined to be the total load on the nodal annulus divided by the nominal contact area ($A_{k\text{-}1}$) associated with frequency level *k.* From the load balance, the mean pressure at frequency level *k* satisfies the condition

$$\bar{p}_k A_{k-1} = p_0(r_j) A_o(r_j) = p_{\text{mm}}(r_j)\left(2\pi r_j \Delta r\right) \tag{2}$$

Thus,

$$\bar{p}_k = \frac{p_{\text{mm}}(r_j) 2\pi r_j \Delta r}{A_{k-1}}. \tag{3}$$

Next, the volume loss, $(V_{loss})_k$, associated with frequency level *k* is computed from the mean pressure using a procedure that is detailed below. Once this *k*-level volume loss is computed, the frequency level is incremented. The inner loop continues until all frequencies levels are considered. Then, the overall loss in mean spacing for the given nodal annulus is computed according to

$$h_{loss}(r_j) = \frac{1}{2\pi r_j \Delta r} \sum_{k=1}^{N} \left(V_{loss}\right)_k \tag{4}$$

From this the mean spacing for the nodal annulus is determined from

$$h(r_j) = c_{\max} - h_{loss}(r_j) \tag{5}$$

where c_{max} represents the gap at the initial, no-load, contact between the steel substrate and the Inconel annulus. The aforementioned height, c_{max}, was approximated by taking the ten-point average of the magnitudes of the five highest peaks and five lowest valleys within the nominal annular contact zone. This method is used for approximating the undeformed gap in lieu of the absolute maximum peak in the contact zone, because the former is statistically less susceptible to measurement-related variability.

Once the mean gap has been computed for the nodal annulus at the given radial location, the iteration proceeds to the outer loop (Figure 6) whereby the radial position is incremented. The iteration finishes when the entire contact region has been covered.

We now provide details on the determination of the single k-level asperity contact area ($\bar{A}_k$) as well as on the determination of the k-level volume loss, $(V_{loss})_k$ which are needed in the iterations described above.

Although there is no general analytical expression for incomplete contact, Johnson, Greenwood and Higginson ("JGH" hereon) [53] provided two asymptotic solutions. Following their approach, a reference pressure is defined according to

$$p_k^* = \pi\sqrt{2}E^*\Delta_k f_k \tag{6}$$

where Δ_k is the amplitude of the sinusoidal profile at the current frequency level *k*. It is readily shown that Δ_k is related to the FFT amplitude coefficient β_k via the simple relation, $\Delta_k = 4\beta_k$. For a lightly loaded contact, a Hertzian approach is applicable, while an alternate expression is applicable for heavily loaded (or nearly complete) contact. When $\bar{p}_k(r) << \bar{p}_k^*(r)$, the following expression applies:

$$(\overline{A}_{JGH})_1 = \frac{\pi}{f_k^2}\left[\frac{3}{8\pi}\frac{\bar{p}_k}{p_k^*}\right] \tag{7}$$

and in the nearly complete contact case, the following expression is used:

$$\left(\overline{A}_{JGH}\right)_2 = \frac{1}{2f_k^2}\left(1-\frac{3}{2\pi}\left[1-\frac{\bar{p}_k}{p_k^*}\right]\right) \tag{8}$$

Jackson and Streator [24] later performed a polynomial curve fit on the Johnson et al. [53] experimental data in conjunction with the above pair of equations, giving:

$$\bar{A}_k = \left(\bar{A}_{JGH}\right)_1 \left(1 - \left[\frac{\bar{p}_k}{p_k^*}\right]^{1.51}\right) + \left(\bar{A}_{JGH}\right)_2 \left(\frac{\bar{p}_k}{p_k^*}\right)^{1.04} \quad \text{for } \frac{\bar{p}_k}{p_k^*} < 0.8$$

$$\bar{A}_k = \left(\bar{A}_{JGH}\right)_2 \quad \text{for } 0.8 < \frac{\bar{p}_k}{p_k^*} \le 1.0 \tag{9}$$

Now in order to compute *k*-level volume loss, $(V_{loss})_k$, a third order piece-wise curve fit was performed on data of Johnson et al. [53] who presented numerical solutions relating the normalized surface separation and normalized contact pressure: The third-order piecewise curve-fit is included as Equation (10):

$$\left(\frac{h_k}{\Delta_k}\right)^{\frac{2}{5}} = -19.565\left(\frac{\bar{p}_k}{p_k^*}\right)^3 + 14.97\left(\frac{\bar{p}_k}{p_k^*}\right)^2 - 4.6175\left(\frac{\bar{p}_k}{p_k^*}\right) + 1.0052$$

$$\text{for } \left(\frac{\bar{p}_k}{p_k^*}\right) \le 0.32$$

$$\left(\frac{h_k}{\Delta_k}\right)^{\frac{2}{5}} = -.9269\left(\frac{\bar{p}_k}{p_k^*}\right)^3 + 2.1761\left(\frac{\bar{p}_k}{p_k^*}\right)^2 - 2.1787\left(\frac{\bar{p}_k}{p_k^*}\right) + 0.932 \tag{10}$$

$$\text{for } 0.32 < \left(\frac{\bar{p}_k}{p_k^*}\right) \le 1.00$$

The volume loss for frequency level *k* is then found using the following:

$$(V_{loss})_k = A_{k-1}\left(\Delta_k - h_k\right) \tag{11}$$

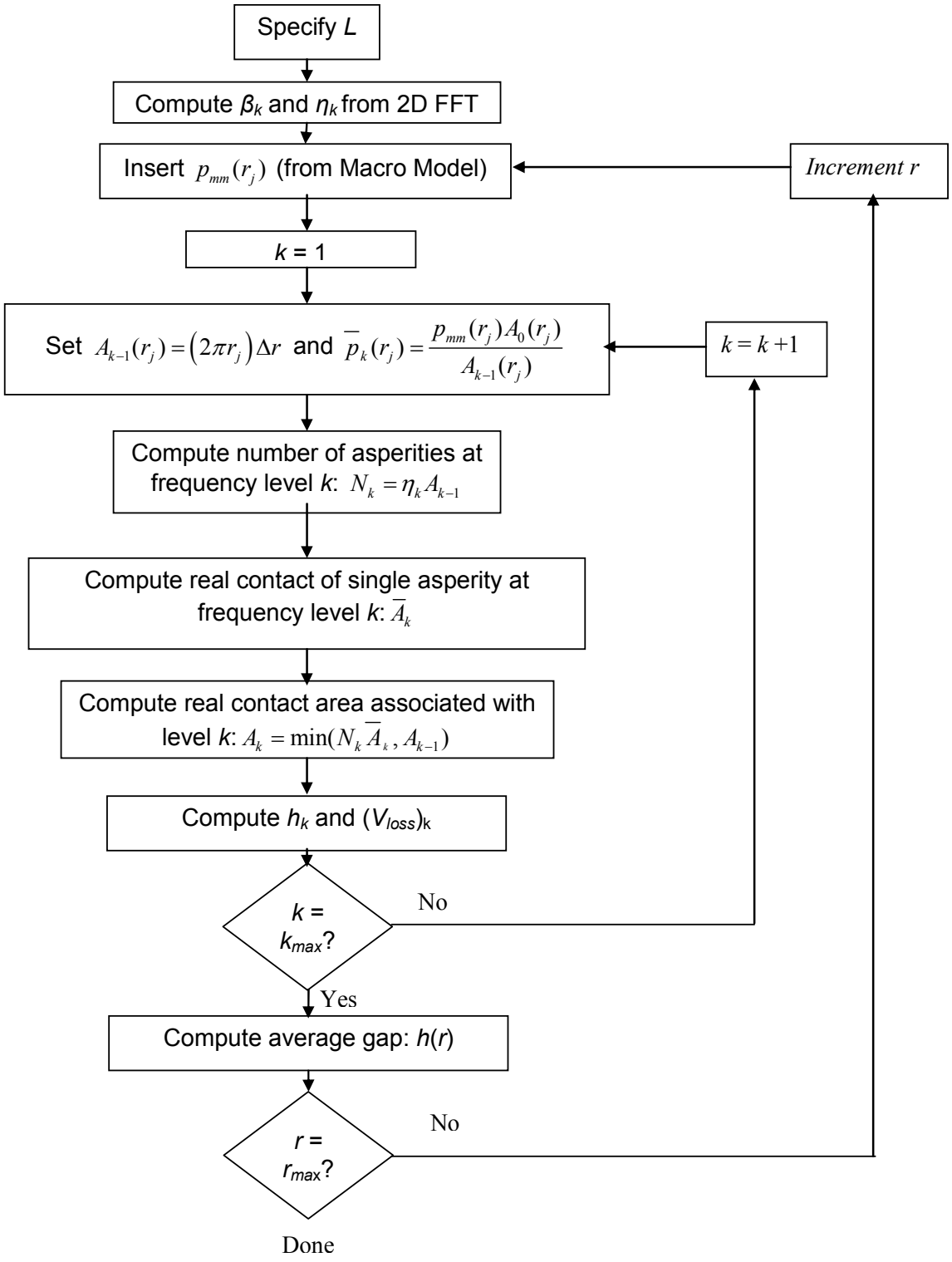

Figure 6: Flow chart of steps involved to approximate average gap using the Jackson-Streator model (Elastic deformation).

The loss in surface separation at the current radial distance *r* can then be determined as described earlier using Equation (4), and then the corresponding average surface separation is found using Equation (5).

This process is continued for all radial locations in the contact zone. The normalized surface separation, which is needed for the mixed-lubrication model, is then determined by dividing *h*(*r*) by the standard deviation of the residual surface heights [51], which for a discrete surface is expressed by the following:

$$S_q = \sqrt{\frac{1}{N_x N_y} \sum_{n_x=1}^{N_x} \sum_{n_y=1}^{N_y} \zeta^2 \left(n_x, n_y \right)} \tag{12}$$

4.4. Mixed Lubrication Model

Once the local normalized spacing is determined, a mixed lubrication flow model is then used to determine the volumetric leakage rate. The working fluid's gas constant is specified, and the fluid is treated as a compressible fluid with flow allowed in the radial direction exclusively. In addition, the surface roughness profile of the stainless steel substrate is considered to be isotropic. Thus, the average Reynolds Equation [54] for a compressible fluid in polar coordinates with no surface motion is given by

$$\frac{\partial}{\partial r}\left(\frac{\phi r \rho h^3(r)}{\mu}\frac{\partial p}{\partial r}\right)+\frac{1}{r}\frac{\partial}{\partial \theta}\left(\frac{\phi \rho h^3(r)}{\mu}\frac{\partial p}{\partial \theta}\right)=0 \tag{13}$$

Due to the axisymmetric flow conditions, the second term in Equation (13) disappears. Integrating the remaining term with respect to *r*, it follows that

$$\frac{\phi r \rho h^3(r)}{\mu}\frac{\partial p}{\partial r}=C \tag{14}$$

Where *C* is an integration constant. Patir and Cheng developed a model for pressure-induced flow between nominally smooth surfaces [29]. The parameter φ is the pressure flow factor, which for isotropic surfaces is defined by

$$\phi=1-0.9e^{-0.56\frac{h(r)}{S_q}} \tag{15}$$

Now for radial only flow, the mass leakage rate per circumferential seal length is given by

$$\frac{\dot{m}}{2\pi r}=-\frac{\phi \rho h^3(r)}{12\mu}\frac{dp}{dr} \tag{16}$$

where the local surface separation, *h*, varies as a function of *r*. After algebraic manipulation, Equation (16) may be written as

$$\frac{\phi r \rho h^3(r)}{\mu}\frac{dp}{dr} = -\frac{6}{\pi}\dot{m} \tag{17}$$

.

Comparing Equation (17) to Equation (14), we see that

$$C = -\frac{6}{\pi}\dot{m} \tag{18}$$

Since the working fluid is treated as an ideal gas, ρ = p/(RT). Thus, using the previous relationship Equation (17) can be rewritten as follows:

$$\frac{\phi r p h^3(r)}{\mu RT}\frac{dp}{dr} = -\frac{6}{\pi}\dot{m} \tag{19}$$

Isolating p and integrating both sides, the previous equation becomes

$$\frac{1}{RT}\left(\frac{p_o{}^2 - p_i{}^2}{2}\right) = -\frac{6\mu}{\pi}\dot{m}\int_{r_i}^{r}\frac{dr'}{\phi r' h^3(r')} \tag{20}$$

Where r' is a dummy integration variable. Setting $r = r_o$, the mass flow rate is given by

$$\dot{m} = \frac{-\pi p_o{}^2\left(1-\left(\frac{p_i}{p_o}\right)^2\right)}{12\mu RT\int_{r_i}^{r_o}\frac{dr'}{\phi(r')r'h^3(r')}} \tag{21}$$

In order to determine the volumetric flow rate at the outer radius per unit seal length, Equation (21) is then divided by of the fluid density along with the outer radius circumferential length, which leads to

$$Q = \frac{-p_o\left(1-\left(\frac{p_i}{p_o}\right)^2\right)}{24\mu r_o \int_{r_i}^{r_o} \frac{dr'}{\phi(r')r'h^3(r')}}. \tag{22}$$

It is convenient to specify leakage rates on a per unit length basis so the efficacy of different size seals can be compared readily for the same operating conditions. The circumferential length corresponding to the outer seal radius was chosen, because it corresponds to the maximum annular band after traversing across the entire sealing zone.

5. LEAKAGE MODELING – ELASTIC PLASTIC CONTACT

5.1. Overview

In the preceding chapter, an elastic only leakage computational model was presented. The current chapter seeks to extend the elastic only formulation into the elastic-plastic regime. Based on the compressive loads that were applied in the leakage studies, it is assumed that no bulk plastic deformation occurs in the annular contact zone. As a result, the finite element macro contact model used to determine the contact pressure distribution in the elastic only case is suffice for the elastic-plastic deformation model in the current case.

Although there is no bulk plastic deformation present in the compressed substrate, which provides adequate justification for neglecting plasticity in the current macro contact model, asperity peaks, particularly the taller asperity peaks, undergo significant plastic deformation. In the current formulation, the Jackson-Streator model is used to assess how each frequency level is impacted by plastic deformation. Moreover, the contact pressure at a given frequency level is compared to the critical pressure required to initiate plasticity. In the absence of a more convenient method for approximating the elastic-plastic nodal surface separation in the annular contact zone, the elastic-plastic real area of contact is used to approximate the said separation using JGH's [53] formulation presented previously. The assumption employed here is that degree of plastic deformation that occurs in the contact zone is not so severe that the asperities reach the fully plastic deformation regime. Thus, the elastic solution should provide a reasonable estimate for the elastic-plastic deformation being modeled.

Once the elastic-plastic area is determined, the gap is approximated by using a curve fit on the elastic solution results for three dimensional contact published by Johnson, Greenwood, and Higginson [53]. That is, the contact area is computed from an elastic-plastic analysis, but the gap is calculated from an elastic solution that relates gap to area. This approximation is implemented for simplicity, in the absence of a comparable elastic-plastic model relating contact area to gap.

Although we anticipate a larger decrease in surface separation when considering elastic-plastic deformation as compared to its elastic-plastic counterpart, the reduction in the average gap at each nodal location is not so significant that the gap to root mean square surface height is no longer adequately characterized by the mixed lubrication. As a result, similar to the macro contact model discussion above, the previously mentioned mixed lubrication formulation is also satisfactory for the present case.

5.2. Micro Contact Model – Elastic-Plastic

Recently, Krithivasan and Jackson [55] employed the finite element method to extend the elastic rough surface model to address three-dimensional elastic-plastic sinusoidal contact. The updated version of the JGH model accounts for elastic-plastic deformation by modifying several of the previously defined parameters. Using their approach, the elastic plastic pressure amplitude, $p^*_{ep}(r)$, is now given by the following relation:

$$p_{ep}^{*}(r) = p^{*}(r)\left(4.172\frac{S_y}{E^{*}} + 0.0173\right)\sqrt{\frac{\lambda_k}{\Delta_k}} \tag{23}$$

.

The updated expression for the area occupied by a single asperity, $\overline{A_k}$, is defined as

$$\overline{A}_k = \left(\overline{A}_{ep}\right)_k \left(1 - \left[\frac{\overline{p}(r)}{\left(p_{ep}^{*}(r)\right)_k}\right]^{1.51}\right) + \left(\overline{A}_{JGH}\right)_2 \left(\frac{\overline{p}}{\left(p_{ep}^{*}(r)\right)_k}\right)^{1.04}$$

$$\text{for } \frac{\overline{p}}{p_{ep}^{*}} \le 1 \tag{24}$$

$$\overline{A}_k = \left(\frac{1}{\lambda_k^2}\right) \quad \text{for } \frac{\overline{p}}{p_{ep}^{*}} > 1$$

where $\left(\overline{A}_{ep}\right)_k$ is the spherical elastic-plastic area contact area for a single asperity at the current frequency level *k*. The equation for $\left(\overline{A}_{ep}\right)_k$ was derived from the elastic–plastic model by Kogut and Etsion[56], and is given by

$$\left(\overline{A}_{ep}\right)_k = 2\left(\left(A_c\right)_k\right)^{\frac{1}{1+d}} \left(\frac{3\overline{p}(r)}{4CS_y}\lambda_k{}^2\right) \tag{25}$$

where *C* is a material constant defined by

$$C = 1.295e^{0.736\nu} \tag{26}$$

and v is the Poisson ratio for the softer of the two metals in the compressive seal interface. The parameter *d*, as shown in Equation (27), was determined by performing a curve fit on FEM results, and may be determined using the relation:

$$d = C_1\left(\frac{E^*\Delta_k}{S_y\lambda_k}\right)^{C_2} \tag{27}$$

where C_1= 3.8 and C_2= 0.11 are constants obtained empirically. Similarly, the critical contact area for the softer material on a frequency basis, $\left(A_c\right)_k$, is given by

$$\left(A_c\right)_k = \pi^3\left(\frac{CS_yR_k}{2E^*}\right) \tag{28}$$

with the radius of curvature at frequency level k, R_k , determined as follows:

$$R_k = \frac{1}{4\pi^2\Delta_k f_k^2}\,. \tag{29}$$

The area of contact for a frequency level *k,* $A_{k,}$ can then be determined as follows: $A_k = \min(N_k\overline{A}_k, (A_r)_{k-1})$. The min function prevents a higher frequency level from having a larger area of contact than any of the frequency levels preceding it. Once the real area of contact is calculated for all frequencies levels *k*, the calculations for approximating the loss in trapped volume and the local gap for a given frequency can then be performed.

In order to approximate the gap in the present case, a piece-wise third order polynomial curve fit was performed on Johnson et al [53] numerical results

to establish the relationship between the normalized surface separation and normalized contact pressure. The curve-fit is included as Equation (30):

$$
\begin{aligned}
&G^{\frac{2}{5}} = -19.565\left(\frac{\overline{p}}{p^{*}_{ep}}\right)^{3} + 14.97\left(\frac{\overline{p}}{p^{*}_{ep}}\right)^{2} - 4.6175\left(\frac{\overline{p}}{p^{*}_{ep}}\right) + 1.0052 \\
&\text{for } \left(\frac{\overline{p}}{p^{*}_{ep}}\right) \le 0.32 \\
&G^{\frac{2}{5}} = -.9269\left(\frac{\overline{p}}{p^{*}_{ep}}\right)^{3} + 2.1761\left(\frac{\overline{p}}{p^{*}_{ep}}\right)^{2} - 2.1787\left(\frac{\overline{p}}{p^{*}_{ep}}\right) + 0.932 \\
&\text{for } 0.32 < \left(\frac{\overline{p}}{p^{*}_{ep}}\right) \le 1.00
\end{aligned}
\tag{30}
$$

where $G \equiv \frac{h_k}{\Delta_k}$ is the fractional surface separation, h_k is the surface separation at frequency level *k* and Δ_k is amplitude at frequency level *k*. The volume loss for frequency level *k*, the loss in surface separation at radius *r*, and the corresponding average surface separation can then be determined as described in the Elastic only analysis via Equation (11) , Equation (4) and Equation (5), respectively.

An updated version of the flow chart used to describe the process for determining the average gap at a particular radial location is included as Figure 7. In addition to the modifications mentioned above, a critical addition is the box used to determine the contact pressure at a given frequency level. Using the assumption that the compressive load at a given radial location is the same at each frequency level, the contact pressure can be determined at each frequency level. Once the contact pressure at the current level is determined as shown in

Figure 7, it can then be compared to corresponding critical pressure for the given frequency level to determine the degree of elastic-plastic deformation, which is ultimately used to approximate the average gap.

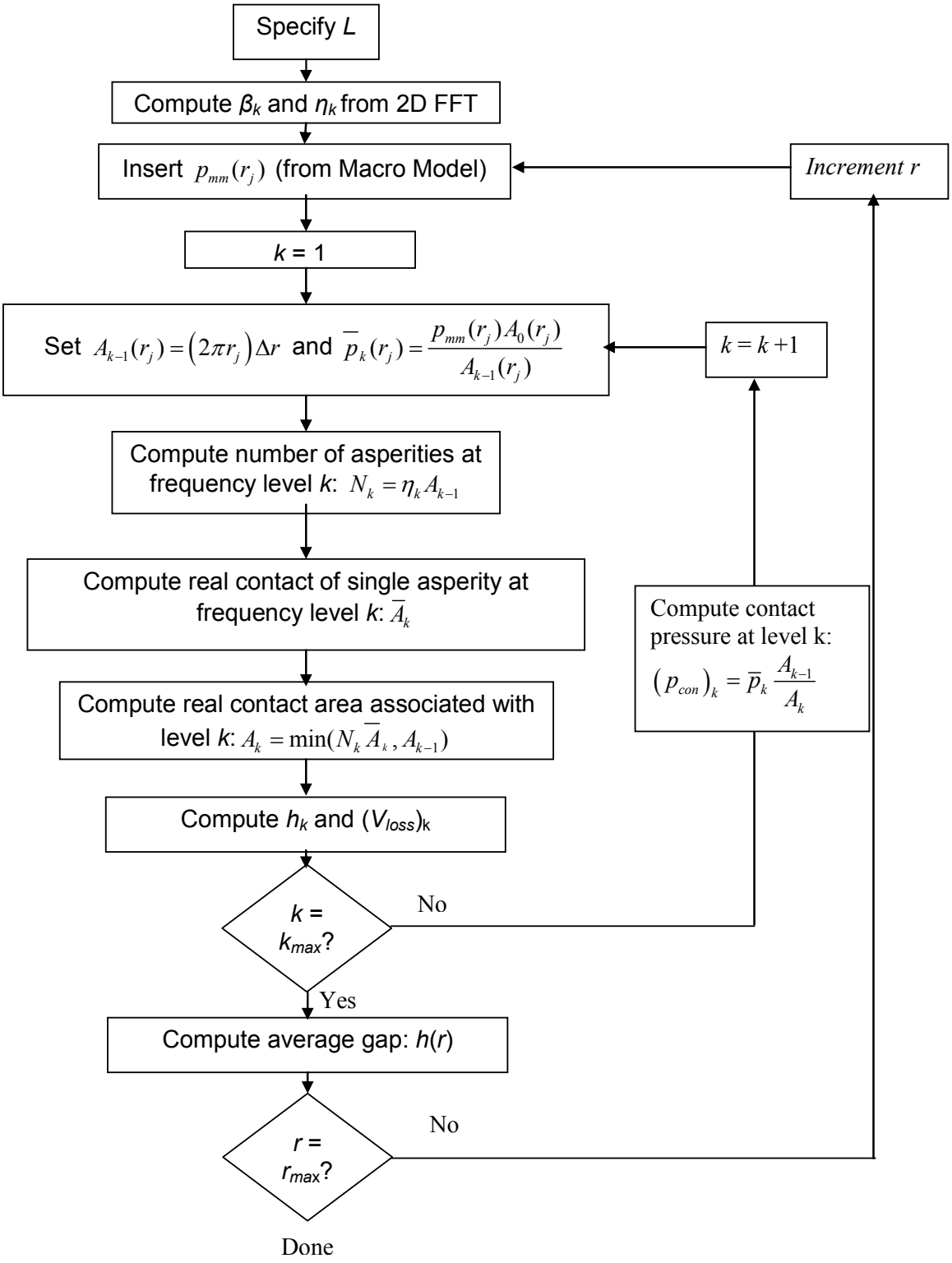

Figure 7 : Flow chart of steps involved to approximate average gap using the Jackson-Streator model (Elastic-Plastic deformation).

6. LEAKAGE EXPERIMENTS

6.1. Experimental Study Overview

Leakage experiments were conducted in parallel with the leakage modeling presented in the two preceding chapters. Two sets of comprehensive leakage studies were performed. The first set of leakage experiments was carried out using a metal-metal compressive seal, which featured a single leakage interface and a machined stainless steel substrate, while the second set of leakage experiments was conducted on phlogopite mica using a conventional compressive arrangement as is depicted in Figure 8. It has been demonstrated via experiment [15] that secondary leakage paths are present between mica interlayers, while primary paths are located at the mica-Inconel interface and the mica-alumina interface, respectively.

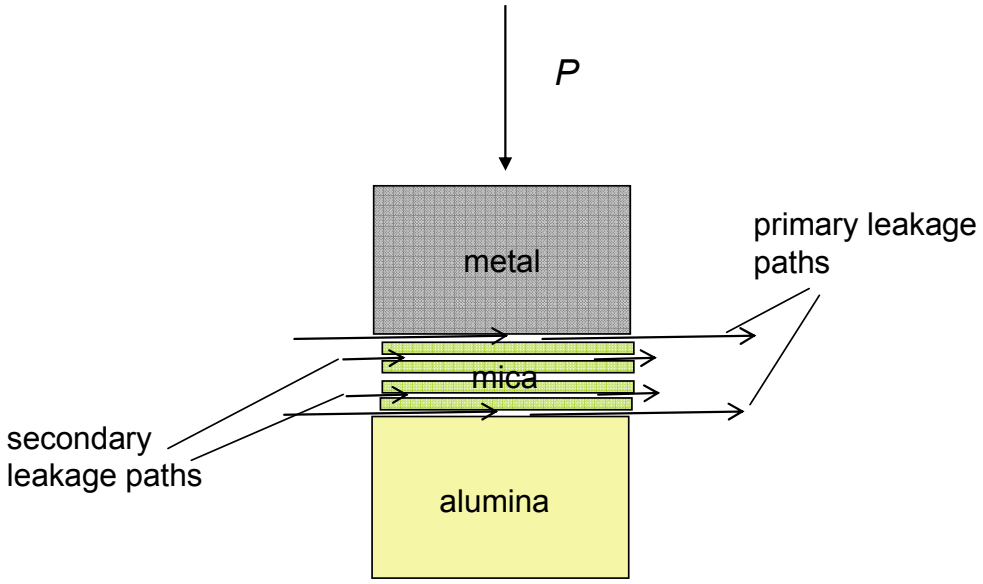

Figure 8: Depiction of conventional mica-based compressive seal configuration.

The metal-metal compressive leakage experiments were critical because these studies not only provided insight regarding the role of surface roughness, compressive load, and temperature, but they also helped to demonstrate the effectiveness of the modeling approach without having to address the complexity of predicting leakage in multiple interfaces or attempting to capture mica's complicated microstructure.

Once the role of compressive load was adequately understood through metal-metal compressive seal studies, it was decided that load should be held constant in the subsequently presented mica-based compressive seal study. The focus of that study was to assess leakage in several interfaces, and more specifically, ascertain how the number of leakage paths impacts leakage rates in a state-of-the art compressive seal. Unlike the previous case, the surface

roughness of the mica was not altered. As result, the role of surface roughness is not analyzed in the latter studies.

The next section will discuss the main features of the leakage apparatus. After that, the experimental procedure used in the leakage experiments is detailed. Once the procedure is presented, a detailed description of the leakage apparatus components is discussed along with instrument calibration and component alignment. The experimental procedure is included along with the process for determining the experimental leakage results. Lastly, sample preparation is discussed for the stainless steel and the mica-based seals, respectively.

6.2. Leakage Apparatus

A schematic of the leakage apparatus is included as Figure 9. An alumina rod connected to the pneumatic loading apparatus is inserted into the top receptacle of the Inconel workpiece, while the bottom portion of the said workpiece, which has an annular shape, is used to load the substrate. The Inconel workpiece is the centerpiece of the leakage apparatus, and is multifunctional in nature. As depicted in Figure 9, a 300 cm^3 cylindrical volume, which is denoted as the known volume in the said figure, is filled with test gas via the connectors attached to the Inconel workpiece. During the filling of the known volume, both Valve A and Valve B are opened so that pressurized gas through the Inconel workpiece towards the entrance of the cylindrical known volume.

During the discharging of the known volume, Valve A is shut and test gas enters from the right side of the Inconel workpiece, and then flows down the portion of the flow channel that coincides with the work piece's axis of symmetry. Eventually, test gas escapes into the ambient surroundings after traversing across the annular sealing zone. As observed in Figure 10, the Inconel workpiece was designed to apply a compressive load at the center of ceramic furnace, while also allowing gas to safely flow through the workpiece. Returning to Figure 9, the height of the test piece was determined so that the horizontal portion of the T-shaped flow channel was tall enough to extend beyond the cylindrical furnace and foam insulation unencumbered. Two ¼ inch male-to female connectors were welded to the inlet and exit corresponding to the top portion of the T. The connectors were welded to preclude gas from potentially leaking when the substrates were replaced.

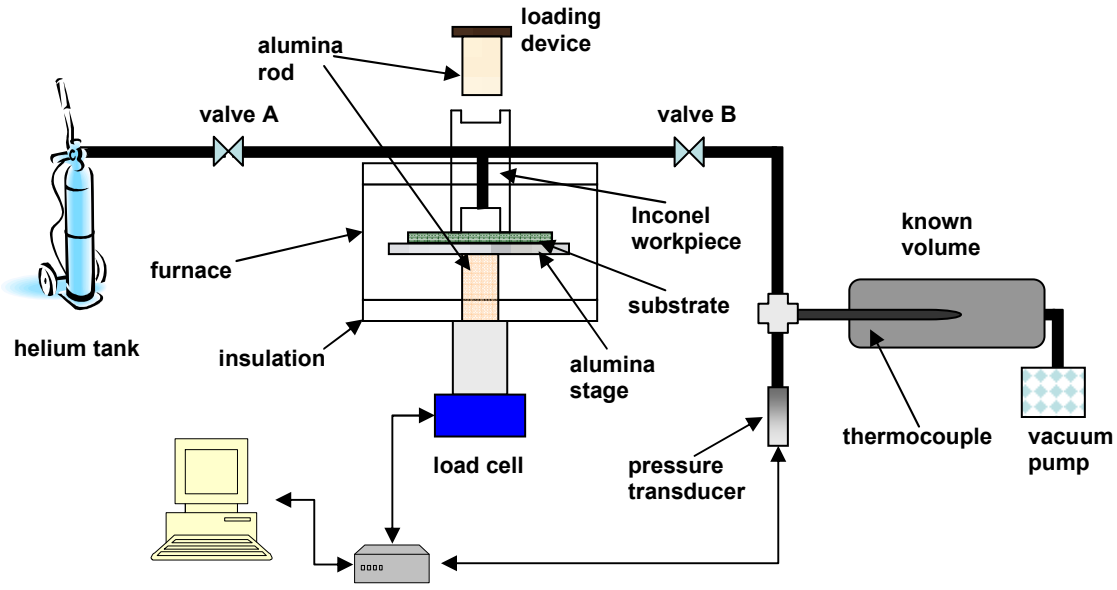

Figure 9 : Experimental apparatus used for leakage testing.

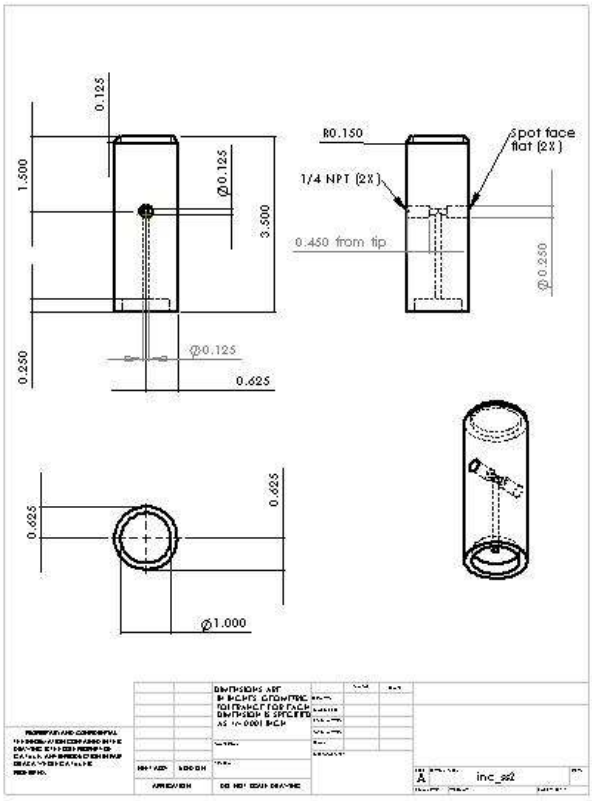

Figure 10: Inconel workpiece used for applying compressive load and circulating test gas during leakage experiments with dimensions in inches.

Stainless steel piping was used to connect all pneumatic components in the leakage apparatus. The ¼ inch stainless steel tubing was chosen specifically, because it is robust and could withstand the heat being conducted through the Inconel work piece without deforming when the furnace is activated. In addition, the diameter of the tubing was small enough so as to reduce the background leakage loss associated with the various connectors. The corresponding background leakage was determined at a differential pressure of 2 kPa to be 0.0527 standard cubic centimeters per minute (sccm).

A ¼ inch male-to-male four-prong cross shaped compression fitting connector is included upstream from the aforementioned Inconel workpiece to attach the differential pressure transducer, thermocouple and cylindrical known volume. The cross connector allows the three components to be joined in parallel. Along the horizontal axis of the T-connect a thermocouple is inserted in the left hand side and extends along the central axis of the known volume stopping in the middle of the said volume lengthwise. The thermocouple is held in place using a threaded cap that also prevents test gas from leaking out the left side of the cross connector. Along the vertical axis of the cross connector, a differential transducer is attached to the bottom to monitor the differential pressure change in the known volume.

The cylindrical known volume has both an NPT threaded inlet and exit. One ¼ inch male-to-male compression to NPT fitting is used to connect the cross connector to the inlet of the said volume. An additional ¼ inch male-to-male compression to NPT fitting is inserted at the far end of the known volume so that a vacuum pump can readily be attached and detached. A sealable release mechanism is attached on the free end of the NPT fitting so that the vacuum pump can be detached without allowing air to seep into the known volume. This mechanism also prevents air from escaping out the exit port of the known volume once it has been pressurized.

Although not critical for determining leakage, several auxiliary components were added to the leakage apparatus to ensure it was robust and experimental conditions could be repeated as desired. To reduce the likelihood of any of the

instrumentation being damaged, particularly the load cell and MTS machine, cooling blocks were incorporated to re-circulate chilled water. Aluminum cooling blocks were added to the system to ensure heat was not transferred to the load cell as depicted in Figure 11, while another cooling block was incorporated near the loading device as depicted in Figure 12. A woven sheath surrounds the compression tubing used to re-circulate the chilled water protecting it from the heat. Threaded transitional connectors were required so that cooling blocks could be inserted between the load cell and the MTS machine respectively. In order to reduce the likelihood of the pressure transducer being overloaded, a flow restrictor device and pressure gauge was placed just before Valve A. Great care was taken to ensure the leakage apparatus, which is depicted in Figure 13, provides accurate and reliable leakage measurements, while eliminating excessive background leakage, damage to compression tubing and electrical components due to excessive heat, and unwanted moments due to unbalanced loading. In the upcoming two subsections, instrument calibration and component alignment is discussed.

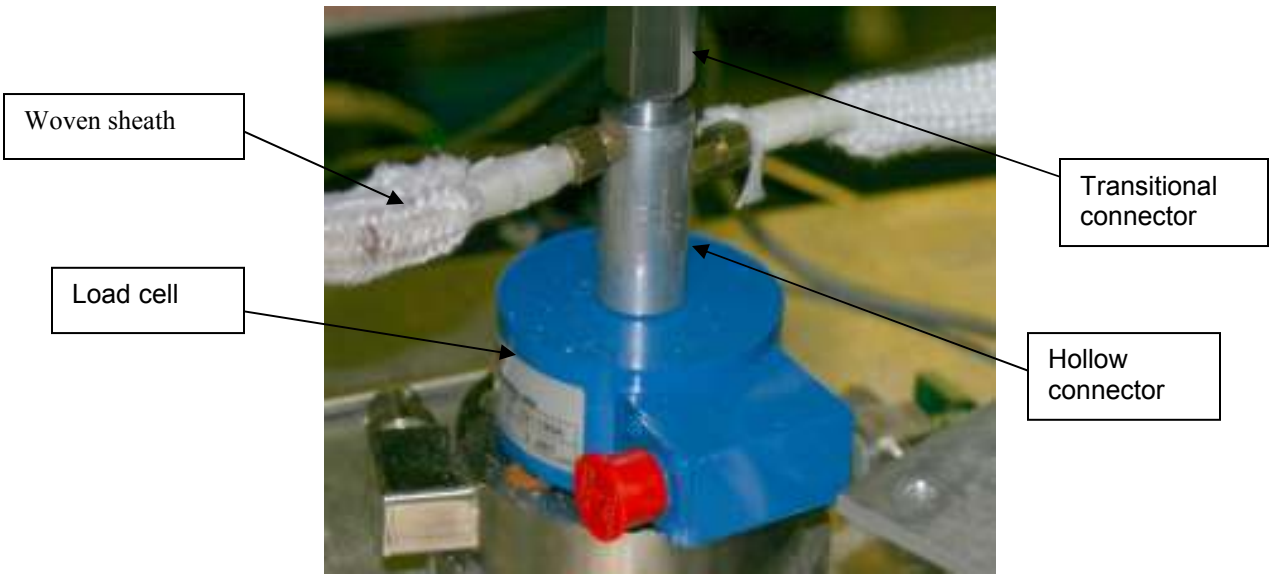

Figure 11: Depiction of hollow cylindrical connector used to prevent heat from damaging load cell.

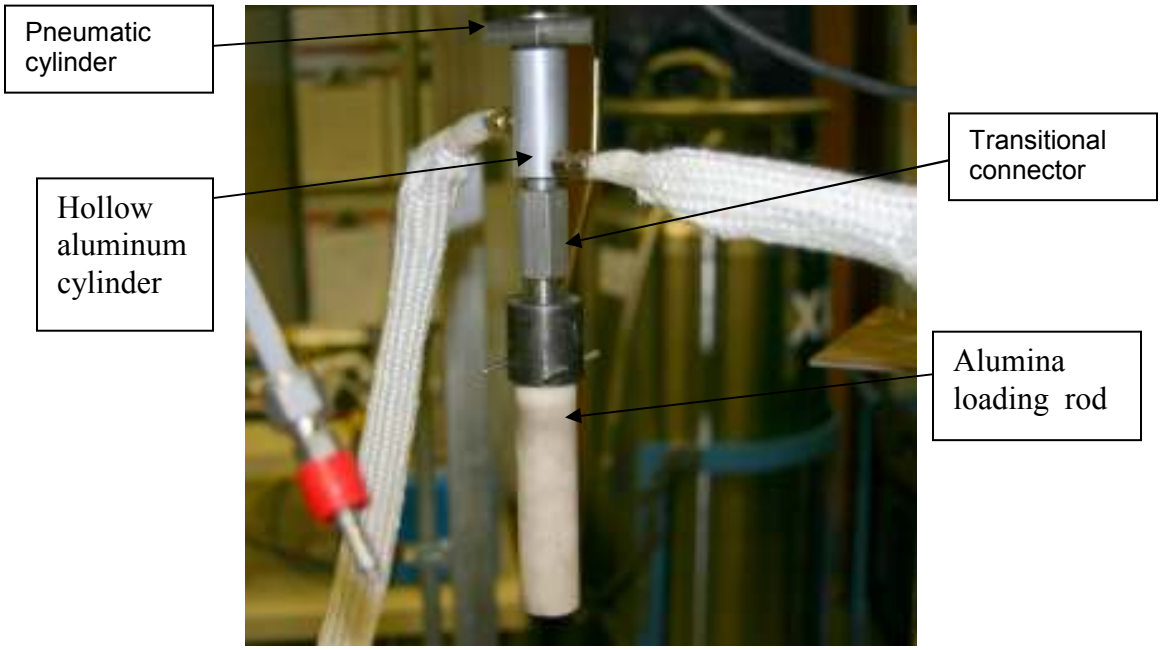

Figure 12: Depiction of hollow cylindrical aluminum block affixed MTS loading machine. Temperature controlled water is re-circulated to reduce heat exposure outside of furnace heating zone

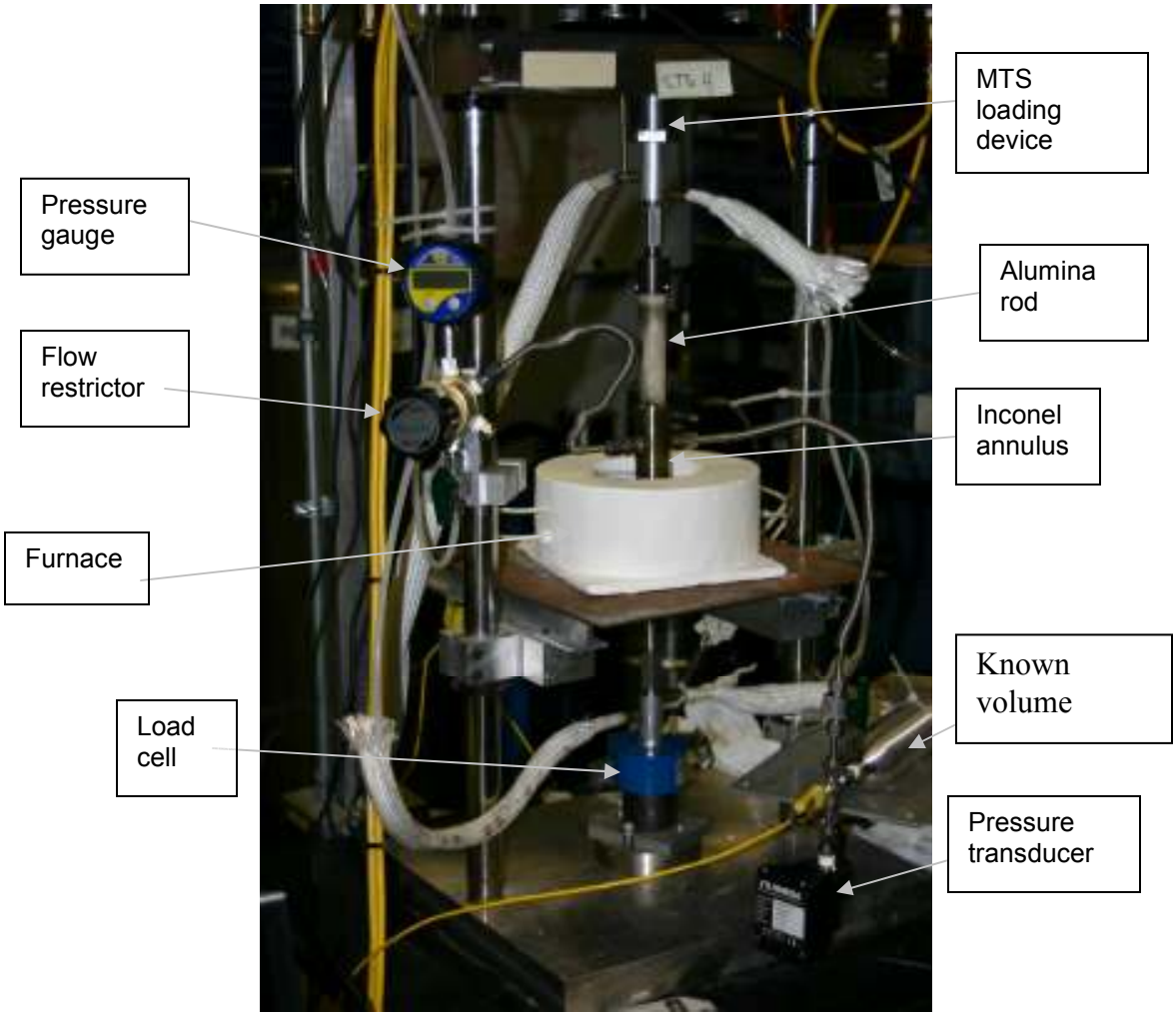

Figure 13: Depiction of the actual leakage apparatus used for investigating leakage in compressive seals.

6.2.1. Instrument Calibration

In order to achieve consistent, reliable leakage measurements several steps were taken. First, the load cell, the 1-psig- differential pressure transducer, and thermocouples all needed to be calibrated. A 300-lbf capacity load cell

manufactured by Interface Model 1110ACK-300 with a listed nonlinearity of 0.03 % full scale was used throughout the leakage analysis.

The load cells were calibrated by first zeroing out the cell, when no mass was present, and then the voltage output was recorded for varying denomination of weights. The corresponding calibration measurements determined prior to testing is included as Table 1 with the consequent voltage as a function of load curve included as Figure 14. Based on the regression line, there is a measurement uncertainty of ± .0021 volts per pound load.

Table 1: Summary of 300-lb_f capacity calibration measurement taken prior to leakage study.

Load (lb_f)	Voltage (V)
0	0
5	5.03
10	9.99
20	19.98
40	39.96
50	49.97
60	59.94

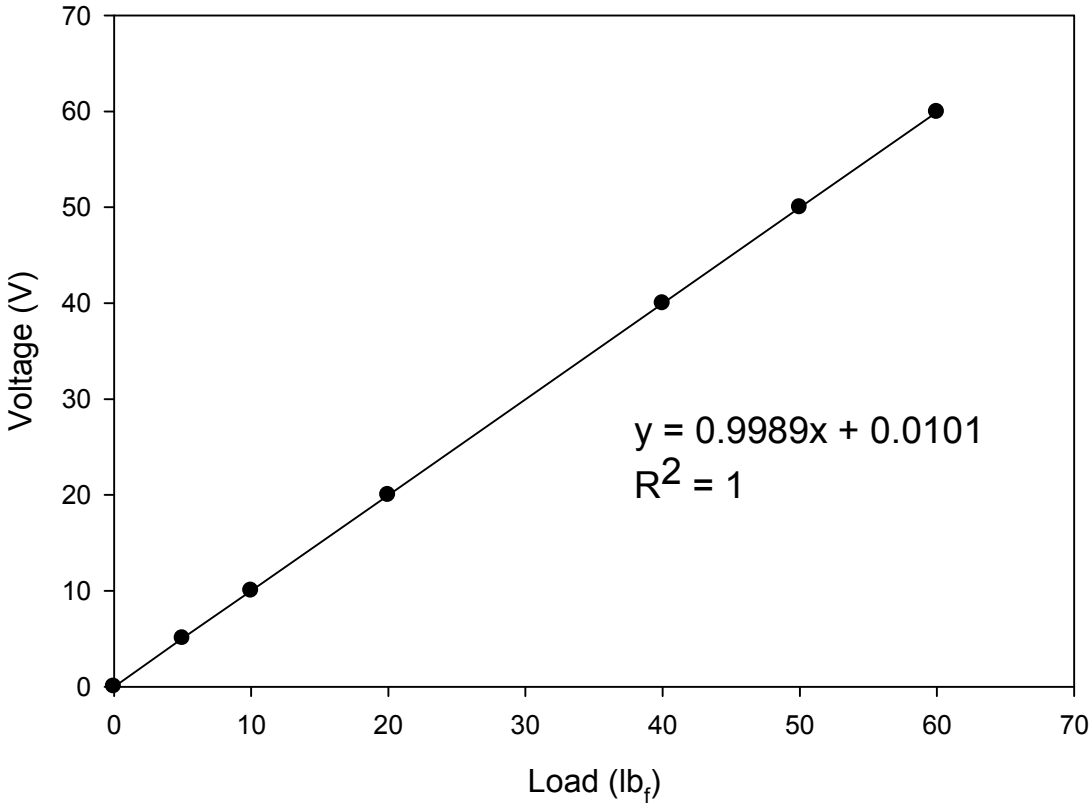

Figure 14 : Voltage versus load calibration curve

A similar procedure was performed on the Honeywell Sensotec 1-psig-differential pressure transducer whose model is FP2000. Since a differential pressure transducer is used, one port is exposed to the surrounding atmospheric air, while the other port is attached to the bottom portion of the cross connection at the inlet of the known volume as shown in Figure 15. Per the product manual, the transducer was then connected appropriately. Transducer voltage output was scaled to read in terms of pounds. To validate the transducer output, a pressure gauge was connected in series with the pressure transducer. A flow

restrictor was then used to adjust the flow rate in the line and the two measuring device readings were compared. LabView was used to adjust the pressure transducer settings for optimal performance.

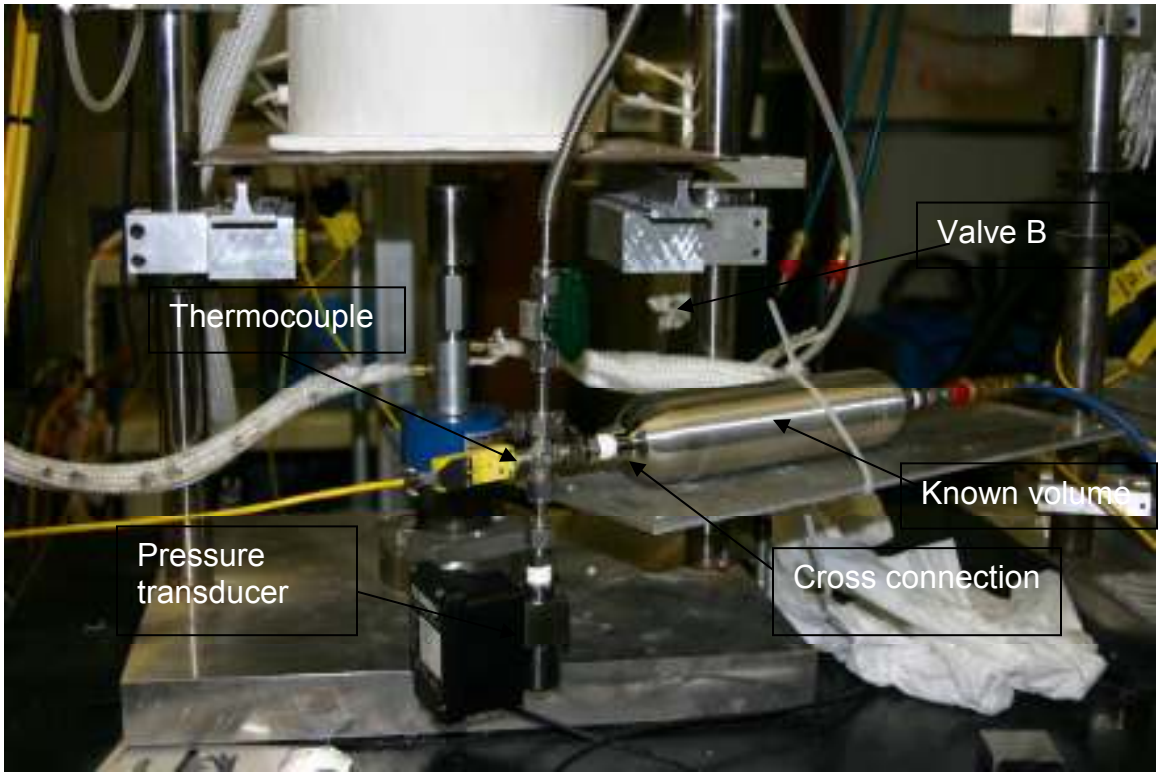

Figure 15 : Depiction of cross connection used to connect the pressure transducer, thermocouple, and inlet line to the known volume.

The thermocouples along the axial center of the known volume and within the sealing zone were calibrated as well. The LabView data acquisition card allows for each to be setup by specifying the type and the operating temperature range. Minor modifications to the load parameters were made to ensure acceptable performance.

6.2.2. Component Alignment

Loading is an essential element for achieving adequate resistance to fluid flow in a compressive seals. In order for the said seal to operate effectively, the compressive load should be applied perpendicular to the interface of interest, and the axial centers of the annulus and substrate should be aligned to eliminate unwanted transverse moments, which facilitate excessive leakage. Several steps were taken to ensure proper loading occurred during the leakage experiments. First, an aluminum adjustment block was designed and fabricated to ensure that the load cell and the Inconel annulus were aligned. Returning to Figure 9, since several of the components, including the alumina rod and stage, were connected and extend along the central axis of the load cell base, it was incumbent that the loading rod contacted the center of the stage as closely as possible to prevent the stage from tipping. A movable adjustment block, which is depicted in Figure 16, was used to position the load cell along a common central axis. The circular holes at the midsection of the block was used to mount the load cell in place, while the antisymmetric U- shaped cutouts were used to secure the base and all of the components connected above it to the steel test frame. The alumina loading rod was fixed, but was extended while inserted in the Inconel workpiece as closely as possible to the alumina stage to fine tune the positioning of components. Once the movable base was aligned and secured properly so that the axial centers of the loading rod and the alumina cylinder attached to the load cell were aligned, the alumina stage could then be seated snugly on top of the alumina support with no change in its orientation. A small

compressive load was then applied using the mechanical tester to verify no shifting occurred once the annulus contacted the alumina stage. It is important to note during the loading process, when the rod connected to the loading device is lowered into the Inconel's top cavity the Inconel is free to self-align since no rigid connections are present. A second alumina rod, which is connected to the load cell in Figure 9, is inserted in a receptacle at the axial center underneath the stage. Once loaded, the stage self-aligns in a similar fashion as the Inconel workpiece described above. Proper centering of the Inconel workpiece with the alumina stage ensures that the substrate will be loaded evenly provided it is centered on top of the alumina stage.

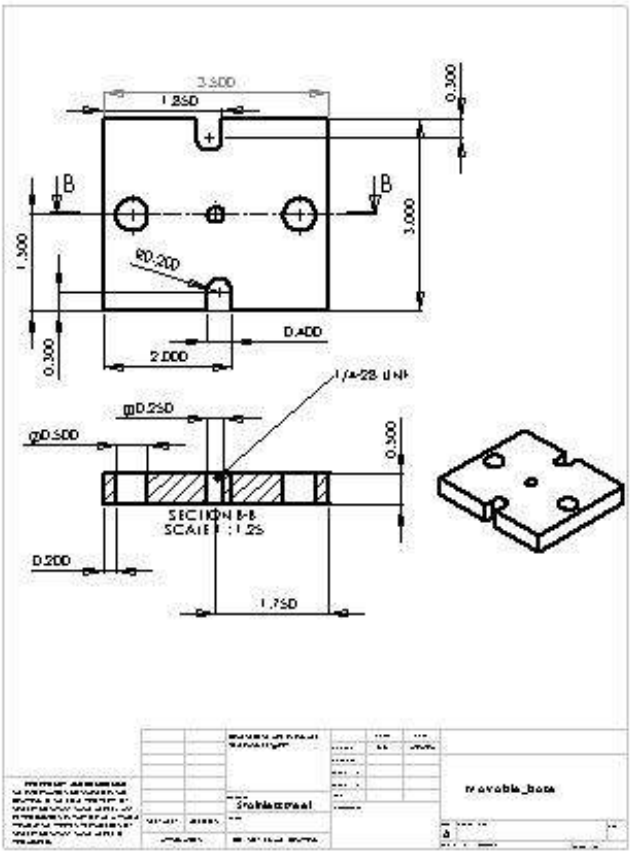

Figure 16: Drawing used to fabricate movable base for load cell alignment with dimensions in inches.

6.3. Experimental Procedure and Leakage Determination

In this section, a detailed experimental procedure is outlined for investigating leakage in a compressive seal assembly. The procedure is identical for both the mica-based and metal-metal compressive seals. A depiction of the essential components of the leakage apparatus was included in the previous section as Figure 13. The 300 cm^3 cylindrical known volume is kept at ambient

conditions and is connected to the Inconel tube via a 6.35 mm diameter stainless steel tube. The leakage experiments are conducted as follows:

1. The previously mentioned known volume is then evacuated using a vacuum pump. The resulting pressure within the reservoir is recorded.
2. Valves A and B are then opened. After the gas supply tank is opened, the flow regulator is used to safely pressurize the known volume to approximately 0.500 psig. Valve B is closed once the desired pressure in the known volume is reached. (Since the subsequent leakage results were determined at 0.27 psig, the tank is pressurized above the target pressure so that the fluid pressure has sufficient time to equilibrate as the reservoir discharges.)
3. If testing is desired at temperatures higher than room temperature, the ceramic cylindrical furnace is positioned to heat the sealing zone to the predetermined set point, and is maintained at the given temperature using a PID controller. Moreover, the furnace is centered relative to the interface so as to reduce the likelihood of thermal variation at the seal interface. Two thermocouples reside within the interior of the furnace, and are oriented as closely as possible to the sealing zone prior to the onset of heating. The measurement thermocouple's readings are recorded in real-time,

while an over–temperature thermocouple's readings are used to adjust the energy output supplied to the ceramic furnace.

4. Once the temperature remains within 5 degrees of the desired temperature for 15 minutes, a LabView program is then used to begin recording data and apply the desired static load at the annular interface is applied as shown in Table 2. Note: Prior to applying the load, the load cell was zeroed out so that the substrate's weight is not included in the load measurement.
5. Referring back to Figure 9, Valve A is then closed, and shortly after, Valve B is opened. The pressurized vessel is then allowed to discharge for approximately 3 minutes. A differential pressure gauge is then used to monitor the change in the differential pressure.
6. The reservoir temperature, furnace temperature, reservoir pressure, total compressive load, and time elapsed are recorded at a sampling rate of a single measurement every 0.25 seconds.
7. All data sampling and loading cease after 180 seconds have elapsed.

Table 2: Summary of the applied load used to yield the desired average compressive stress in the annular contact zone.

Sy (psi)	P(lbf)
100	44.18
200	88.36
300	132.54
400	176.71
500	220.89

For a given leakage experiment, the differential pressure as a function of time can be determined, and a representative plot is given as Figure 17 . Per the figure, the differential pressure is initially constant. There appears to be some transience as indicated by the change in slope just after the differential pressure begins to drops. This corresponds to the instant immediately after Valve B is opened and the test gas begins filling the evacuated flow channels outside the known volume as shown in Figure 9. Once the pressure of the channel and known volume equilibrates, the slope of the differential profile changes again, except this time it decays monotonically in an orderly fashion until the test is completed.

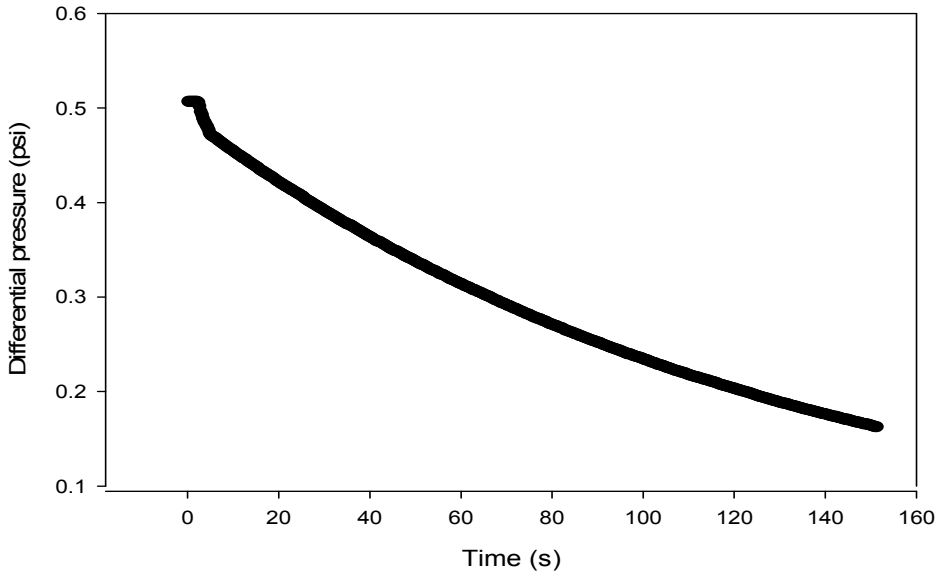

Figure 17: Differential pressure in compressive seal assembly as a function of time.

By assuming the test gas is an Ideal gas, the leakage rate is eventually determined by relating the slope of the above figure to the volumetric leakage rate. The ideal gas assumption is reasonable since the fluid pressure is no more than 3.5 kPa above atmospheric pressure, and the experimental temperature ranges from 25 to 500 °C. The low pressure and operating temperature conditions are suitable for employing the aforementioned idealization. Starting with the Ideal Gas equation of state and solving for mass, one can easily derive an expression for the volumetric rate by simply differentiating the resulting expression for mass with respect to time and dividing the aforementioned by the density of the fluid, the resulting volumetric leakage rate, q, is determined as follows:

$$q = \frac{V}{\rho RT}\frac{dp}{dt} \tag{31}$$

where *V* is the reservoir volume, *R* is the gas constant for the fluid, *T* is the absolute temperature, and *dp* is the differential change in pressure, and *dt* is the differential change in time. First order divided difference methods base on Taylor series approximation were to determine $\frac{dp}{dt}$. A forward difference and backwards difference approximation of the first derivative is applied to the first and final time steps, respectively. A central difference approximation of the first derivative is applied to determine $\frac{dp}{dt}$ at the interior intervals. Four pressure data points were recorded per second with leakage tests lasting a minimum of 180 seconds. Thus, each pressure profile has at least 720 sample points. Once the leakage rate at each discrete data point in the sampled set, the leakage rate corresponding to when the differential pressure is 2 kPa is recorded. If none of the experimental data points are within 0.001 of the desired pressure value, the leakage corresponding to a differential pressure of 2 kPa is linearly interpolated in between the two points that encapsulate the target pressure.

6.4. Sample preparation

In this section, it is explained how samples are prepared for testing. There were two compressive seal configurations that have been investigated – a metal–metal compressive seal and a mica-based compressive seal. As its name

suggests, the former only consists of metallic subcomponents. Moreover, all of the metal-metal compressive seal leakage studies involve a single leakage interface. A common grade stainless steel (e.g. SS 316) was machined so that the effect of surface roughness on leakage could be investigated. Prior to testing, the stainless steel test specimens were lapped using 100 grit and 600 grit work pieces, respectively. In addition, each specimen's thickness was verified to be machined within ±0.0254 mm (.001").

In the case of mica-based compressive seals, the phlogopite mica sheets were cut into 1.5" by 1.5" squares with a 0.5" diameter hole cut in its center as depicted in the engineering drawing of the phlogopite layer included as Figure 18. Prior to applying the compressive load, all mica layers for the given mica-based compressive seal were centered and then stacked on top of one another. Moreover, the phlogopite squares were stacked so that a given compressive seal configuration yielded one, two, or as many as five leakage paths as indicated by the specifications associated with that particular run.

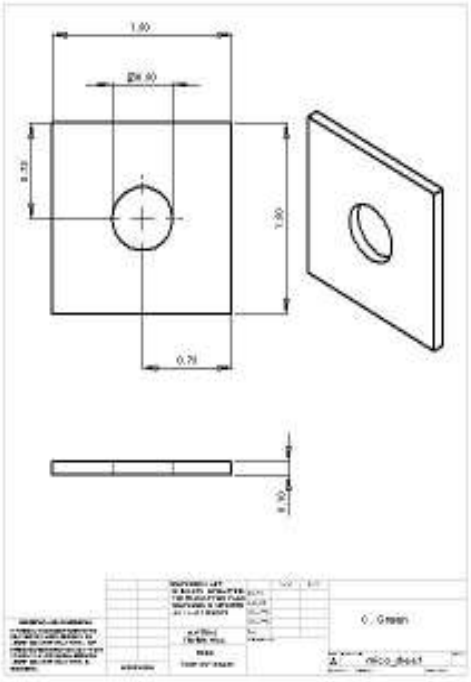

Figure 18: Processed mica layer used in leakage experiments.

Both the phlogopite and the stainless steel substrates were inspected via microscope prior to testing to ensure each was free of large-scale defects that could potentially dominate the leakage characteristics of the compressive seals. Since the mica layers were thin, they were inspected often to ensure the paper was not ripped during loading. The stainless steel, on the other hand, was inspected for scratches.

6.5. Surface Characterization

Surface roughness scans were an integral part of the modeling approach. Recall, the Jackson-Streator model uses Fast Fourier transforms to approximate the surface separation at a given frequency level. After a 3-D surface scan is

performed, the surface height and its corresponding surface coordinates can then be transformed into its corresponding frequency spectrum. The parameters used in each of the three dimensional surface roughness scans are included as Table 3. A Rodenstock RM600 Laser Surface Mapping System was used to map the topography of the stainless steel substrates and mica. The vertical resolution of the aforementioned laser profilometer is .01 microns, while the vertical measurement range was set to ±300 microns as indicated by Table 3. The aforementioned range was selected to ensure higher asperity peaks could be detected. The scan length in the x and y directions was 16 mm, which was chosen because it is slightly larger than the outer radius of the Inconel annulus. There were a total of 256 line scans with 256 points in each scan, which yields 62.5 microns in between adjacent points. The speed for each scan was set to 80 mm/min, with each scan taking approximately 1 hour to complete, which happened to be the maximum scan speed available per the previously specified number of points per line scan.

The “flatness” of the stainless steel substrates could then be approximated using the highest amplitude from the frequency spectrum. First, a curve fit is performed on the amplitude versus frequency plot for a given substrate. Next, the highest measured amplitude was noted, which was determined relative to a scan length of 16 mm and whose corresponding frequency is 62.50 cycles/meter. The resultant curve fit equation is then used to extrapolate to a spatial frequency of 31.25 cycles/meter with a corresponding extrapolated scan length of 32 mm. Since the extrapolated scan length is slightly larger than the outer diameter of the

Inconel annulus, it is an excellent metric for the flatness of the substrate across the entire annular sealing zone.

Table 3: Areal surface roughness scan parameters used for surface characterization

Range	x- length	y-length	Points	Scan	Speed
300 μm	16 mm	16 mm	256	256	80 mm/min

Surface roughness scans were performed prior to the first load for the metal-metal compressive seal leakage study. The three compressive loads used throughout the study were 100, 300 and 500 psi, respectively, which corresponds to the average pressure applied at the annular interface. Since there were two surface finishes, each battery of leakage tests had a total of at least two surface roughness scans. In addition, each substrate was marked so that a given substrate could be oriented in the same manner for each scan. Before performing the ¼ areal surface scan, the zero point for a given specimen, which was the center point in the square substrate, was saved as the referenced starting point. After that, each scan could then be performed per the parameters included in Table 3.

6.6. Experimental Effective Gap

The determination of the average surface separation across the entire contact sealing zone is critical in predicting leakage. As suggested by Equation

(21), the mass flow rate is roughly proportional to $h^3(r)$. Thus, approximations for *h* should be reasonably close to reality; otherwise there will be substantial over-predictions or under-predictions of leakage. Since there is no way to directly measure the gap during a leakage test, we present a means to determine the average, or effective, gap across the entire annular sealing interface by using experimental leakage calculations in conjunction with the mixed lubrication based gas flow model. By replacing the nodal values for *h* with their respective average values over the annular contact zone, the variable portion of the denominator in Equation (21) may be rewritten as follows:.

$$\int_{r_i}^{r_o} \frac{dr'}{\phi(r')r'h^3(r')} = \frac{1}{\Phi_{eff} h_{eff}^3}\left[\ln\left(\frac{r_o}{r_i}\right)\right] \tag{32}$$

where Φ_{eff} is the average isotropic pressure flow factor over the entire annular region, and by its very definition is a function of h_{eff}. By substituting Equation (32) into Equation (21), it follows that

$$\dot{m} = \frac{-\pi {p_o}^2\left(1-\left(\frac{p_i}{p_o}\right)^2\right)}{12\mu RT\dfrac{1}{\Phi_{eff} h_{eff}^3}\left[\ln\left(\frac{r_o}{r_i}\right)\right]}. \tag{33}$$

Now, the absolute pressure as a function of r can be expressed as

$$p(r) = p_{atm} + \Delta p\,. \tag{34}$$

For each study, the pressure at the inner and outer radii may be written as $p_i = p_g$ and $p_o = p_{atm,}$ respectively, where p_g is the gauge pressure reading taken from the pressure transducer. Using the aforementioned and algebraic manipulation, Equation (33) may be rewritten in terms of $p_{o,}$ and Δp exclusively:

$$\dot{m} = \frac{-\pi p_o{}^2 \left(\frac{2\Delta p}{p_o} - \left(\frac{\Delta p}{p_o} \right)^2 \right)}{12\mu RT \frac{1}{\Phi_{eff} h_{eff}^3} \left[\ln\left(\frac{r_o}{r_i} \right) \right]}. \tag{35}$$

Solving for $\Phi_{eff} h_{eff}^3$, it can be shown that

$$\Phi_{eff} h_{eff}^3 = \frac{-12\mu RT\dot{m} \left[\ln\left(\frac{r_o}{r_i} \right) \right]}{\pi p_o{}^2 \left(\frac{2\Delta p}{p_o} - \left(\frac{\Delta p}{p_o} \right)^2 \right)}. \tag{36}$$

Applying the definition of Φ_{eff}, it follows that

$$f(h_{eff}) = \left[1 - 0.9e^{-\left(\frac{0.56 h_{eff}}{\sigma} \right)} \right] h_{eff}^3 = \frac{-12\mu RTQ \left[\ln\left(\frac{r_o}{r_i} \right) \right]}{\pi p_o{}^2 \left(\frac{2\Delta p}{p_o} - \left(\frac{\Delta p}{p_o} \right)^2 \right)}. \tag{37}$$

Equation (37) can then be solved numerically for the effective gap. This value is then compared with arithmetic mean of the nodal value of the average gap as computed from the micro-contact models (see Equation (5)).

7. LEAKAGE RESULTS- ELASTIC ONLY MODEL COMPARISON

7.1. Elastic Only Overview

In this chapter, the elastic-only computational leakage model predictions are compared to leakage tests. A metal-metal compressive configuration with a single interface is used throughout the leakage study, and the working fluid used in this study was purified Helium. The two stainless steel substrates used in this analysis have not been loaded or exposed to heat prior to this leakage study.

A battery of leakage tests was conducted, and the test matrix of the leakage study is included as Table 4. Each row or test combination was performed three times. The average applied compressive stress in the annular contact zone is denoted by p_{comp}, while the seal interface was heated to the temperature specified in Table 4. Both the English and SI-equivalent applied compressive pressures are included in the aforementioned.

Table 4: Summary of temperature, surface roughness, and compressive loading conditions used in metal-metal compressive seal leakage experiments.

Sample	p_{comp} (psi)	p_{comp} (MPa)	T (°C)
100 grit	100	0.689	25
100 grit	300	2.067	25
100 grit	500	3.447	25
100 grit	100	0.689	250
100 grit	300	2.067	250
100 grit	500	3.447	250
100 grit	100	0.689	500
100 grit	300	2.067	500
100 grit	500	3.447	500
600 grit	100	0.689	25
600 grit	300	2.067	25
600 grit	500	3.447	25
600 grit	100	0.689	250
600 grit	300	2.067	250
600 grit	500	3.447	250
600 grit	100	0.689	500
600 grit	300	2.067	500
600 grit	500	3.447	500

A table of the physical parameters used throughout the leakage analysis is included as Table 5, while Table 6 is a collection of the temperature-dependent properties used for the present leakage study. The size of the annular region and the differential pressure, Δp, were chosen in accordance with the experimental procedure outlined by Chou and Stevenson[12]. Since the metal-metal seal was comprised of an Inconel annulus and SS 316 machined substrate, the appropriate thermo-elastic properties including the elastic modulus, Poisson's ratio, and coefficient of thermal expansion were selected from material property handbooks [57]. Several surface roughness parameters were determined from the surface roughness scans of the two stainless substrates, these roughness parameters are included in Table 7. According to Table 7, the difference between the h_{max} and c_{max} in the 600 grit substrate is negligible. However, there is a substantial difference in the two aforementioned quantities in the 100 grit surface, which would dramatically impact leakage predictions given q is proportional to h^3.

Table 5: Parameters used to approximate leakage using computational leakage model.

Parameter	Value
R	208 kJ/kg K
r_i	12.70 mm
r_o	15.875 mm
Δp	2.0 kPa
v	0.22
E^*	99.42 GPa

Table 6: Temperature-dependent properties used in elastic only leakage study [58]

T (°C)	μ (Pa*s)	Sy (MPa)	ρ(kg/m^3)
25	1.9793E-05	207	1.634
250	2.9788E-05	190	0.931
500	4.0893E-05	180	0.630

Table 7: Summary of surface roughness characteristics for the two surface finishes.

Sample	S_q (μm)	h_{max} (μm)	c_{max} (μm)
100 grit	22.96	109.94	74.66
600 grit	1.54	7.53	7.59

7.2. Elastic Only Model Results and Comparison

After the load was prescribed, the macro contact model was then used to determine the pressure distribution. Figure 19 is a depiction of the contact pressure in the contact zone. From the figure, it follows that the nodal pressure values are highest at the inner and outer radii of the annulus. The behavior of the pressure profile at these two locations indicates the presence of stress concentrations due to infinitely sharp corners.

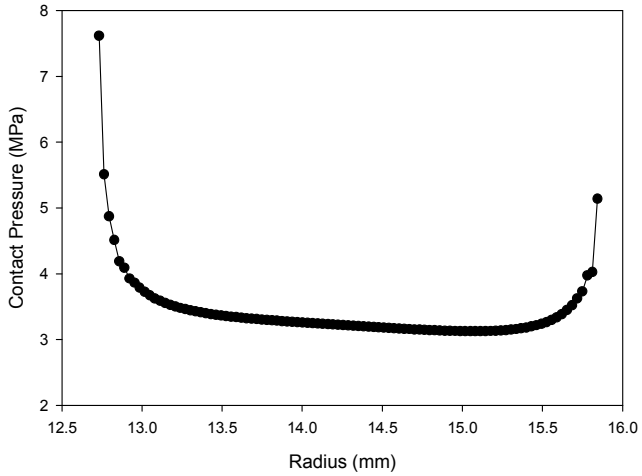

Figure 19: Pressure distribution of metal-metal compressive seal with p_{comp}= 500 psi and T= 25 °C.

From the micro contact model, a relationship is established between the local pressure and the nodal surface separation. A single surface roughness scan is performed on each substrate prior to the leakage study. The corresponding 100 grit and 600 grit surface roughness scans used in this study are included as Figure 20 and Figure 21, respectively. Both scans have isolated peaks. The 100 grit maximum surface height is over 109.94 microns, while the 600 grit substrate's maximum surface height is only 7.53 microns. Prior to approximating the nodal separation, a 2D FFT was performed on the aforementioned surface scans in an effort to convert the surface heights and spatial coordinate information into amplitude and frequency data for a given seal configuration. A representative plot of the frequency spectrum for the 100 grit substrate is included as Figure 22. As indicated by the figure, amplitudes

decrease in an oscillatory fashion as frequency increases. After the aforementioned spectrum is determined, a relationship can be established between spectrum and average surface separation; that is, the JS model is then applied recursively up through the Nyquist frequency to determine the reduction in surface separation at a given nodal location.

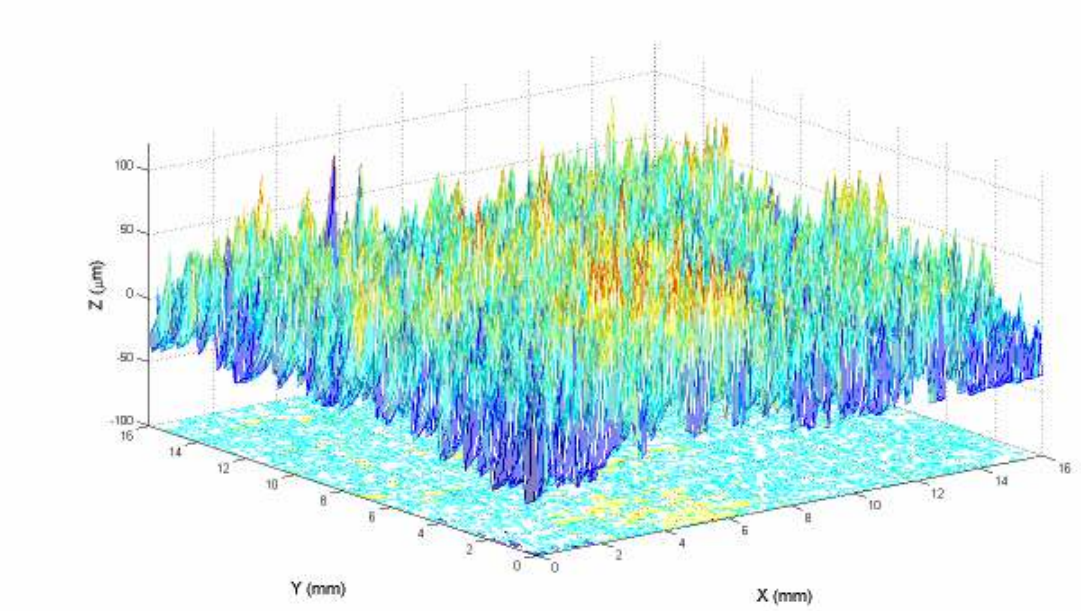

Figure 20: Surface roughness scan of lapped 100 grit stainless steel substrate taken prior to loading (elastic only study).

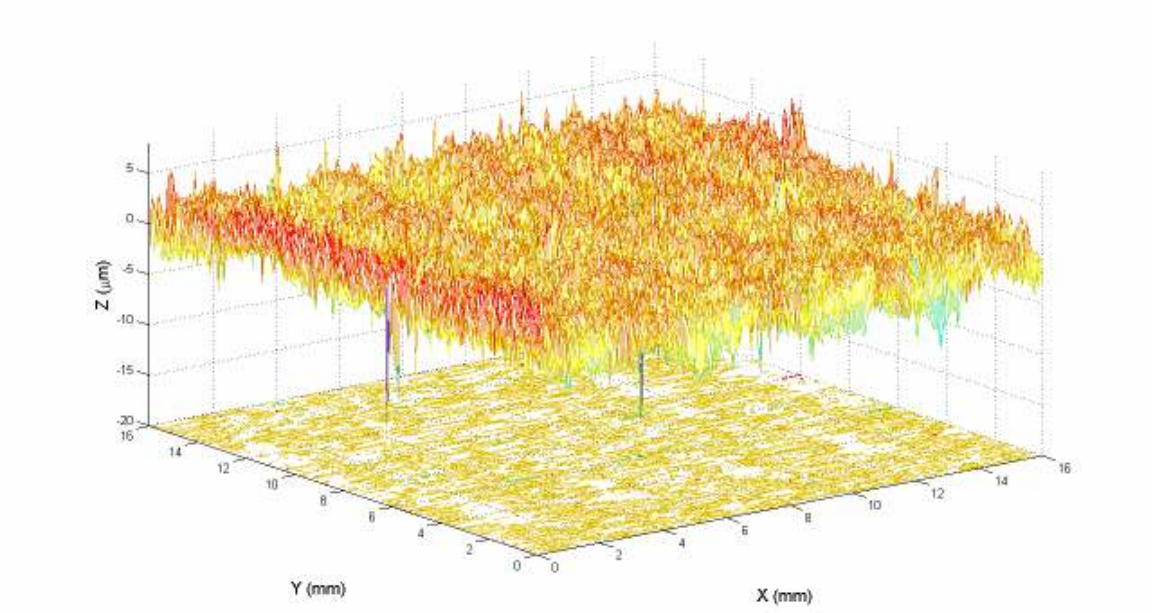

Figure 21: Surface roughness scan of lapped 600 grit stainless steel substrate prior to loading (elastic only study).

One of the critical aspects in approximating the leakage involves estimating the initial surface separation in the compressive seal interface prior to loading. Presently, the ten-point maximum asperity peak is used in the annular contact zone, which in theory, should provide a satisfactory means for describing the maximum surface separation.

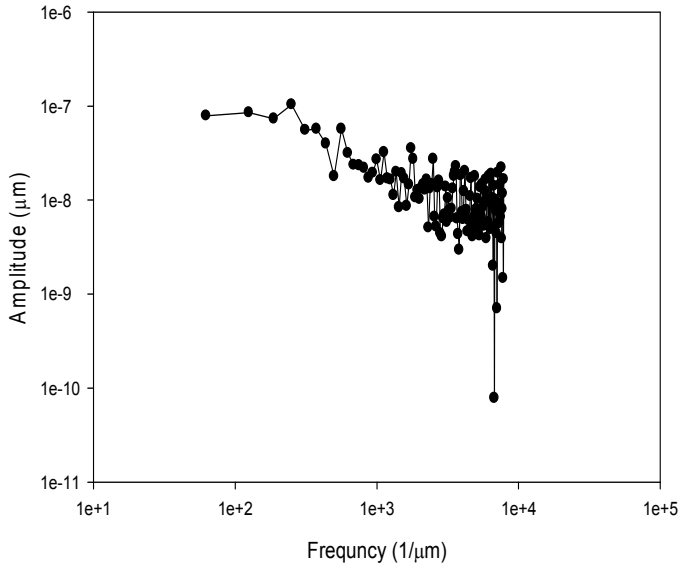

Figure 22: Log-log plot of the amplitude as a function of spatial frequency.

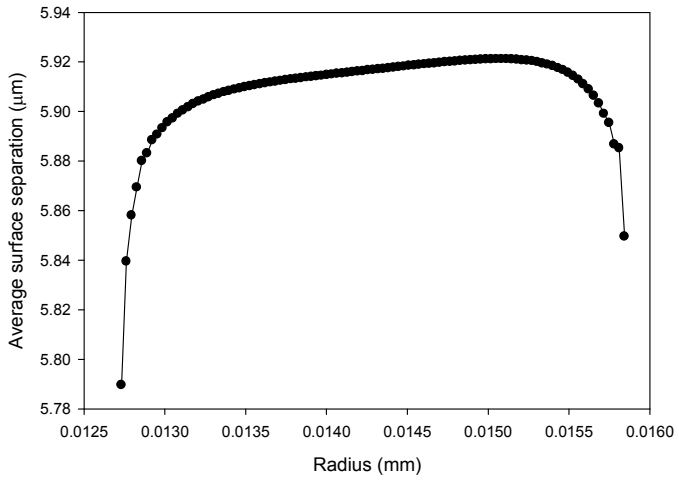

Figure 23: Average surface separation versus radius in 600 grit compressive seal assembly.

As shown in Figure 23, the resulting nodal surface separation is plotted as a function of radial distance from the origin. As indicated by the figure, the surface separation is the least at the nodal locations corresponding to the inner

and outer radius. The surface separation increases some but for the most part remains constant over the interior nodes. In fact, the variation across the entire annular region is less than 1 percent.

Using the mixed lubrication model, the volumetric flow rate per unit seal length is determined as specified per experimental conditions. The corresponding elastic model predictions were then compared with the average experimental leakage results as shown in Table 8, while the standard error or uncertainty associated with the experimental leakage results is included as Table 9. A complete listing of the leakage results of the current study is included in Appendix A as Table 24.

Table 8: Leakage results for metal-metal compressive seal with two surface finish variations.

Stress(MPa)	Temp (°C)	100 grit avg (sccm/cm)	100 grit elastic (sccm/cm)	600 grit avg (sccm/cm)	600 grit elastic (sccm/cm)
0.689	25	0.706	115.0526	0.367	0.2779
2.068	25	0.616	106.0371	0.363	0.2650
3.447	25	0.588	100.2749	0.289	0.2547
0.689	250	1.696	76.4481	0.248	0.1846
2.068	250	1.395	70.4576	0.220	0.1761
3.447	250	1.143	66.6289	0.204	0.1692
0.689	500	1.270	55.6877	0.199	0.1345
2.068	500	0.886	51.3240	0.203	0.1282
3.447	500	0.962	48.5350	0.210	0.1233

Table 9: Standard error associated with experimental average volumetric leakage per circumferential length results for metal-metal compressive seal assembly.

Stress(MPa)	Temp (°C)	100 grit σ_u (sccm/cm)	600 grit σ_u (sccm/cm)
0.689	25	0.016	0.014
2.068	25	0.009	0.022
3.447	25	0.035	0.048
0.689	250	0.245	0.045
2.068	250	0.459	0.044
3.447	250	0.179	0.037
0.689	500	0.184	0.039
2.068	500	0.107	0.046
3.447	500	0.036	0.042

As indicated by Table 8, the leakage rates for the 600 grit substrate seal assembly are considerably lower for the same loading and temperature conditions as compared to the 100 grit metal–metal seal assembly, which indicates the effect of surface roughness is prominent. Referring to Table 8, the ten–point maximum for the 100 grit substrate is more than 14 times its 600 grit counterpart, which indicates that the undeformed average surface separation of the 100 grit substrate is considerably larger than its 600 grit counterpart. Thus, the higher leakage rates for the same loading conditions are indicative of a substantial difference in the two substrates' average surface separation even after loading. It also follows that there is an inverse relationship between load and leakage rate; that is, leakage rate decreases with an increase in load. As temperature increases, the leakage rates decrease monotonically with respect to load in the 600 grit compressive seal, while leakage rates in the 100 grit increase from 25 to 250 °C and then decrease from 250 to 500 °C while holding the applied stress constant. Referring to Table 9, the standard error associated with the mean at elevated temperatures was much higher for 100 grit substrate as

compared to the 600 grit. Since the leakage apparatus used was the same, these results indicate that there may be some instability associated with using the slope of the differential pressure versus time to approximate $\frac{d\Delta p}{dt}$.

Referring back to Table 8, the computational leakage model yields qualitative trends consistent with the experimental observations discussed previously. Both the experimental and computational model results are consistent with regard to the role of surface roughness. Leakage rates decrease dramatically when comparing the 600 grit seal to the 100 grit seal. Thus, smoother interfaces exhibit less leakage for the same applied compressive load.

From a quantitative standpoint, the accuracy of the model predictions were mixed when analyzing the two machined surface finishes. For the 100 grit compressive seal assembly, the leakage predictions grossly over predicted the experimental leakage results. From Table 6, we observe that the maximum surface height is over 100 microns. Since this height corresponds to the initial gap, which, according to the micro contact model is not decremented more than 1 percent. Thus, the gap during the loading process according to the model remains virtually unchanged across the annular interface. From Equation (22), the computational model's leakage rate is proportional to h^3. As a result, the model predicts a significantly higher leakage compared to experimental results. One of the deficiencies in the modeling approach is that the undeformed surface separation could potentially become dominated by high outlier peaks. Further investigation should be performed to determine whether the peaks included are

indeed indicative of the overall surface, or are these peaks isolated, which would indicate that they would be plastically deformed to a greater extent than the overall surface to be consistent with the leakage rates exhibited in this study. In order for the experimental and model results to compare more favorably, the gap would need to be reduced, which indicates that plastic deformation should be assessed in order to obtain improved results for the rougher surface.

The computational model was reasonably effective in predicting the leakage rates in the 600 grit compressive seal assembly. According to Figure 24, the model under predicts the leakage as compared to the experimental results, but improves and lies within the standard error bars for the two higher temperatures. In Figure 25 and Figure 26, the applied compressive load is varied. The model predictions are close to experimental results at 500 °C, and were reasonably close at 25 °C in Figure 25 when compared with the experimental average volumetric leakage rate.

Overall, the computational model performs well predicting the leakage rates for the smoother surface, which may be partially explained by the fact that there are fewer isolated outlier peaks in the nominal contact zone for the 600 grit surface as compared to the 100 grit surface. The model seems to capture the effect surface roughness and temperature well. However, the current model seems too stiff in the present form to adequately capture the effect of loading. One explanation for the stiffness in the model can be attributed to the fact that the waviness of the Inconel annulus was not considered. In addition, an elastic-plastic contact model may be necessary to adequately capture the loss in

average surface separation at the local maxima. The relatively large standard error associated with the 100 grit substrate exclusively may be indicative of some instability associated the approximating $\frac{d\Delta p}{dt}$ as opposed to measurement uncertainty associated with a measurement device.

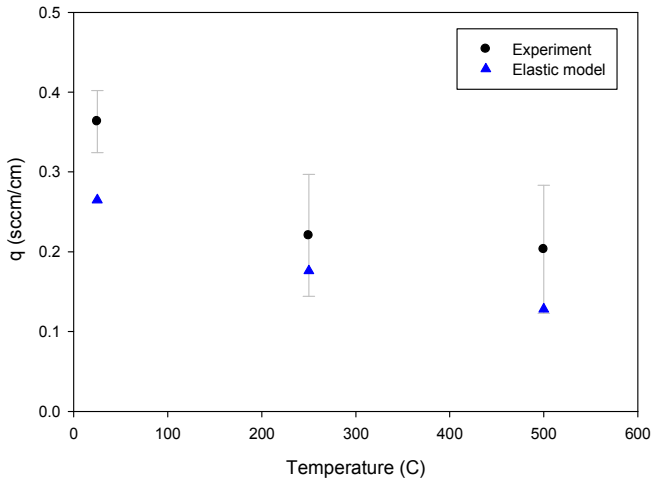

Figure 24: Comparison of volumetric leakage rate per seal length versus temperature for Inconel/SS 316 compressive seal at 2 kPa (0.29 psig) with p_{comp} = 2.068 MPa (300 psi).

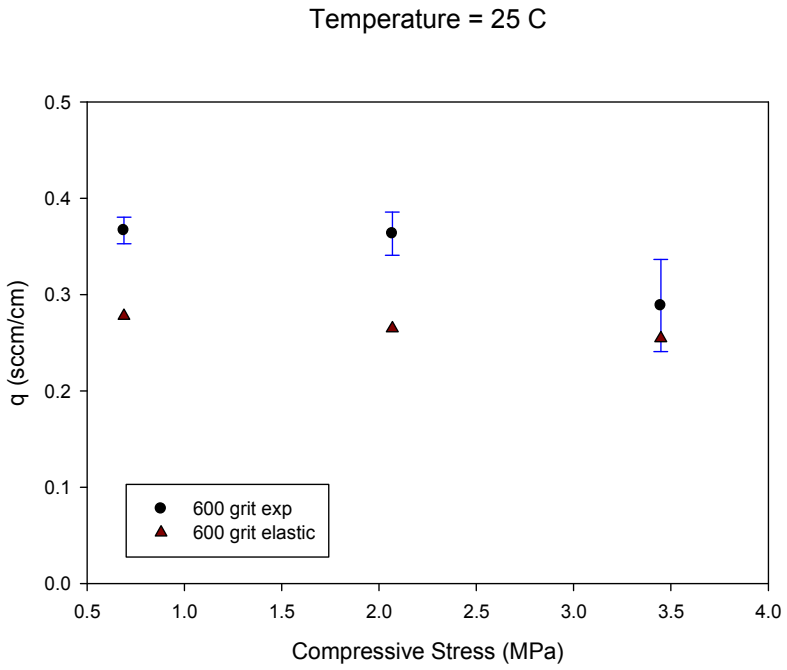

Figure 25: Comparison of volumetric leakage rate per seal length as a function of compressive stress for Inconel/SS 316 compressive seal at 2 kPa (0.29 psig) with T= 25 °C.

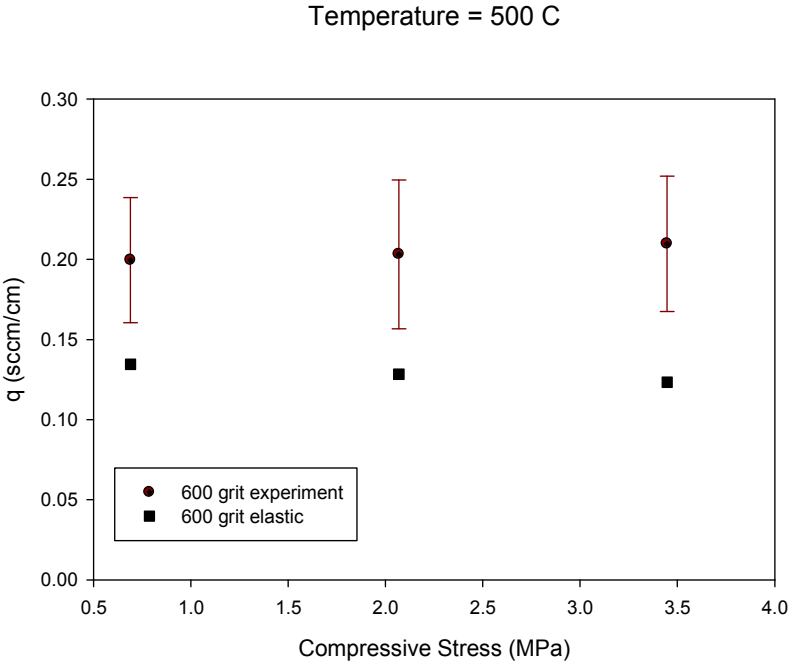

Figure 26: Comparison of volumetric leakage rate per seal length as a function of compressive stress for Inconel/SS 316 compressive seal at 2 kPa (0.29 psig) with T= 500 °C.

7.3. Elastic Only- Results Summary

An elastic computational leakage model was presented to describe how surface roughness, temperature and loading conditions affect the volumetric leakage rate in a metal-metal compressive seal. A macro-contact model was used to determine the contact pressure distribution on the surface of the stainless steel substrate. Next, the Jackson-Streator micro-contact model was used to determine the localized surface separation using the FFT of surface profile measurements. Once the mean spacing and pressure distribution was determined, a mixed lubrication model could then be used to approximate the volumetric leakage rate. The leakage model predictions were then compared to leakage experiment results. The following observations can be made:

1. Both experimental and model results indicate that the volumetric leakage initially decreases monotonically with increasing load, but becomes decreasingly sensitive to the load as the load is increased.

2. For the same average compressive stress, the volumetric leakage was considerably higher in the 100 grit test specimens as compared to the 600 grit metal-metal specimens, which underscores the significance of surface roughness.

3. Compared to the experimental results, the computational leakage model grossly over predicted the normalized leakage rates for the

100 grit compressive specimens. On the other hand, the normalized leakage predictions for the 600 grit metal-metal specimen compared well with its experimental counterpart. The discrepancy in the 100 grit substrate can partially be attributed to the fact that the undeformed gap is skewed by high outlier asperity peaks. It would be instructive to investigate how the surface characteristics change after mechanical loading. Subsequent analysis should also approximate the experimental gap to further assess the micro contact model's accuracy.

4. Due to the relative insensitivity to load, subsequent models should include elastic-plastic deformation to further improve results.

8. LEAKAGE RESULTS- ELASTIC-PLASTIC COMPARISON

8.1. Elastic-Plastic Overview

In this chapter, the elastic-plastic computational leakage model predictions are compared to the previously introduced elastic only model predictions as well as concurrent leakage tests. Separate experimental leakage studies were performed in addition to the leakage results presented in the previous chapter, and will be described subsequently. In addition, the same stainless steel substrates are using in the current analysis as before. However, the two substrate's surface characteristics have changed due to the aging effects associated with repeated exposure to heat and mechanical loading.

It is also important to note that although both the elastic and elastic-plastic models can be compared with any of the leakage studies presented here, the intent was to use the insight gained from the elastic-only leakage comparison to demonstrate how the modeling approach was refined, and in turn, the results improved. Thus, the nomenclature used for characterizing the series of experiments associated with the elastic only model comparison were called 'Elastic Only Comparison', while the subsequent independent leakage experiments associated with the Elastic-plastic model comparison is termed 'Elastic-plastic Comparison'. Therefore, the nomenclature is model-centric since the experimental leakage results are independent of the model selected for comparison.

In the current study, a metal-metal compressive seal configuration with a single interface is used throughout the leakage study. However, the working fluid used in this study was purified Argon rather than Helium. In addition to the leakage rate comparison mentioned above, an experimental effective gap is determined in the current study; that is, the average gap across the entire annular region is approximated through derivation from mixed lubrication theory. The aforementioned experimental effective gap is then compared with the two model predictions. This comparison allows us to assess how well the micro contact model approximates the average gap at the annular interface.

The corresponding elastic-plastic leakage comparison test matrix is identical to the elastic only study shown in Table 4. However, in the current study, each row or test combination was performed seven times in an effort to reduce the standard error associated with the average leakage for the specified conditions.

8.2. Elastic-Plastic Results

The same mechanical parameters that used throughout the current leakage analysis were used in the prior elastic only leakage study presented in Chapter 6. To review the aforementioned parameters please refer to Table 3, while a listing of the temperature dependent properties including the dynamic viscosity, μ, and yield strength are included as Table 10. The size of the annular region and the differential pressure, Δp, were influenced by the experimental

procedure outlined by Chou and Stevenson [12]. Since the metal-metal seal was comprised of an Inconel annulus and SS 316 machined substrate, the appropriate thermo-elastic properties including the elastic modulus, Poisson's ratio, and coefficient of thermal expansion were selected from material property handbooks [57]. The surface roughness characteristics for the two stainless steel samples are summarized in Table 11, while the consequent surface roughness scans for the 100 grit and 600 grit substrates used in this study appear as Figure 27 and Figure 28, respectively. According to Table 11, the root mean square roughness is actually lower for the 100 grit substrate compared the 600 grit specimen. As expected, the maximum peak height in the contact zone, h_{max}, is higher for the 100 grit specimen than its 600 grit counterpart. The surface scan results indicate that 100 grit specimen's core surface roughness statistics have reduced dramatically as compared to the elastic only leakage study presented in the previous chapter (Refer to Table 7). Referring to Table 7, there was an appreciable difference in all of the parameters when comparing the two substrates. After repeated mechanical loading and exposure to heat, the higher asperities were flattened considerably. Subsequent surface scans were conducted for the elastic-plastic model comparison, and these latter scans indicate that there is virtually no difference between the two substrates when comparing c_{max} the ten-point maximum, which is an important distinction since the initial gap is approximated using $c_{max.}$ Comparing the 100 grit surface roughness scan depicted in Figure 27 to the pristine scan of the previous study (Figure 20), it appears that the highest asperity peaks are now more isolated and

have been reduced in height as compared to the original scan. As result, the leakage statistics associated with the 100 grit surface should improve considerably for the same temperature and loading conditions since the overall substrate height profile appears to have been reduced.

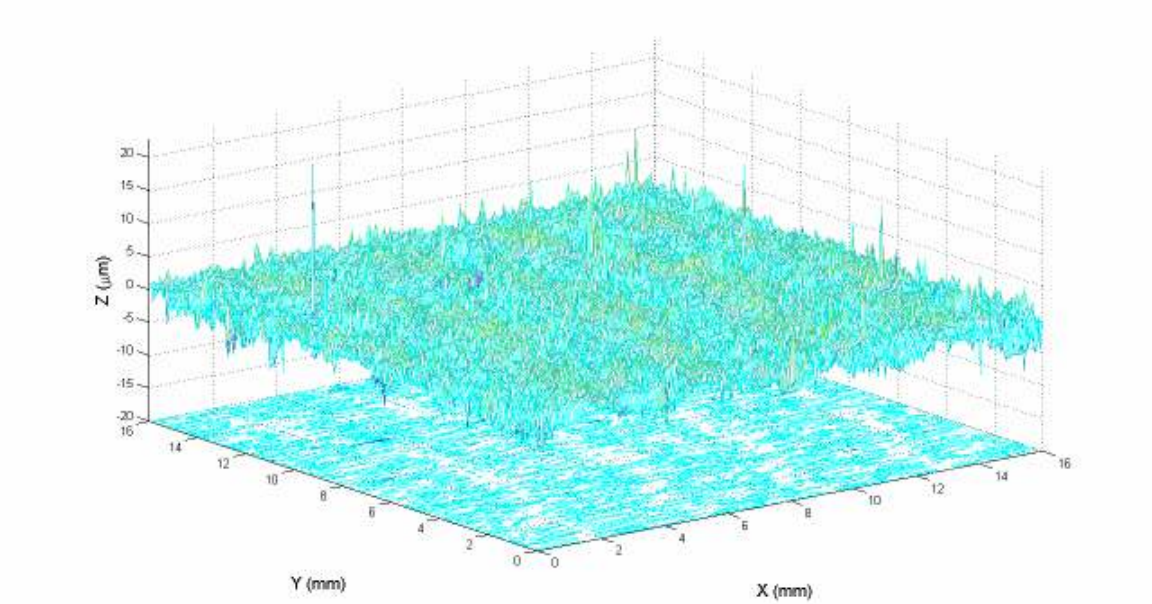

Figure 27: Surface roughness scan of lapped 100 grit stainless steel substrate prior to loading (elastic-plastic study).

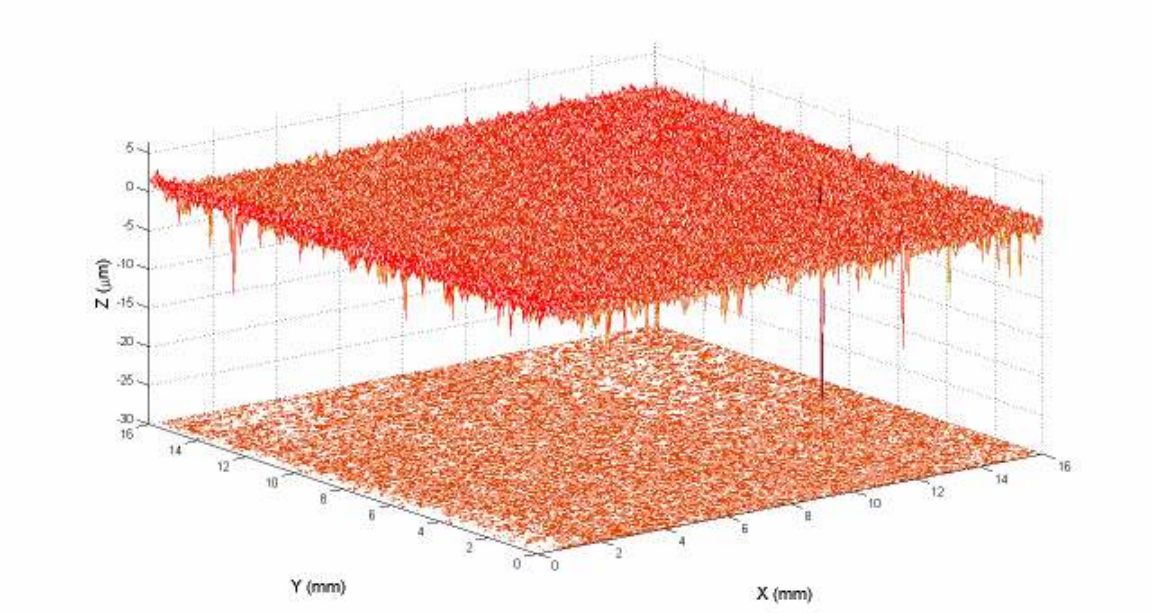

Figure 28: Surface roughness scan of lapped 600 grit stainless steel substrate prior to loading (elastic-plastic study).

Table 10: Temperature-dependent properties used in elastic-plastic leakage study.

T (°C)	μ (Pa*s)	Sy (MPa)	ρ(kg/m^3)
25	2.26E-05	207	1.634E-03
250	3.58E-05	190	9.312E-04
500	5.06E-05	180	6.300E-04

Table 11: Summary of the surface roughness statistics that were determined in an effort to predict the average elastic-plastic gap.

Substrate	S_q (m*10^{-6})	c_{max} (m*10^{-6})	h_{max} (m*10^{-6})
100 grit	1.504	10.881	12.465
600 grit	1.912	10.633	7.353

Using the mixed lubrication model, the volumetric flow rate is determined as specified per the experimental conditions. The volumetric leakage results per circumferential length from both the elastic and elastic-plastic computational leakage models are then compared with the experimental results. The volumetric leakage rate per circumferential seal length at the outer radius, q , is plotted versus average compressive stress at 25 °C for the 100 and 600 grit compressive seals assemblies in Figure 29 and Figure 30, respectively. Similarly, the relationship of the previously mentioned quantities was also investigated at 500°C, and the corresponding plots for the 100 and 600 grit assemblies are included as Figure 31 and Figure 32.

Referring to Figure 29, both the elastic and elastic-plastic model over predict the leakage as compared to the experimental average of the seven leakage runs, while the two models under predict leakage in the 600 grit compressive assembly as seen in Figure 30. In the 100 grit case, the both models predict the asperities to behave stiffer than experimental results indicate with the elastic-plastic model out performing its elastic counterpart. In the 600 grit case, the elastic model captures the experimental results at the two higher loads. At 25 °C, the elastic model's predictions are almost within the standard error bands for the two higher contact pressures as depicted in Figure 30, and in general, outperform the elastic-plastic model for the aforementioned conditions.

According to Figure 31 and Figure 32,when temperature increases to 500 °C both models under predict leakage in the 100 grit case and slightly over predict leakage in the 600 grit case. In the 100 grit case, the results seem to

suggest that the interfacial modulus is too stiff. Unlike the results at 25 °C, the elastic–plastic model now consistently out performs the elastic only model at the elevated temperature. The elastic-plastic model seems to perform particularly well at 500 °C in predicting leakage rates as compared to experimental results.

The performance of the models is consistent with intuition. One would expect the rougher substrate (e.g.100 grit substrate) to experience more plastic deformation than the smoother substrate due to higher asperity peaks. Both models seem to be in agreement with regard to the effect of load on leakage rates in either compressive seal assembly; that is, as load increases, the volumetric leakage rate decreases. When heat is added at elevated temperatures, the yield strength goes down resulting in increased interfacial deformation for the same loading conditions. Such phenomena should be more accurately captured using the elastic-plastic model.

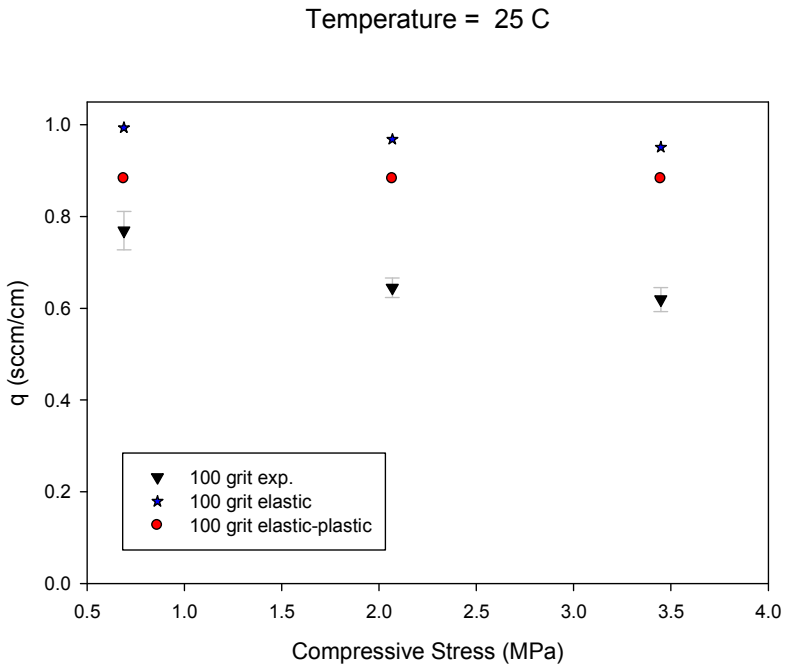

Figure 29: Comparison of volumetric leakage rate per seal length as a function of compressive stress for Inconel/ 100 grit SS 316 compressive seal at 2 kPa (0.29 psig) with Temperature = 25 °C.

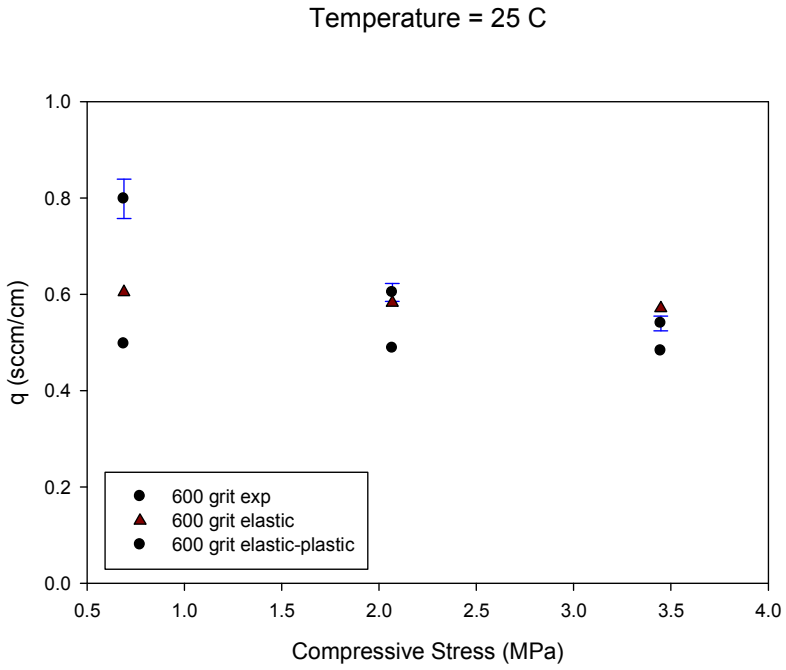

Figure 30: Comparison of volumetric leakage rate per seal length as a function of compressive stress for Inconel/ 600 grit SS 316 compressive seal at 2 kPa (0.29 psig) with Temperature = 25 °C.

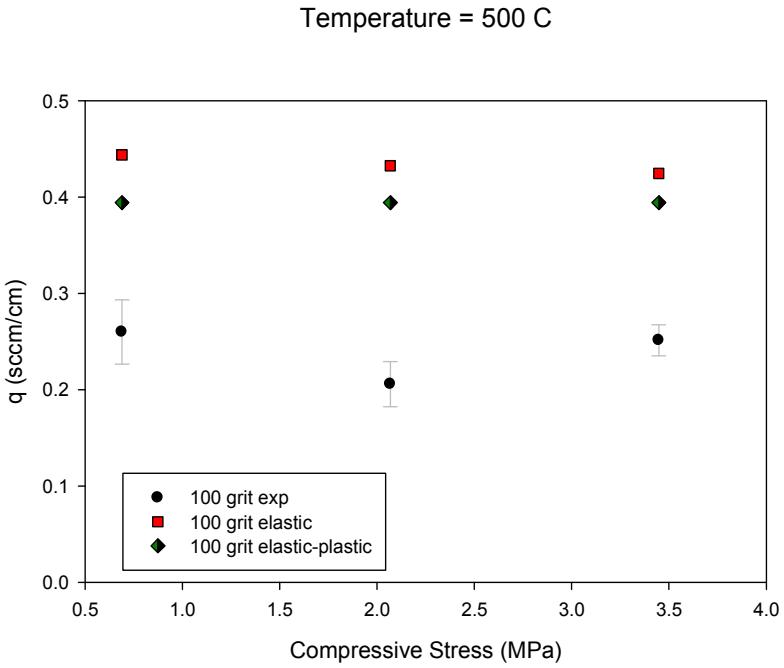

Figure 31: Comparison of volumetric leakage rate per seal length as a function of compressive stress for Inconel/ 100 grit SS 316 compressive seal at 2 kPa (0.29 psig) with Temperature = 500 °C.

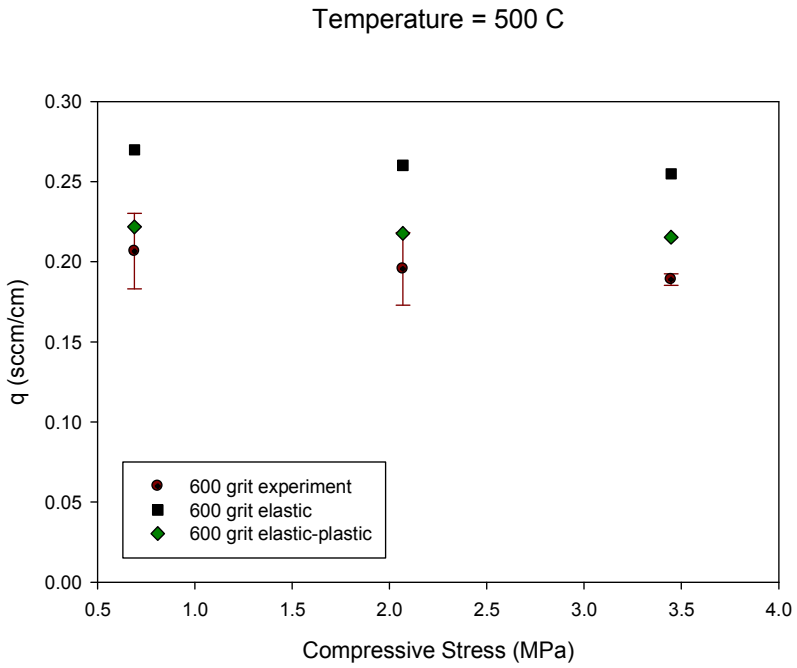

Figure 32: Comparison of volumetric leakage rate per seal length as a function of compressive stress for Inconel/ 600 grit SS 316 compressive seal at 2 kPa (0.29 psig) with Temperature = 500 °C

Referring back to Figure 29 and Figure 30, it follows that there is no discernable difference between the 600 grit substrate seal assembly's leakage rates for the same loading and temperature conditions as compared to the 100 grit seal assembly, which indicates the effect of surface roughness is not as prominent as was witnessed in the 'Elastic Only' leakage study. This result may be partially explained by the fact that both substrates' asperities undergo plastic deformation, especially the 100 grit substrate as result of repeated mechanical loading and exposure to heat. Moreover, even though the 600 grit surface is still smoother than the 100 grit surface as determined from the surface scan, the level of plastic deformation present in the sealing zone of the 100 grit substrate is

now suffice to mitigate the effect of surface roughness.. According to Figure 31, the experimental leakage rates in the 100 grit decrease from 0.689 MPa to 2.068 MPa and then increase from 2.068 MPa to 3.447 MPa while holding temperature constant at 500 °C, which contrasts the predictions of decreasingly monotonic behavior as predicted by both leakage models. On the other hand, the leakage rate decreases monotonically with respect to load in the 600 grit compressive seal for both model and leakage results at 500 °C. As temperature increases, the dynamic viscosity of the fluid increases, while the fluid's density increases, both of which contribute to the volumetric leakage rate decreasing as indicated by Equation (22).

The relationship between the effective gap and compressive stress is investigated in Figure 33 through Figure 36. At 25 °C, both models over predict the gap as compared to the experimental results with the elastic–plastic model outperforming the elastic only model as shown in Figure 33 and Figure 34. Referring to Figure 35 and Figure 36, both models seem to approximate the effective gap well as compared to experimental results at 500 °C.

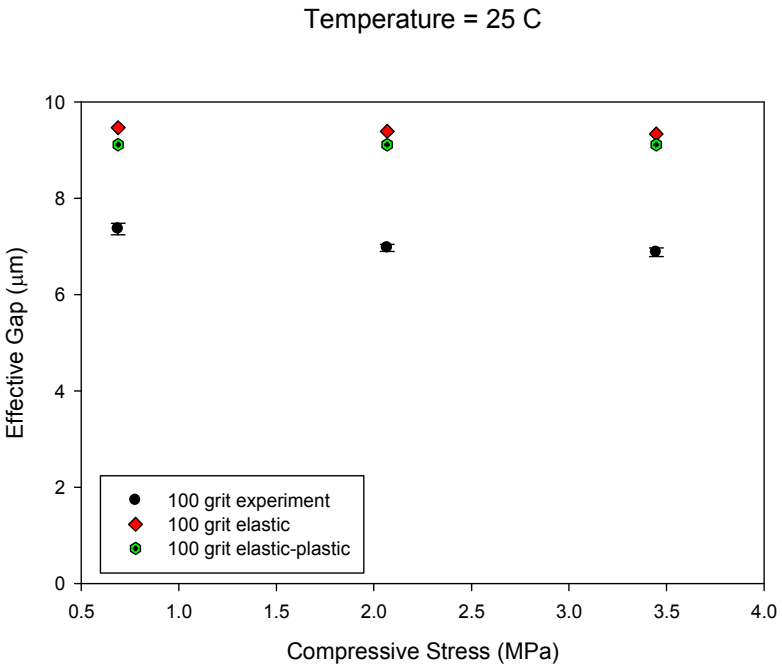

Figure 33: Comparison of effective gap as a function of compressive stress for Inconel/ 100 grit SS 316 compressive seal at 2 kPa (0.29 psig) with Temperature = 25 °C.

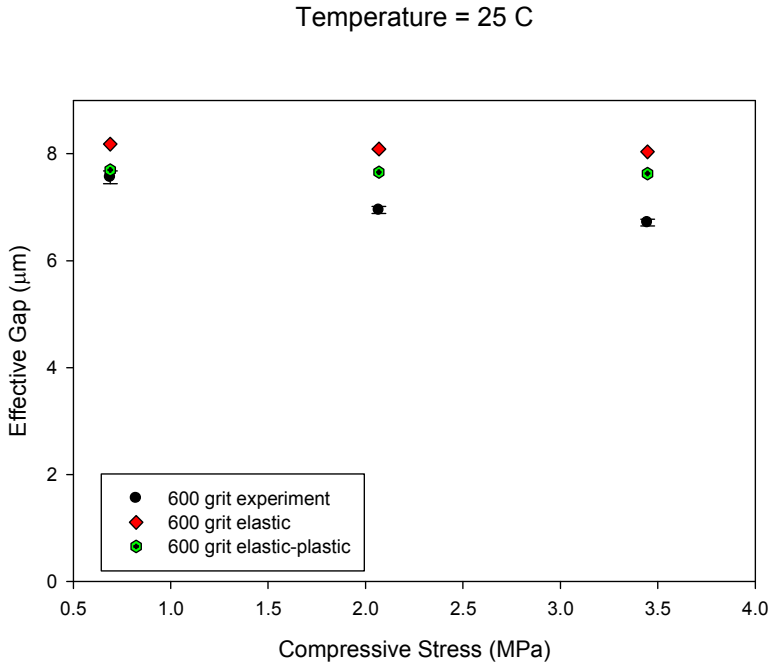

Figure 34: Comparison of effective gap as a function of compressive stress for Inconel/ 600 grit SS 316 compressive seal at 2 kPa (0.29 psig) with Temperature = 25 °C.

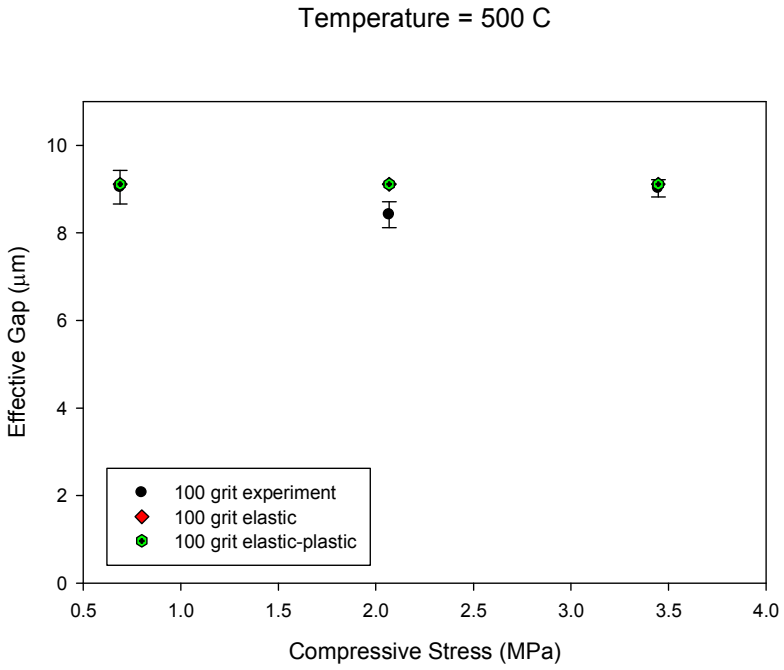

Figure 35: Comparison of effective gap as a function of compressive stress for Inconel/ 100 grit SS 316 compressive seal at 2 kPa (0.29 psig) with Temperature = 500 °C.

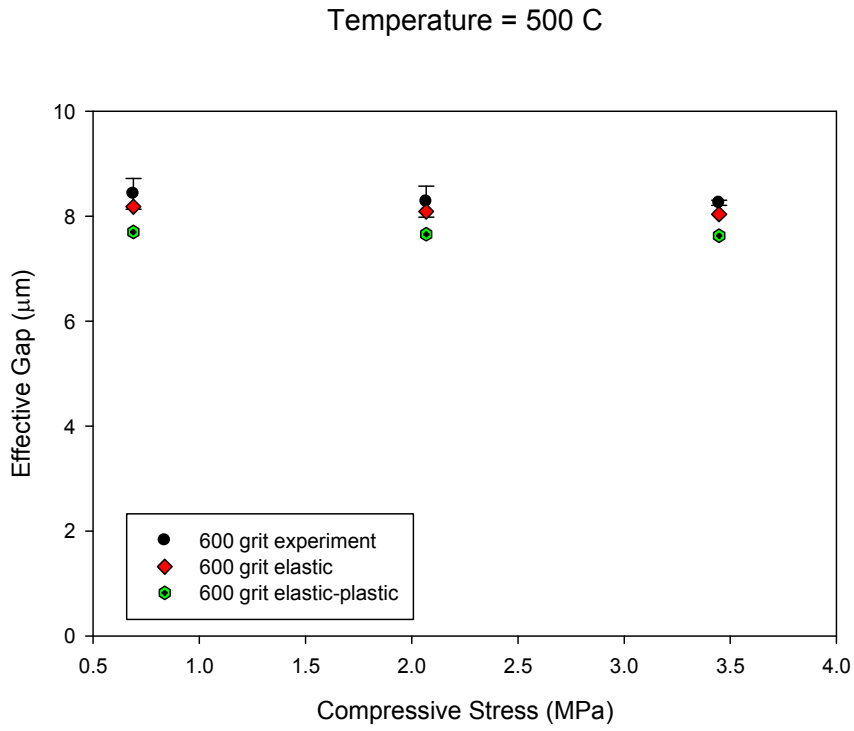

Figure 36: Comparison of effective gap as a function of compressive stress for Inconel/ 600 grit SS 316 compressive seal at 2 kPa (0.29 psig) with Temperature = 500 °C.

Both computational leakage models yield qualitative trends consistent with the experimental results. Regarding the role of surface roughness, leakage rates decrease dramatically when comparing the 600 grit seal to the 100 grit seal, although experimental results indicate that the effect of surface roughness is stymied when ample plastic deformation is present. Thus, smoother interfaces exhibit less leakage for the same applied compressive load only when considerable plastic deformation in the sealing zone is absent.

The elastic and elastic–plastic computational models were both reasonably effective in predicting the relationship between leakage and

temperature for each of the compressive seal assemblies. From a qualitative standpoint, as temperature increases, the volumetric leakage rate per seal length decreases. According to Figure 37 and Figure 38, both computational models slightly over estimate leakage in the rougher 100 grit compressive seal assembly. On the other hand, both models' predictions are very close to the experimental results for the 600 grit compressive seal assembly.

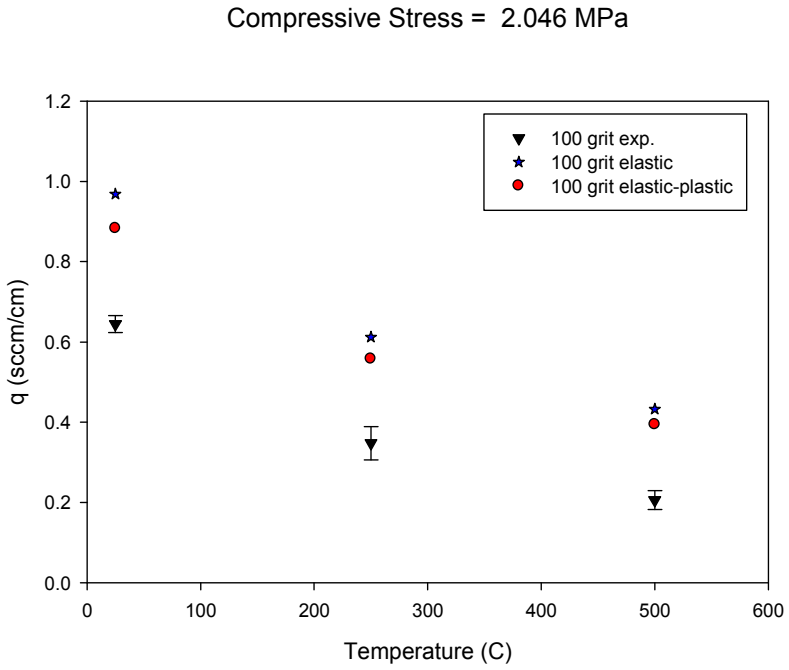

Figure 37: Comparison of volumetric leakage rate per seal length as a function of temperature for Inconel/ 100 grit SS 316 compressive seal at 2 kPa (0.29 psig) with Compressive stress = 2.046 MPa.

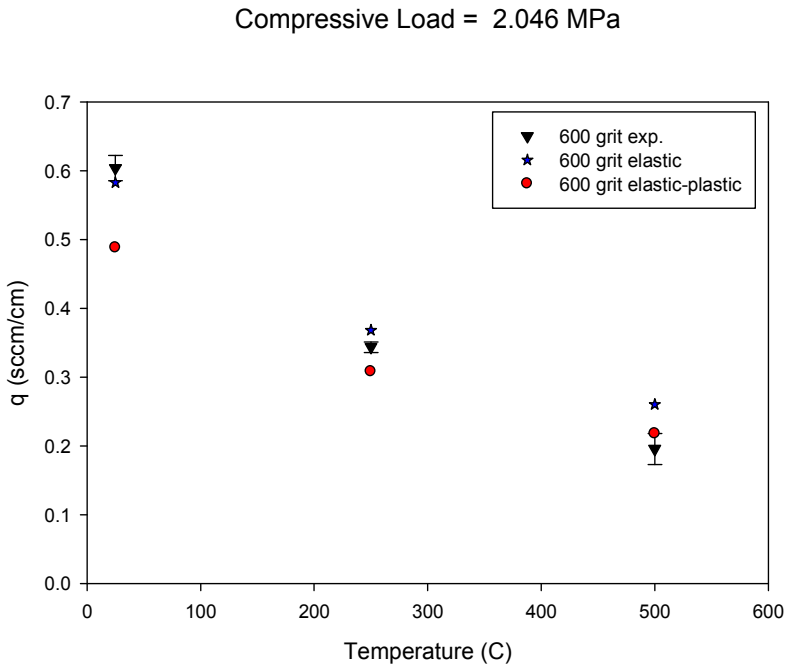

Figure 38: Comparison of volumetric leakage rate per seal length as a function of temperature for Inconel/ 600 grit SS 316 compressive seal at 2 kPa (0.29 psig) with Compressive stress = 2.046 MPa.

Overall, the elastic computational model seems to be more in tune with experimental results at lower temperatures, while the elastic-plastic model seems to capture the leakage more effectively at higher temperatures. Both models provide reasonably good predictions for the effective gap and volumetric leakage rate in the 600 grit compressive seal assembly. In general, the model results for the 100 grit seal assembly were conservative as compared to its experimental findings. A complete listing of the individual leakage results for the current study is included as Table 25 Appendix A, while the corresponding average gap results are included in Table 26 of Appendix A. A summary of the leakage results and corresponding experimental standard error are included in the same Appendix as

Table 27 through Table 29. The analogous results summary for the effective gap is included as Table 30 through Table 32 of Appendix A.

8.3. Elastic-Plastic - Results Summary

A computational leakage model was presented to describe how surface roughness, temperature and loading conditions affect the volumetric leakage rate and effective surface separation in a metal-metal compressive seal. A finite element-based macro-contact model was used to determine the contact pressure distribution on the surface of the stainless steel substrate. Next, the Jackson-Streator (JS) micro-contact model was used to determine the localized surface separation using the FFT of surface profile measurements. Both elastic and elastic-plastic deformations were considered in the current study. Once the mean spacing and pressure distribution was determined, a mixed lubrication model could then be used to approximate the volumetric leakage rate. The leakage model predictions were then compared to leakage experiment results. The following observations can be made:

1. Both experimental and model results indicate that the volumetric leakage initially decreases monotonically with increasing load, but becomes decreasingly sensitive to the load as the load is increased.

2. Both experimental and model results suggest that the volumetric leakage rate decreases monotonically as temperature increases. With regard to the effect of the temperature, the elastic-plastic

leakage model out performed its elastic only counterpart. The elastic-only leakage computational model slightly over predicts leakage as compared to its experimental counterpart, while the elastic-plastic model leakage predictions were very close to the corresponding experimental results.

3. As far as the effective gap is concerned, both leakage models over estimated the effective gap at 25 °C. On the other hand, at 500 °C both computational models estimated the effective gap to be lower than its experimental counterpart.

4. Results were mixed regarding the role of surface roughness. According to the leakage models, the smoother 600 grit compressive specimens exhibited less leakage than their 100 grit counterparts for the same temperature and loading conditions. However, experimental results indicated that there was virtually no difference in the two substrates leakages, which indicates plastic deformation can overcome a perceived advantage in leakage performance due to surface roughness.

5. Both models and experiment were consistent in indicating the volumetric leakage rate per seal length decreases monotonically with respect to temperature. Both computational models predicted leakage particularly well as compared to experiment in the smoother 600 grit compressive seal assembly.

9. ALTERNATE EXPERIMENTAL LEAKAGE DETERMINATION

9.1. Alternate Leakage Determination Overview

In this chapter, we investigate whether the experimental volumetric leakage rate results are most accurately presented by using the instantaneous slope by way of a divided difference approach to approximate $\frac{dp}{dt}$ in lieu of a regression analysis approach which will be described subsequently. After observing relatively large uncertainty in the leakage results for the 100-grit substrate at elevated temperatures especially, it seemed that fluctuations observed in these results were not characteristic of the measurement uncertainty associated with the pressure transducer and thermocouples used to assess pressure and temperature, respectively. Taking a closer look at Table 9, the standard error associated with the volumetric leakage rate average was consistently higher for the 100 grit compressive seal as compared to the 600 grit compressive seal results even though the same equipment and loading conditions were employed. In addition, a similar trend continued in the Elastic-Plastic Study (see Table 29) even though four additional replicates were performed as compared to the Elastic only study. Since a drawback of using an instantaneous slope calculation is that signal noise can be amplified, an investigation was performed to whether it would be more appropriate to use regression analysis to determine the best-fit over a specified pressure interval,

and then use the first derivative of the resulting p(t) function to determine $\frac{dp}{dt}$ at a differential pressure of 2 kPa.

To accomplish this end, the elastic-only JS micro-contact models is used to determine the function that governs how the differential pressure decays as a function of time in the 600 grit metal-metal compressive seal assembly. Unlike previously presented results that employ a finite difference approach to predict the volumetric leakage rate per circumferential seal length at a specific instant, this investigation seeks to not only assess how well these micro contact models can capture the change differential pressure over a relatively large span of time, but also to discern if a regression-based approach to approximating the experimental leakage rates provides a more precise measurement as compared to the previously presented divided difference approach.

The experimental data associated with the 600 grit substrate in the elastic only comparison study, which was presented in Chapter 7 is compared to the model elastic only and elastic-plastic model predictions. Regression analysis is used to characterize the relationship of the pressure versus time for the various compressive loading conditions as shown in Table 12 with each row observed a total of three times.

Table 12: Summary of experimental conditions used for the differential pressure characterization study.

Substrate	Stress(MPa)	Temp(°C)
600 grit	0.689	25
	2.068	25
	3.447	25
	0.689	250
	2.068	250
	3.447	250
	0.689	500
	2.068	500
	3.447	500

9.2. Derivation of Alternate Leakage Approximation

In this section, mixed lubrication theory is leveraged to establish a governing equation or the differential pressure versus time. Through the entire study, the test gas has been treated as an ideal gas. By solving the ideal gas equation for mass and then differentiating with respect to time, it follows that the mass flow rate, $\dot{m}$, is given by

$$\dot{m} = \frac{V}{RT}\left(\frac{d\Delta p}{dt}\right) \tag{38}$$

An alternate expression for the mass flow rate was derived previously based on mixed lubrication theory, and it appears as Equation(21). By equating the two expressions for mass flow rate to one another and then solving for $\frac{d\Delta p}{dt}$, the change in differential pressure with respect to time may be written as

$$\frac{d\Delta p}{dt} = \frac{-\pi T_{kv} {p_o}^2 \left(1 - \left(\frac{p_i}{p_o}\right)^2\right)}{12\mu T_f V \int_{r_i}^{r_o} \frac{dr'}{\phi(r') r' h^3(r')}} \tag{39}$$

Where T_{kv} is the absolute fluid temperature inside the cylindrical known volume and T_f is the absolute fluid temperature in the furnace. By noting that the pressure at the inner radius is defined as $p_i = p_o + \Delta p$, the above expression can be written in terms of the differential pressure and atmospheric pressure. Thus, after substituting for p_i and multiplying out the numerator, $\frac{d\Delta p}{dt}$ can be written as

$$\frac{d\Delta p}{dt} = \frac{-\pi T_{kv} {p_o}^2 \left(\left(\frac{\Delta p}{p_o}\right)^2 - 2\left(\frac{\Delta p}{p_o}\right)\right)}{12\mu T_f V \int_{r_i}^{r_o} \frac{dr'}{\phi(r') r' h^3(r')}} \tag{40}$$

Since $\left(\frac{\Delta p}{p_o}\right) \ll 1$, Equation (40) can be linearized such that the following expression can be written to describe $\frac{d\Delta p}{dt}$:

$$\frac{d\Delta p}{dt} = \frac{-\pi \Delta p T_{kv} p_o}{6\mu T_f V \int_{r_i}^{r_o} \frac{dr'}{\phi(r') r' h^3(r')}}. \tag{41}$$

Separating the variables and applying the initial conditions it follows that the differential pressure as a function of time is given by

$$\Delta p = \Delta p_i e^{-\lambda t}$$
$$\lambda = \frac{-\pi p_O T_{kv}}{6\mu T_f V \int_{r_i}^{r_O} \frac{dr'}{\phi(r') r' h^3(r')}} \tag{42}$$

To determine $\frac{d\Delta p}{dt}$ and ultimately the experimental volumetric leakage rate, Equation (42) is differentiated with respect to time and can then be inserted into Equation (31) to determine the volumetric leakage rate as a function of time.

9.3. Pressure Characterization Results

As indicated by Table 12, each row of the 600 grit leakage experiments was conducted three times. From the case when the compressive stress is 500 psi and the temperature is 500 °C, the following three representative plots of the differential pressure versus time are included as Figure 39 through Figure 41. Regression analysis was then performed on each of the experimental runs to determine the function that best characterizes the differential pressure drop versus time. Over a differential pressure range of 3.0 to 1.7 kPa, it can be shown from the aforementioned plots that a decaying exponential adequately captures the relationship between the differential pressure drop and time elapsed, and has the general form: $\Delta p = a_0 e^{-a_1 t}$.

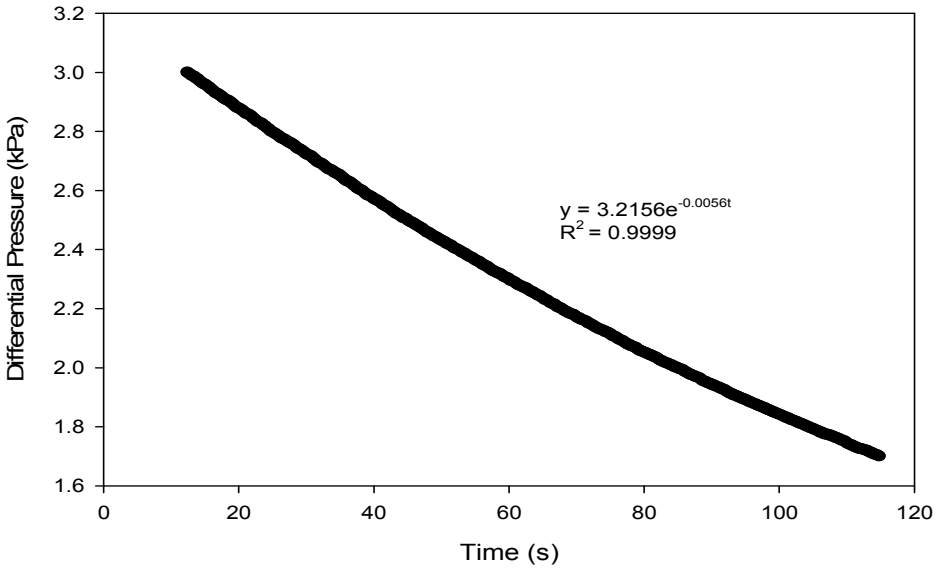

Figure 39 : Representative plot of the first trial of the differential pressure vs. time with T=500 °C and σ_{avg} =3.447 MPa.

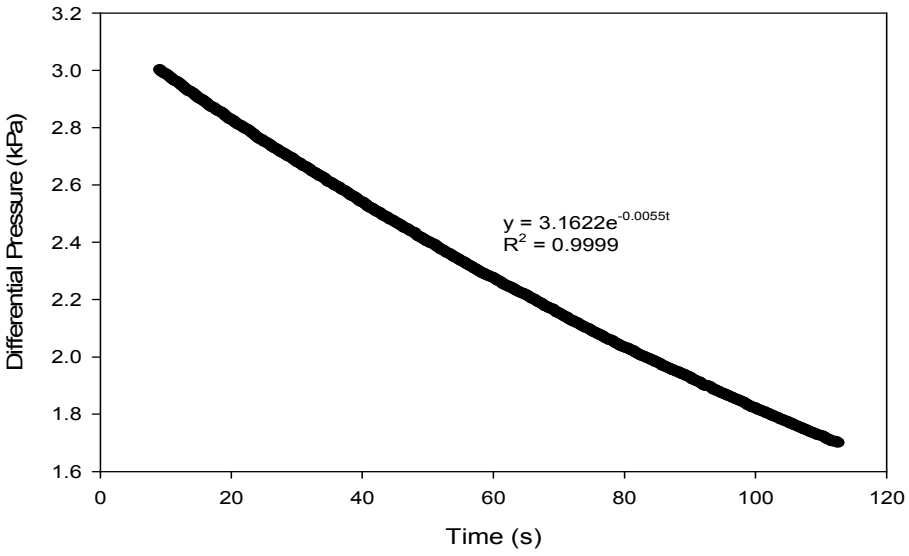

Figure 40: Representative plot of the second trial of the differential pressure vs. time with T=500 °C and σ_{avg} =3.447 MPa.

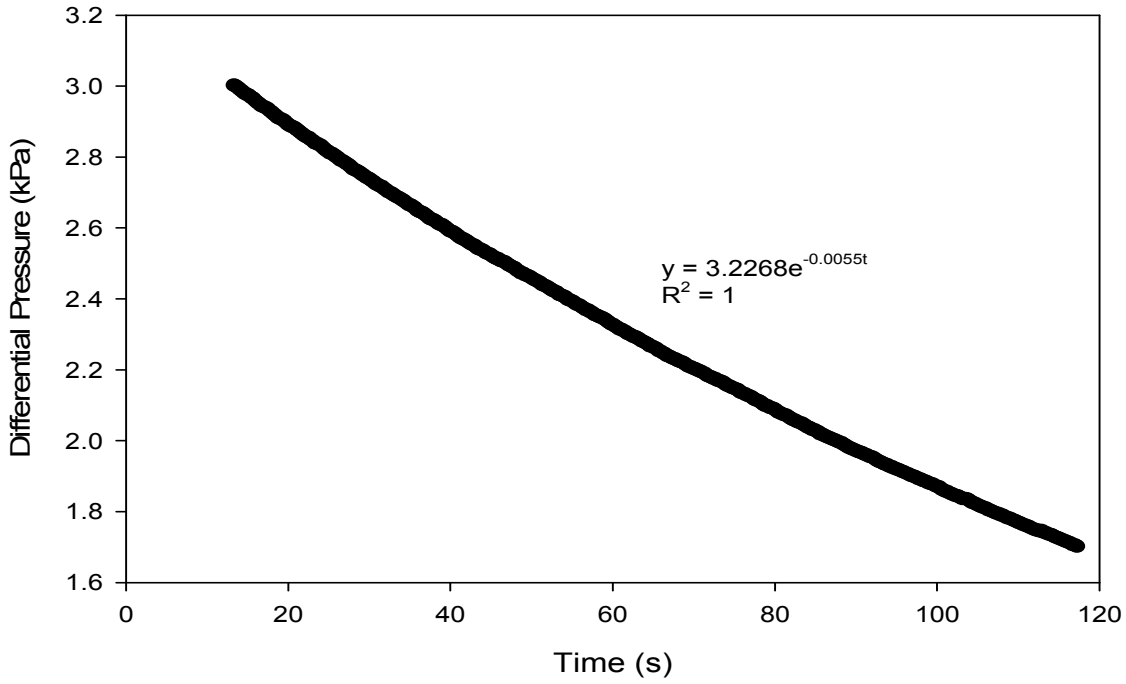

Figure 41: Representative plot of the third trial of the differential pressure vs. time with T=500 °C and σ_{avg} =3.447 MPa.

The above process was repeated for each of the experimental runs, and then the average and standard deviation associated with each of the exponential best fit constants were determined. The time scale was shifted so that the differential pressure at time equal to 0 seconds was 3.0 kPa. Using the expression derived in the previous section, the corresponding model predictions for the exponential function were also determined. A summary of the experimental results are included as Table 13, while the model predictions are included as

Table 14. Per the aforementioned tables, the elastic only model seems to better characterize the evolution of the differential pressure over time as

compared to its elastic plastic counterpart. In the 0.689 MPa (100 psi) and 500 °C case, after 1 minute has elapsed, the elastic only model over predicts its experimental average counterpart by about 30 percent. In general, the time experimental time constant is approximately 20% higher than its elastic only counterpart. Thus, the experimental results indicate the differential pressure decays considerably faster than the elastic only model predicts.

The regression and instantaneous slope methods were both compared based on their relative statistical uncertainty to determine which method provides the most precise results for the experimental results. To this end, the ratio of the standard error to the experimental average was obtained, and the consequent results are included in Table 15. As indicated from the table, the maximum relative error on a percentage basis of the mean is 6.90 % for the regression approach, while the instantaneous slope's maximum uncertainty is nearly 57 %. As the temperature increases beyond 25 °C, the instantaneous slope's percentage uncertainty exceeds 20 % for all but once case, while the regression method never exceeds 6.90%. Thus, it follows that the regression method is the preferred option for experimental results determination.

Table 13: Summary of experimental regression analysis to characterize differential pressure for 600 grit metal-metal compressive seal.

600 grit Experimental Equation : $y= a_0e^{-a1t}$					
Stress(MPa)	Temp(°C)	a_1-avg	a_1-std	a_0-avg	a_0-std
0.689	25	-0.0107	0.0001	1.1891	0.0090
2.068	25	-0.0095	0.0003	1.1833	0.0071
3.447	25	-0.0089	0.0001	1.1914	0.0128
0.689	250	-0.0063	0.0002	1.1702	0.0392
2.068	250	-0.0058	0.0002	1.1704	0.0059
3.447	250	-0.0057	0.0000	1.1810	0.0162
0.689	500	-0.0070	0.0005	1.2398	0.0461
2.068	500	-0.0060	0.0000	1.1742	0.0204
3.447	500	-0.0055	0.0001	1.1636	0.0108

Table 14: Summary of model predictions for 600 grit compressive seal differential pressure characterization.

600 grit Experimental Equation : $y= a_0e^{-a1t}$					
Stress(MPa)	Temp(°C)	a_1-avg	a_1-std	a_0-avg	a_0-std
0.689	25	-0.0107	0.0001	1.1891	0.0090
2.068	25	-0.0095	0.0003	1.1833	0.0071
3.447	25	-0.0089	0.0001	1.1914	0.0128
0.689	250	-0.0063	0.0002	1.1702	0.0392
2.068	250	-0.0058	0.0002	1.1704	0.0059
3.447	250	-0.0057	0.0000	1.1810	0.0162
0.689	500	-0.0070	0.0005	1.2398	0.0461
2.068	500	-0.0060	0.0000	1.1742	0.0204
3.447	500	-0.0055	0.0001	1.1636	0.0108

Table 15: Comparison of the statistical uncertainty associated with two approaches to approximating leakage rates.

Experimental Conditions		Regression		Slope	
Stress(MPa)	Temp (C)	100 grit % (std/avg)	600 grit % (std/avg)	100 grit % (std/avg)	600 grit % (std/avg)
0.689	25	1.08	0.76	3.97	6.56
2.068	25	2.96	0.60	2.54	10.71
3.447	25	0.94	1.07	10.24	28.68
0.689	250	2.76	3.35	24.99	31.18
2.068	250	2.76	0.51	56.96	34.62
3.447	250	0.66	1.37	27.20	31.25
0.689	500	6.70	3.71	25.08	33.91
2.068	500	0.59	1.74	20.86	39.53
3.447	500	1.11	0.93	6.47	34.86

9.4. Pressure Characterization Summary

The differential pressure versus time was plotted to ascertain the function that governs the decay of pressure in a 600 grit metal –metal compressive seal. The following observations can be made:

1. Both experimental and model predictions indicate that the differential pressure as a function of time is governed by an exponentially decaying function.
2. The standard deviation associated with the differential pressure was less than the instantaneous standard deviations associated with the volumetric leakage rate.
3. Both elastic only and elastic-plastic micro contact models under predict the exponential leakage constant; thus, the decay is slower than its experimental counterpart.

4. The elastic only micro contact model outperformed the elastic plastic model for capturing the relationship between differential pressure and time. This can be attributed to minimal accumulated plastic deformation since leakage test were performed when the 600 grit substrate was pristine.

10. SURFACE CHARACTERIZATION STUDY

10.1. Study overview

From the previously introduced elastic and elastic-plastic leakage series results, it was observed that the 100 grit substrate's maximum surface height and ten-point maximum was substantially lower after continued exposure to mechanical loading and heat during repeated leakage experiments. The leakage experiments conducted as a part of the 'Elastic Only' study were conducted approximately two months prior to the leakage experiments performed as a part of the 'Elastic-plastic' leakage study. Since both of the stainless steel substrates were only lapped once prior to the 'Elastic only' leakage study, and were allowed to age via experimental conditions, the substantial change in the 100 grit substrate's surface characteristics prompted further investigation regarding the effect of temperature and loading on the surface roughness scans. When the leakage studies were performed at elevated temperatures, the influence of temperature and loading was coupled. As a result, the chief aim of the present study was to ascertain if there is an appreciable change in the surface roughness parameters due to loading or temperature exclusively.

In addition to the recorded scans associated with the previously presented leakage studies, a series of surface roughness scans were conducted varying the load and temperature conditions separately in an attempt to determine how these parameters impact the surface characteristics of the stainless steel

substrates. A summary of the study conditions is included as Table 16. According to the table, the compressive stress was varied from 0.689 MPa (100 psi) to 3.447 MPa (500 psi), while temperature was varied from 25 to 500 °C. The test conditions were performed in a sequential manner as shown in Table 16.

Table 16: Summary of average compressive load and thermal exposure conditions used in surface characterization study.

Run	Scan	Load (MPa)	Temperature (°C)
1	100 grit	0	25
2		0.689	25
3		2.068	25
4		3.447	25
5		0	250
6		0	500
1	600 grit	0	25
2		0.689	25
3		2.068	25
4		3.447	25
5		0	250
6		0	500

10.2. Experimental Specifications

The two stainless steel substrates undergo mechanical loading or are heated to a specified temperature per Table 16. There were two separate experimental procedures performed depending on whether either heating or compressive loading was required. In the case of mechanical loading, the Inconel test piece was used to load the stainless steel substrate for twenty minutes at the desired compressive load with no gas flowing through the leakage apparatus. The same LabView program that was used in the aforementioned leakage experiments was also used in the present study to record the static load and time elapsed. When heating was required, a programmable furnace was

used to heat the substrate and keep it at the desired temperature for 30 minutes. The substrate was then allowed to cool naturally. After the mechanical or thermal loading was applied, the surface roughness scans were performed using the procedure outline in the chapter discussing leakage apparatus.

10.3. Surface Characterization Results

Surface roughness scans were performed on two stainless steel substrates per the conditions specified in Table 16. Room temperature and zero average compressive stress were selected as the reference conditions for the current study. The corresponding reference scans for the 100 grit and 600 grit stainless steel substrates are included as Figure 59 and Figure 60 in Appendix B, while the balance of the surface scans are included as Figure 61 through Figure 70 for the two substrates.

A summary of the surface roughness statistics for the entire surface characterization study is included as Table 17. The effect that average compressive load and temperature has on the ten point maximum is plotted in Figure 42 and Figure 43, respectively. According to Figure 42, once the substrate is loaded, the ten-point maximum decreases monotonically with respect to increasing compressive stress for the 100 grit substrate, while the 600 grit substrate decreases from 0.689 MPa to 2.068 MPa compressive stress, and then increases from 2.068 MPa to 3.448 MPa. As far as temperature is concerned, the 600 grit substrate's ten point maximum decreases with an

increase in load, while the 100 grit alternates with an increase in height and then a decrease in height as temperature is incrementally increased.

The role of temperature and mechanical loading was also investigated with regard to the maximum asperity height and the root mean square roughness for each substrate. The resulting plots for the two substrates are included as Figure 44 through Figure 47. Based on the Figure 44, the net effect of mechanical loading is a reduction in maximum asperity height in the contact zone for both substrates. Referring to Figure 45, there seems to be a net decrease in h_{max} in both substrates due to an increase in temperature. Figure 46 indicates that mechanical loading had no discernable effect on the root mean square roughness in the 100 grit substrate, and a slight decrease in Sq for the 600 grit substrate. On the other hand, as depicted in Figure 47, temperature facilitated a substantial rise in Sq from 25 °C to 250 °C and then a sharp decline 250 °C from 500 °C.

Referring to each of the substrates' surface roughness scans, as mechanical load and thermal exposure increases, the maxima seem to becoming increasingly more isolated as compared to the reference scans taken prior to the surface roughness study, which is a clear indication of plastic deformation. The anomalous rise in root mean square roughness at 250 C seems to be casued by oxidation along both stainless steel substrates surface, which resulted in large deformations in the respective surface scans.

Table 17: Summary of surface characterization statistical results for various experimental conditions.

Run	Scan	Stress (MPa)	Temperature (°C)	S_q (µm)	c_{max} (µm)	h_{max} (µm)
1	100 grit	0	25	2.293	8.456	13.042
2	100 grit	0.689	25	2.349	13.961	18.747
3	100 grit	2.068	25	2.327	11.608	14.525
4	100 grit	3.447	25	2.339	10.008	15.761
5	100 grit	0	250	13.427	30.510	32.552
6	100 grit	0	500	2.347	6.039	14.226
1	600 grit	0	25	0.806	3.125	7.380
2	600 grit	0.689	25	1.124	14.819	12.202
3	600 grit	2.068	25	0.794	2.665	7.120
4	600 grit	3.447	25	0.811	11.129	10.476
5	600 grit	0	250	2.413	9.242	10.174
6	600 grit	0	500	0.817	3.125	9.543

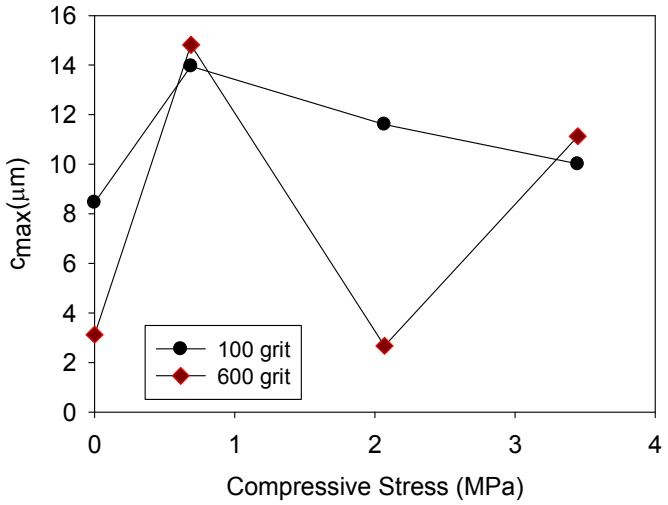

Figure 42: Ten-point maximum as a function of average compressive stress.

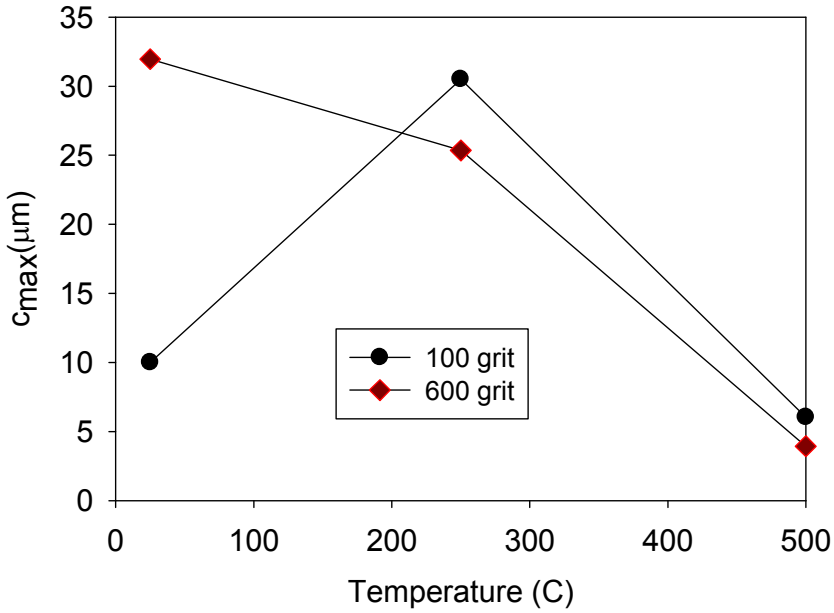

Figure 43: Ten-point maximum as a function of temperature.

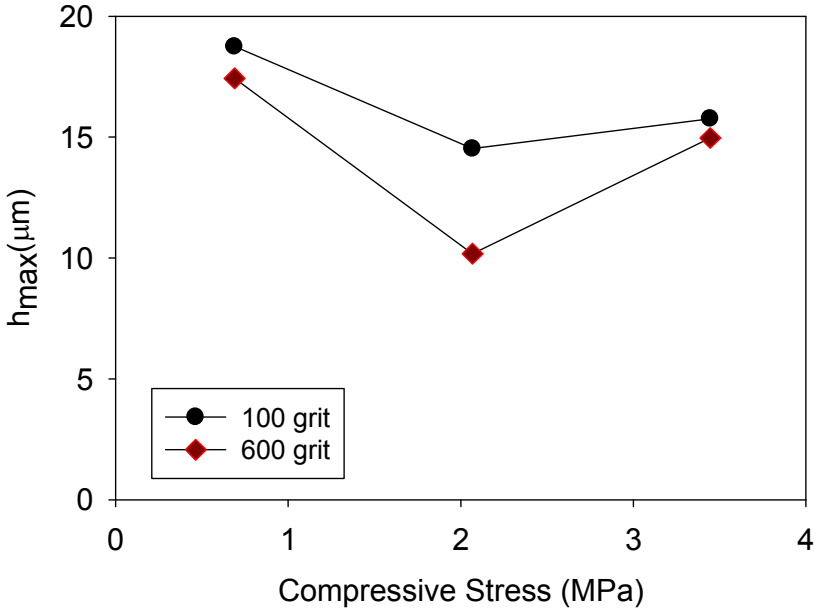

Figure 44: Nominal contact area asperity height maximum versus average compressive stress

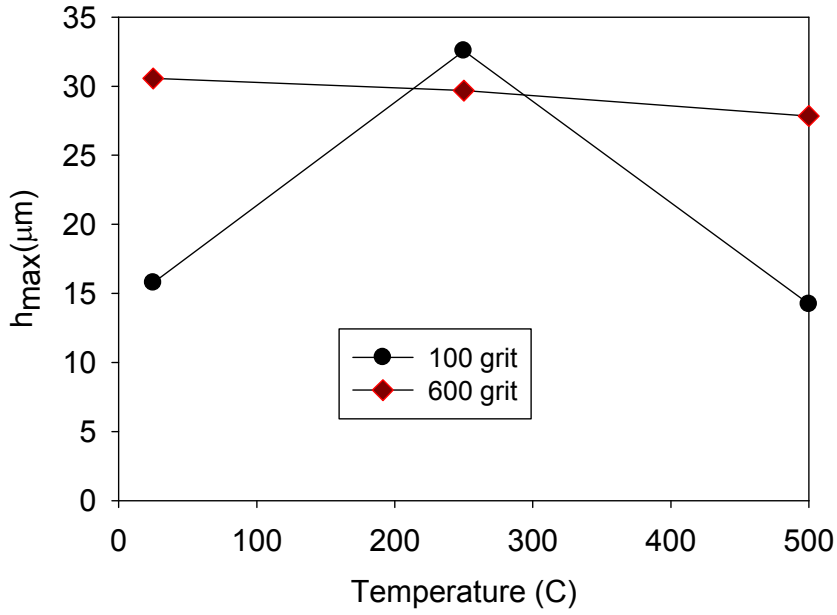

Figure 45: Nominal contact area asperity height maximum versus temperature

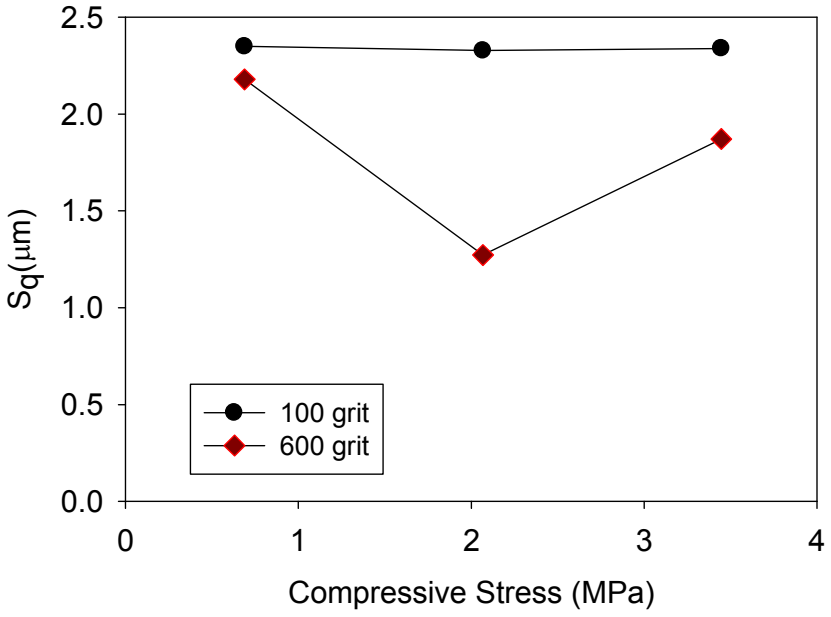

Figure 46: Root mean square surface roughness versus compressive stress.

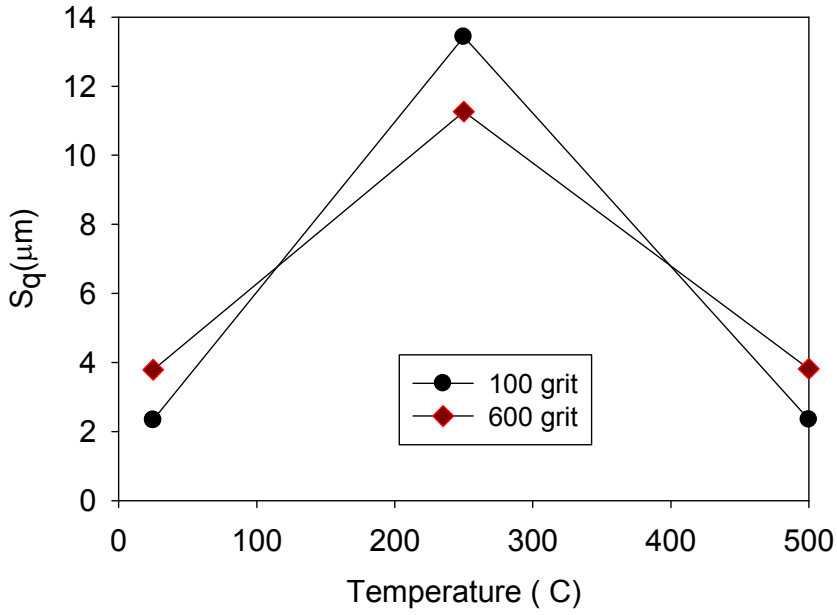

Figure 47: Root mean square surface roughness versus temperature.

10.4. Surface Characterization Summary

A surface characterization study was performed to ascertain the effect mechanical loaded and elevated heat exposure have on the surface roughness scan of two stainless steel substrates. Based on the study results, the following observations can be made:

1. Elevated heat exposure results in a decrease in root mean square roughness, ten-point maximum height, and maximum surface height in nominal contact zone, which demonstrates that asperities are flattened across the surface.

2. An increase in mechanical loading resulted in a monotonic decrease in surface height parameter in the 100 grit substrate, while the 600 grit substrate actually experienced an increase in key surface parameter. Thus, mechanical loading can indeed smooth a rough surface by plastically deforming surface asperities. However, there is a limit to this reduction.
3. Root-means square surface slightly decreased with respect to mechanical loading, but experience large fluctuations due to oxidation along the substrate.

11. LEAKAGE RESULTS- MULTI-INTERFACE MICA LAYERS

11.1. Multi-Interface Mica Overview

In this chapter, the previously introduced elastic-only computational leakage model predictions are compared to experimental leakage test results. In the current study, a mica-based compressive seal configuration is analyzed, and is depicted in Figure 48. During this study, mica layers were stacked so that there were one, two and five leakage paths, respectively, for a given compressive seal configuration. For example, the two leakage path interface consisted of two mica sheets. The top sheet, which is in direct contact with the Inconel annulus, has a 0.5 inch diameter hole in its center. The hole enables pressurized gas to flow down to the bottom mica sheet. Hence, in the two leakage path configuration, there is an Inconel-mica interface as well as a mica-mica interface. Both of which allow pressurized Argon to flow into the ambient surroundings. In the literature, it has been demonstrated that the Inconel-mica interface is the dominant leakage path. This forthcoming analysis seeks to quantify the leakage at each interface, and in turn, further elucidate leakage in several points of interests.

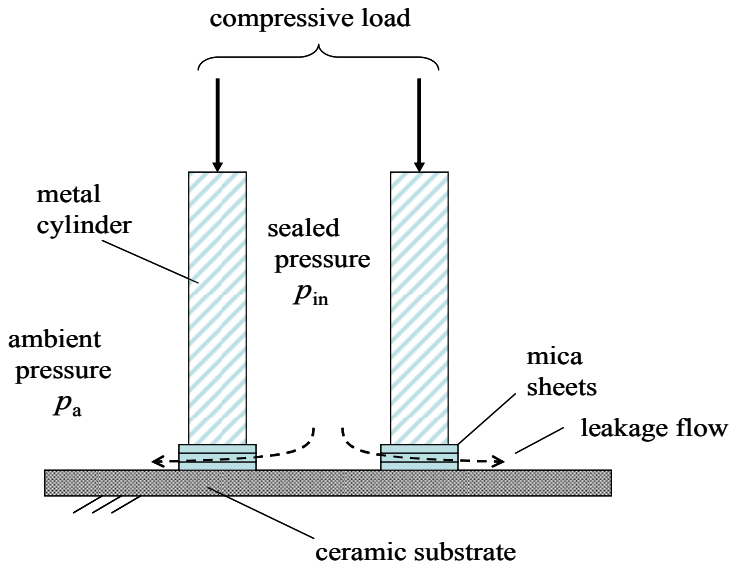

Figure 48 : Schematic of Experimental Model of Mica Compressive Seal.

The corresponding leakage test matrix is included as shown in Table 18. In this particular study, each row or test combination was performed five times in an effort to increase the statistical certainty of the average measurement. Unlike the two prior metal-metal compressive seal analyses, only a single compressive load of 300 psi (2.046 MPa) is used throughout the duration of the current study so that the influence of the number of interfaces can be isolated. Another distinction from the previous studies is that the surface roughness is analyzed as received rather than altering the surface of the phlogopite mica layer. Moreover, since the mica layers are flexible and can easily be bent additional measures needed to be taken to ensure the surface roughness scan is not altered due to a curve in the surface as opposed to the actual topographic undulations. As a result, a best fit paraboloid is subtracted from the raw surface data minimize the effect of curvature on the impending surface roughness scan. The generalized

equation for the paraboloid is given by the following expression: $z(x,y) = z_0 + ax + by + cx^2 + dy^2$ where a, b, c, and d are constants determined via a regression analysis.

Table 18: Test matrix used in mica-based compressive seal leakage study.

Stress (MPa)	Temp. (C)	Mica layers
2.048	25	1
		2
		5
	250	1
		2
		5
	500	1
		2
		5

11.2. Multi-Interface Macro Contact Model

Although the modeling approach for the multi-interface mica compressive seal assembly is similar to the approach used for the metal-metal compressive seal macro model introduced in previous chapters, there were several modifications that needed to be implemented. First, since each mica layer is only .004” (0.10 mm) thick and the entire Inconel annulus test piece is approximately 4” tall, the previous macro contact model used in the metal-metal compressive seal could not be used in the mica-based compressive seal contact model due to the dramatic difference in the relative height aspect ratios. As a result, the Inconel model was simplified as depicted in Figure 49. From the figure, the

vertically positioned annulus is modeled as a rectangular body with a width equal to the difference in the outer and inner radius of the nominal annular contact zone, while having a height equal to 0.25” (6.25 mm). The applied normal load, which is equal to the average compressive pressure multiplied by the nominal contact area, is then applied as a boundary condition along the top of the aforementioned annulus. Roller boundary conditions are instituted along the vertical line located at the inner radius of the annulus; that is, motion is restricted in the radial direction, but movement is allowed in the vertical (axial) direction.

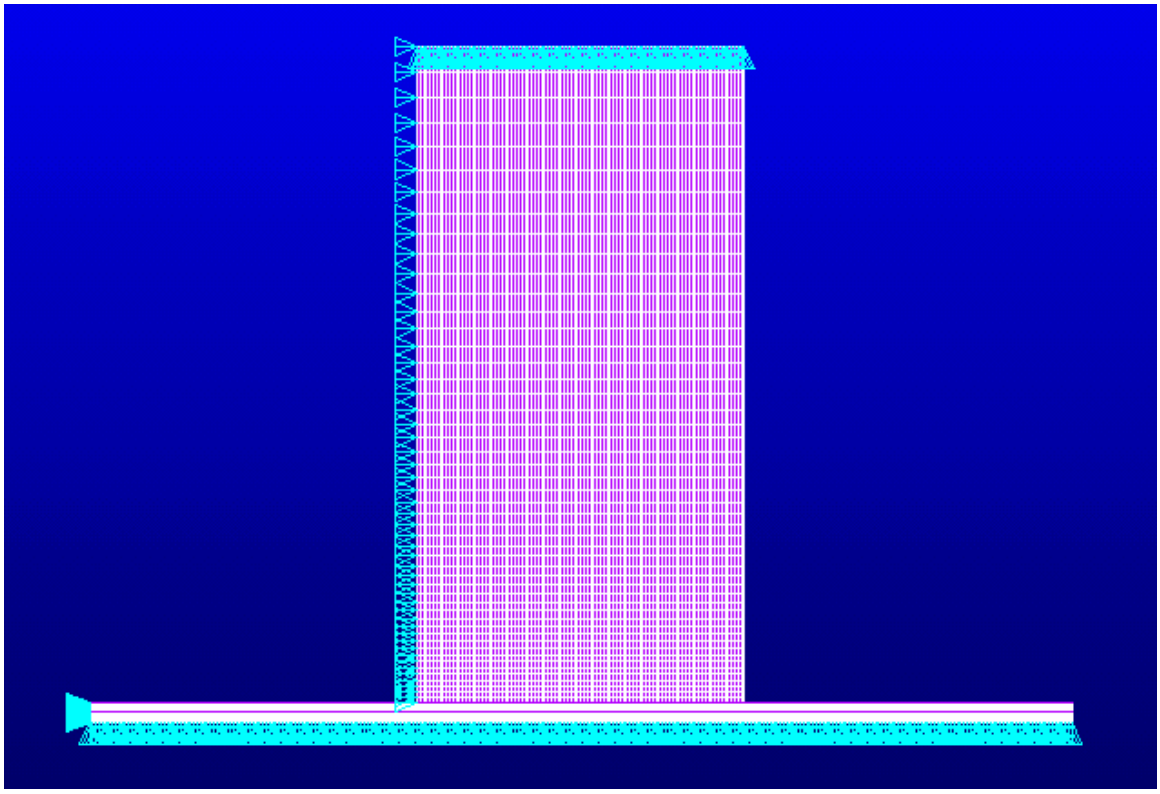

Figure 49 : Finite element representation of two mica layer compressive seal being loaded by an Inconel annulus

Each phlogopite mica layer is then modeled as a single continuous sheet. Just like before, an axisymmetric two-dimensional model is used. Target 169 elements (2-D target elements), are created at each node along the bottom of the Inconel annular zone as well as on the bottom of each mica layer, while Contact 172 elements (2-D 1-node node-to-surface elements) were created at each node along the top surface (line) of each mica layer. The Contact 172 elements act as compressible linear springs that ascribe a load given the overall compression of the spring. As the aforementioned target elements move towards the contact elements, the former compresses the spring-loaded Contact 172 elements. Although the focus of this study occurs at the surface, the elements used to populate the interior of the Inconel and mica layers are Plane 42 elements (2-D plane elements with axisymmetric key options). The pressure distribution is then determined at each nodal location iteratively on a 360° basis as depicted in Figure 50. Boundary conditions were set so that both of the mica layers are prevented from moving in the radial direction along the symmetry axis, while the bottom mica layer, which in reality is always in contact with the alumina stage throughout the loading process, is modeled with rollers underneath. The boundary and loading conditions are analogous when the model is extended to five mica layers.

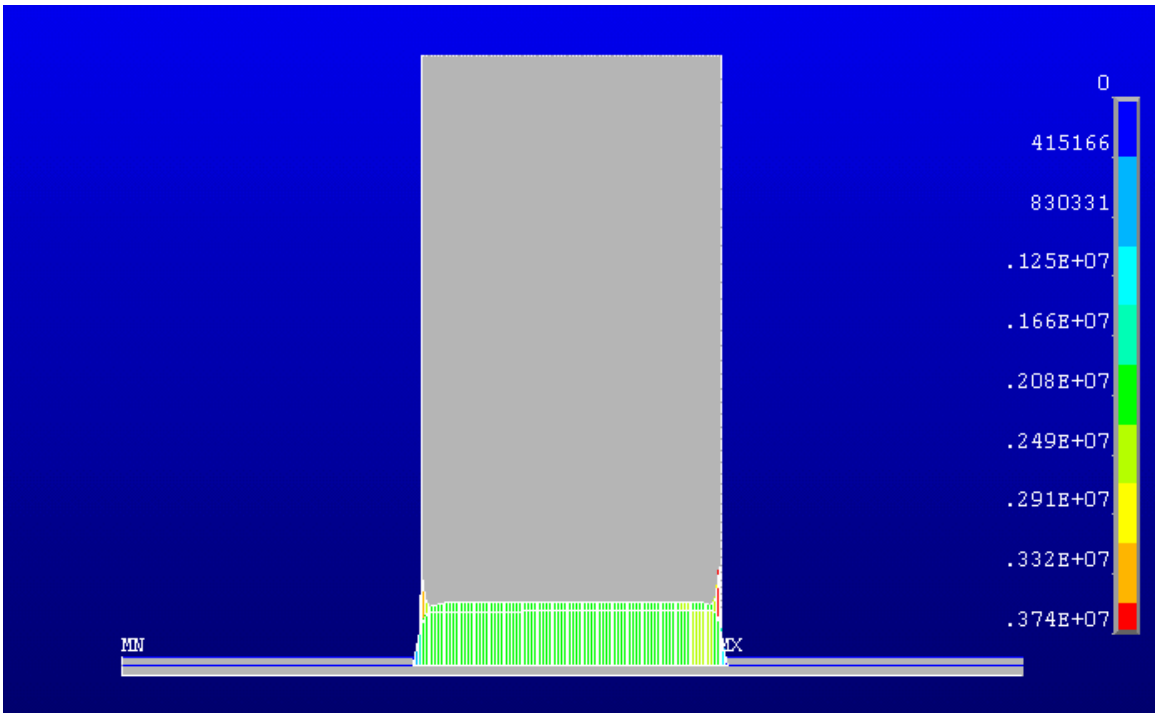

Figure 50: Resulting pressure distribution when an Inconel annulus impacts two phlogopite mica layers.

Due to the fact that the pressure distribution at multiple interfaces needs to be stored for subsequent use by the micro contact model, the corresponding pressure distributions at each interface are exported as text files. The resulting pressure distributions are then read into a MATLAB program just as before with the metal-metal compressive seals, except multiple application of the computational model are applied until leakage is predicted at each interface.

11.3. Multi-Interface Mica Results

Due to the fact that the phlogopite mica layers' thermoelastic properties are heavily influenced by several features including temperature and pressure during preparation, etc. A Dynamic Material Analyzer (DMA) was used to

approximate the elastic modulus over the experimental temperature range used in the current study. A representative plot of the elastic modulus as a function of temperature is included in Figure 51. The elastic modulus for the mica is then determined by taking the square root of the sum of the squares of the storage and loss modulus values at a given temperature value. As previously mentioned, the mica layers used in the leakage study were only 0.1 mm thick. However, the DMA could not accommodate specimens that thin. As a result, a thicker phlogopite mica sample (0.25 in) was used to determine the elastic modulus. A table of the non–temperature dependent mechanical parameters used throughout the leakage analysis is included as Table 19, while a listing of the temperature dependent properties including the dynamic viscosity of the test gas, μ, and elastic modulus of the mica is included as Table 20.

Table 19: Mechanical properties and parameters that were used throughout mica compressive seal study.

Parameter	Value
R	208 J/kg K
ri	12.70 mm
ro	15.875 mm
Δp	2.0 kPa
v	0.22
Einc	193 GPa

Table 20: Thermo physical properties used throughout mica compressive seal study.

T (°C)	μ (Pa*s)	E_{mica} (GPa)	$\rho(kg/m^3)$
25	2.26E-05	64.10	1.634E-03
250	3.58E-05	23.85	9.312E-04
500	5.06E-05	15.26	6.300E-04

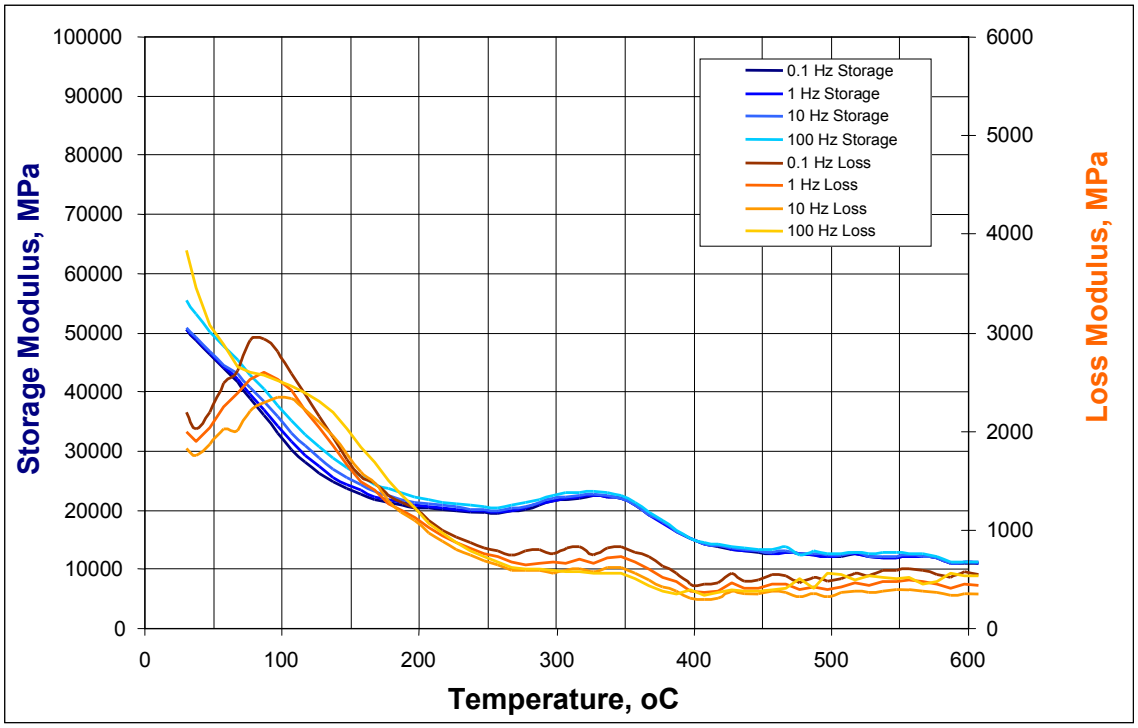

Figure 51 : Elastic modulus for phlogopite mica was approximated from room temperature to 600 °C using a Dynamic Material Analyzer.

A mica-based compressive seal leakage study was performed using the elastic only formulation of the leakage computational model. After the surface roughness scan was performed on the mica sample, a best-fit paraboloid of the form was used to counteract deviations in the surface roughness scan due to the mica layer not being flat. A representative surface roughness scan used for the mica study is included as Figure 52. Note how the specimen bows when examined on a microscale. Once the pressure distribution and the mean surface

separation at each node within the mica interfaces were determined, the volumetric leakage rate was computed for the three distinct compressive seal configurations. Representative plots for the pressure distribution in the 2-mica layer compressive assembly are included with the Inconel-mica interface appearing in Figure 53 , while the mica-mica interface is depicted in Figure 54. The pressure distribution is the highest for both of the aforementioned plots at the radial locations corresponding to the annulus's infinitely sharp edges. As expected, as the radius increases the average pressure seems to stabilize at 2.04 MPa in both plots. A summary of the leakage results is included as Table 21, while the experimental uncertainty associated with the mean is included as Table 22.

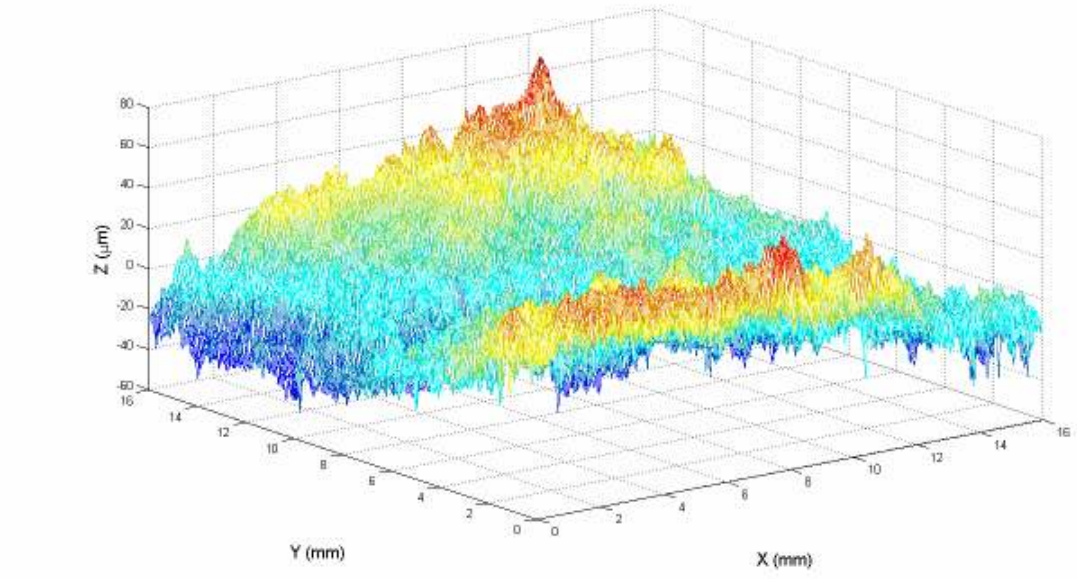

Figure 52: A representative surface roughness scan of phlogopite mica used in the mica-based compressive seal experiments.

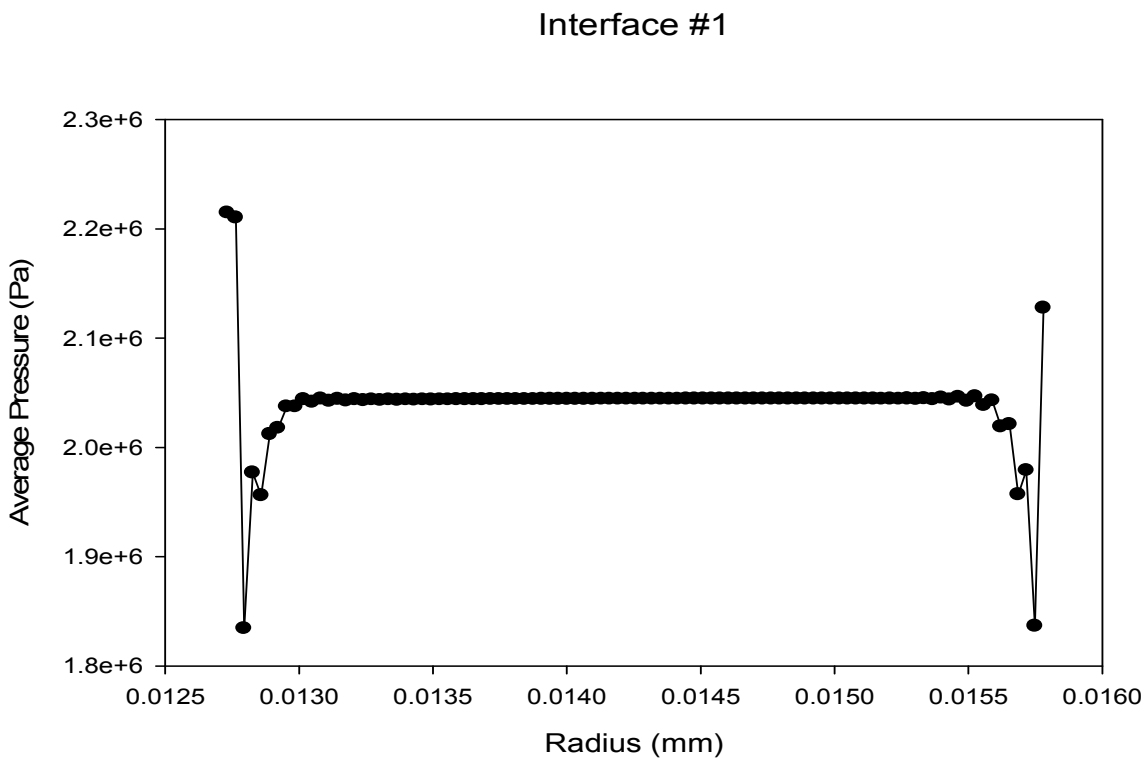

Figure 53: Representative pressure distribution of Inconel-mica interface in a 2-layer mica-based compressive seal.

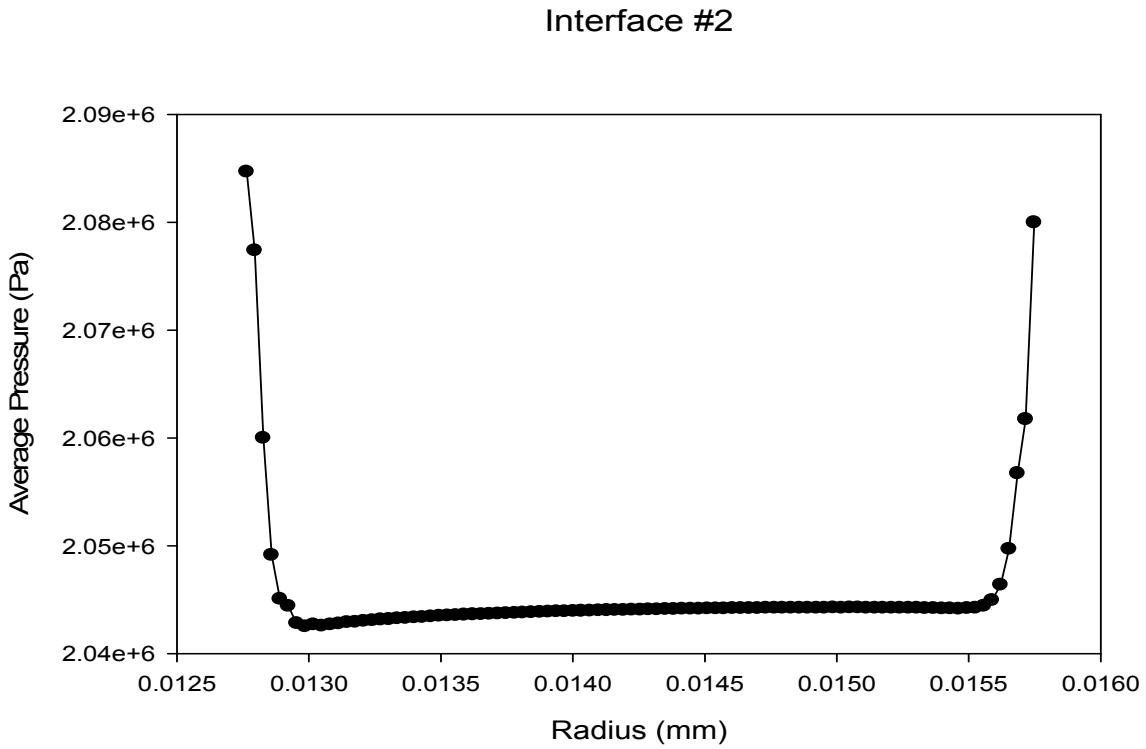

Figure 54: Representative pressure distribution of mica-mica interface in a 2-layer mica-based compressive seal.

Table 21: Summary of leakage results determined in the mica-based compressive seal study.

Leakage Results (sccm/cm)				
Temp, C	Stress(MPa)	Mica layers	Average	Elastic
25	2.068	1	1.8307	3.459
25	2.068	2	0.6573	3.610
25	2.068	5	0.6282	4.064
250	2.068	1	0.4003	2.186
250	2.068	2	0.3793	2.281
250	2.068	5	0.4510	2.568
500	2.068	1	0.4106	1.545
500	2.068	2	0.2888	1.612
500	2.068	5	0.2176	1.815

Table 22: Standard error associated with mica compressive seal experimental results.

Experimental Standard Error (sccm/cm)			
Temp, C	Stress(MPa)	Mica layers	σ_u
25	2.068	1	0.2501
25	2.068	2	0.0188
25	2.068	5	0.1316
250	2.068	1	0.0269
250	2.068	2	0.0397
250	2.068	5	0.0214
500	2.068	1	0.0491
500	2.068	2	0.0391
500	2.068	5	0.0304

The chief aim of the current study was to investigate how the temperature and the number of mica layers impact leakage rates in a mica-based compressive seal assembly. The volumetric leakage rate was plotted versus the

number of mica layers at temperatures of 25 and 500 °C, respectively, and the corresponding plots are included as Figure 55 and Figure 56. According to the figures, the elastic computational model over predicts the experimental leakage. In addition, results are contradictory as it relates to the effect the number of mica layers has on leakage. The experimental results indicate that the leakage decreases when the number of mica layers is increased within the compressive seal assembly, although the effect diminishes dramatically as temperature increases to 500 °C. On the other hand, the leakage model indicates an increase in the volumetric leakage rate is a consequence of adding mica layers to the compressive seal assembly. Looking more closely at the experimental data within the aforementioned plots, the error bars encapsulating the average leakage measurements indicate that the effect of additional mica layers is minimal as temperature increases. The discrepancy between the model and the experimental results may be attributed to the plastic deformation occurring in the leakage interfaces. As the number of mica layers increases, there is a cushioning effect as a result of the additional layers that not only allows mica to conform more readily at the mica-Inconel interface, but also the increased deformation also reduces the surface separation in between mica layers. The elastic model's predictions indicate that each of these interfaces behave in a more stiff fashion that observed experimentally, which ultimately causes the model's assessment to counter experimental trends. It would be instructive to determine the yield strength properties associated with mica so that an elastic

plastic analysis may be performed. Such analysis should more accurately capture the excessive deformation that occurs when the mica is loaded.

The effect of temperature on the volumetric leakage rate was also investigated for the three compressive seal configurations. The volumetric leakage rates versus temperature was plotted for the single and five mica layer compressive seal assembly, and is included as Figure 57 and Figure 58, respectively. The above figures indicate that an increase in temperature results in a decrease in leakage regardless of the number of mica layers present, which is confirmed by both the leakage computational model predictions and experimental results. These results are consistent with the prior two leakage studies presented involving the metal-metal compressive seals.

Using the computational model, the dominant leakage path was confirmed to be the mica-Inconel interface. Per Table 23, interface 1 corresponds to the mica-Inconel interface, while the other interfaces, which are denoted 2 through 5 where applicable, are comprised solely of mica layers. Per the table, as the number of interfaces increase the percentage of gas loss at the mica-Inconel interface decreases. Nevertheless, the vast majority of the leakage occurs at the mica-Inconel interface.

Table 23 : Leakage summary at various interfaces in mica-compressive seal assembly.

T (°C)	Mica Layers	Interface 1	Interface 2	Interface 3	Interface 4	Interface 5	Total	% Loss at 1
25	1	3.459					3.459	100.00
250	1	2.186					2.186	100.00
500	1	1.545					1.545	100.00
25	2	3.46	0.15				3.610	95.81
250	2	2.19	0.10				2.281	95.81
500	2	1.54	0.07				1.612	95.81
25	5	3.46	0.15	0.15	0.15	0.15	4.064	85.12
250	5	2.19	0.10	0.10	0.10	0.10	2.568	85.12
500	5	1.54	0.07	0.07	0.07	0.07	1.815	85.12

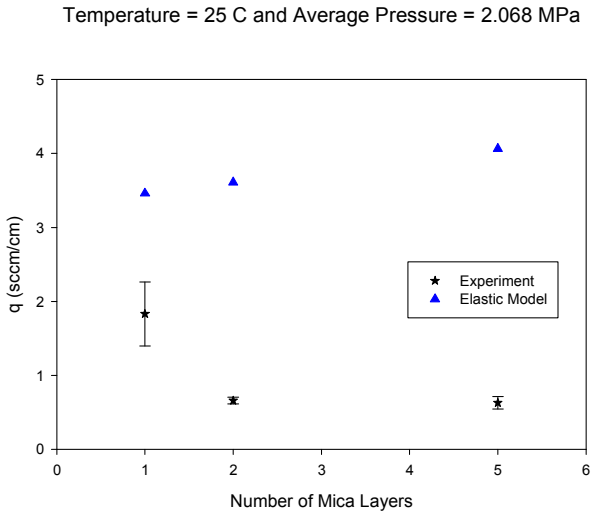

Figure 55: Volumetric leakage rate per seal length versus the number of mica layers used when T= 25 C.

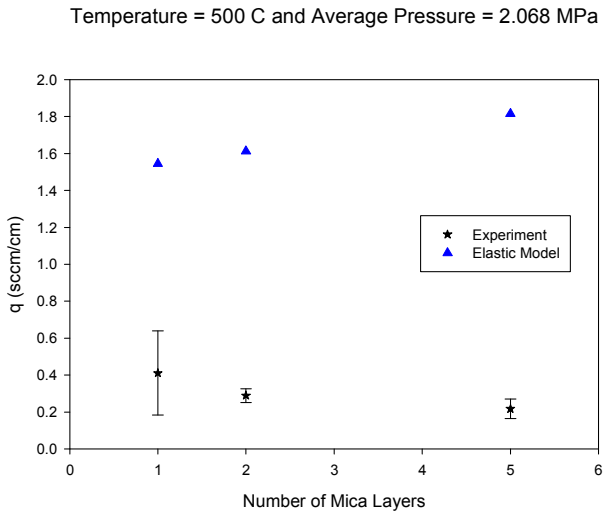

Figure 56: Volumetric leakage rate per seal length versus the number of mica layers used when T= 500 C.

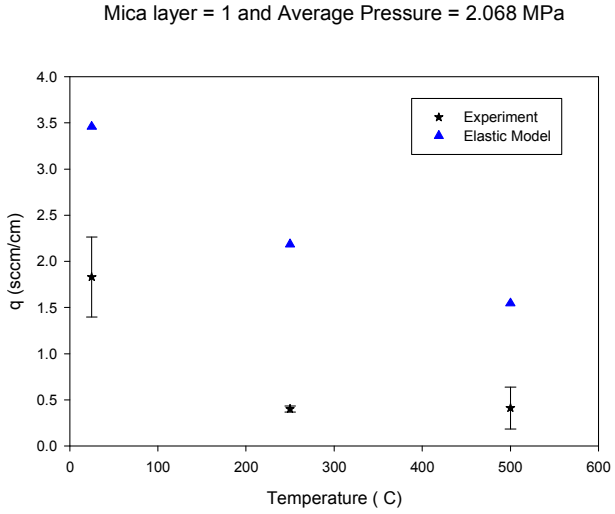

Figure 57: Volumetric leakage rate per seal length as a function of temperature in single layer compressive seal assembly.

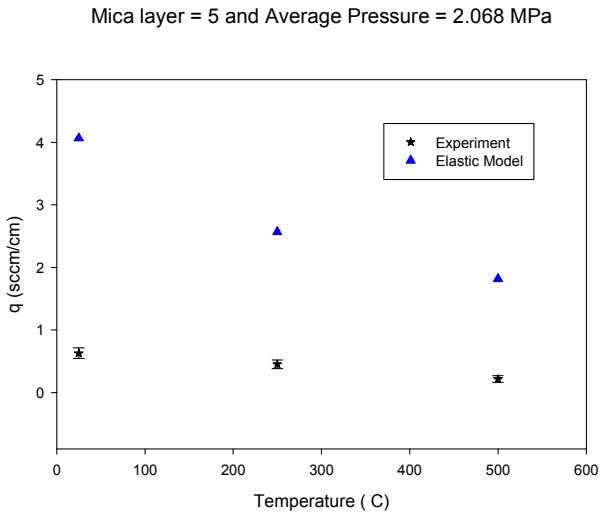

Figure 58: Volumetric leakage rate per seal length as a function of temperature in a five layer mica compressive seal assembly.

11.4. Multi-Interface Mica - Results Summary

A computational leakage model was presented to describe how temperature and the number of phlogopite mica layers affect the volumetric leakage rate in a multi-interface mica compressive seal. A finite element- based macro-contact model was used to determine the contact pressure distribution on the surface of the stainless steel substrate. Next, the Jackson-Streator (JS) micro-contact model was used to determine the localized surface separation using the FFT of surface profile measurements. Elastic deformations were solely considered in the current study due to the fact that there was no data or experimental apparatus available to approximate the yield strength for the mica used throughout the current leakage study. Once the mean spacing and pressure distribution was determined, a mixed lubrication model could then be used to

approximate the volumetric leakage rate. The leakage model predictions over estimated the volumetric leakage as compared to the experimental results. The following observations can be made:

1. Both the computational model and leakage results confirm that the volumetric leakage rate decreases as temperature increase without regard for the number of layers present.
2. Experimental leakage results indicate that leakage decreases with an increase in the number of interface. However, the effect was minimal, especially at temperatures above 25 °C. The computational model indicates that there is a positive correlation between leakage and added interfaces; that is, an increase in leakage paths promotes an increase in leakage.
3. The computational model was able to confirm and quantify the volumetric leakage loss at the primary interface as well as secondary interfaces.

12. RESEARCH IMPACT

Both an elastic and elastic-plastic contact mechanics-based computational leakage models have been developed to assess leakage in various compressive seal configurations and loading conditions. In particular, the effect of temperature, applied compressive stress, and surface roughness has been examined to determine each parameter's impact on leakage in a compressive seal. Metal-metal compressive seal leakage studies have been conducted not only to demonstrate proof-of-principle, but also to accentuate how well model predictions capture experimental leakage results. A distinction from most of the published contact mechanics-based leakage models is that each model's predictions have been experimentally validated. In addition, these model overcome the ambiguity of scale issue associated with statistically –based contact models by employing a new Fast Fourier Transform based micro contact model. The Jackson-Streator micro contact model, whose performance has been experimentally validated indirectly through the previously mentioned leakage studies, captures the multi-scale nature of micro-scaled contact, while also providing a single unambiguous solution. As a complement to the metal-metal compressive seal leakage studies, additional leakage studies were performed on multi-interface mica based compressive seals. Specifically, the elastic only model is used to quantify leakage in each interface of the mica-based compressive seal assemble, and also confirm the dominant and secondary leakage paths. The following observations can be made based on the conducted leakage studies:

- Smoother surfaces exhibit less leakage for identical loading and temperature conditions as compared to rougher interfaces.
- Repeated exposure to heat and mechanical loading facilitates plastic deformation, which enables a rougher surface to exhibit comparable leakage rates for identical loading and temperature conditions as compare to a smoother surface.
- Volumetric leakage rates per circumferential length decrease as temperature increases for identical operating conditions due to an increase in dynamic viscosity and a decrease in density.
- An increase in mechanical loading results in a decrease in volumetric leakage rates.
- JS model predictions for effective gap were shown to compare favorably with an experimentally derived effective gap via mixed lubrication theory.
- In the elastic only analysis, it was observed that high isolated outlier peaks can adversely affect the JS model's prediction of the average surface separation. Additional surface characterization studies involving confidence intervals should be performed to more accurately determine the initial surface separation.
- Thermal effects facilitated dramatic changes in the root means square surface roughness and ten-point maximum, while

mechanical loading resulted in an appreciable decrease in these same parameters.

- A regression-based procedure for determining leakage was shown to exhibit less fluctuations as compared to the instantaneous slope approach that employs finite difference approximations.
- An Elastic only model was able to quantify and confirm primary leakage paths in the mica-based compressive seal assembly. However, additional mica characterization studies are required to assess the yield strength and elastic modulus as a function of temperature. The elastic-plastic leakage model could then be used to more accurately predict leakage rates as compared to experimental results.

13. FUTURE WORK – SUGGESTED IMPROVEMENTS

13.1. Metal-Metal Compressive

Both an elastic and elastic-plastic computational leakage models have been developed to assess leakage in various compressive seal configurations and loading conditions. Although the modeling results compared favorably with experimental results in the series of studies presented, opportunities for further improvement will be included in the forthcoming discussion.

As a point of emphasis, the current design methodology's principal aim was to evaluate the effectiveness of a new micro contact model namely the Jackson-Streator Model. Stochastic models like the GW Model[59] and others that expand from its framework have been shown to provide favorable results for a very specific and often design constrained context. However, the aforementioned models fail to provide a single solution as it relates to approximating the average gap. Instead, an arbitrary criterion is often used to quantify the radius of curvature and other key parameters so that a solution may be specified for the problem at hand. In a general sense, these models provide a family of solutions for the average gap problem. It is in this vein, the Jackson-Streator model was used in the present model not only because it captures the multi-scale nature of micro contact rather than relegating the contact scale to the one most convenient, but it also allows a researcher to obtain a single solution

based on the loading conditions and surface scans. Secondly, although the present model does indeed provide corresponding amplitude for spatial frequency-related information in order to approximate the average gap, the frequency spectrum information is never mapped back to corresponding locations per the surface roughness scan. Thus, this model is not purely deterministic. Lastly, the intent of the computational leakage model was to capture the dominant mode of leakage by averaging the micro-scaled gap at a given interface. As result, this model does not attempt to capture secondary modes of leakage including the diffusion of gas through a solid medium.

There are four suggestions offered for improved results if one were to model leakage using the same approach presented previously. First, a surface characterization study regarding the effect of load should be implemented to thoroughly understand the initial surface separation prior to loading based on an arbitrary profile. In the metal-metal compressive seal leakage tests, the resulting mean surface separation is adversely affect by isolated high asperity peaks when the over root mean square surface roughness is still approximately 2. In reality, those isolated asperities are most like plastically deformed. However, this scenario is not adequately captured with the current approach. Next, the surface characteristics of both surfaces in given interface should be considered. The current model results seemed to be less sensitive to load than its experimental counterpart. Although modeling both surfaces could indeed prompt an overestimation of leakage at lower loads due to the fact that the surface separation in the top surface is also considered, with sufficient compressive load,

the model should be able to more precisely capture the effect of the applied compressive load has on leakage. The surface characteristics of two surfaces could be transformed into an equivalent roughness profile such that a perfect smooth annulus is contacting an equivalent rough surface model, which is similar to the present case. Next, residual stresses could be incorporated into the micro contact approach to further improve results, especially if either surface is strain hardened. Jackson et al. [60] accounted for residual stresses in the finite element hemispherical model recently. Since the surface topography of the stainless steel substrate did indeed change over the course of various leakage experiments, it seems that the aforementioned model is a logical extension to the current study. Lastly, in the current model, Patir and Cheng's isotropic flow factors provided an adequate correction on the Modified Reynolds Equation. It is anticipated that when the normalized surface separation is slightly less than one, the accuracy of the aforementioned flow factors diminishes dramatically. If the mixed lubrication model employed an updated approach [61]where the effect of the contact deformation on the flow factors is taken into account, the current leakage model could then be applicable to an even wider array of leakage scenarios.

If the modeling approach is shifted to a deterministic framework, there are several techniques that can be employed in lieu of the flow factors used in the current study. Moreover, Venner [62] has demonstrated amplitude reduction technique can be performed on the FFT directly with dramatically reduced

computation time. Such an approach[63] would also sidestep the limitations associated with flow factors.

13.2. Mica-Based Compressive Assembly Model

The mica-based compressive seal model's improvements pertain more to assessing the thermophysical properties of the mica being modeled than any deficiencies in the approach per se. In the current study, the actual mica sheets that were used in the leakage experiments were actually considerably thinner than the mica samples on which the DMA was used to determine the elastic modulus as a function of temperature. However, the thickness, amount of binder used, and percentage of porosity all affect the thermophysical properties of mica. Thus, phlogopite mica properties should be assessed directly to achieve better results.

APPENDIX A – COMPLETE LEAKAGE RESULTS

Table 24: Experimental leakage study results determined for the elastic only metal-metal compressive seal study.

Avg. Stress (MPa)	Temp. (°C)	100 μgrit (sccm/cm)	600 μgrit (sccm/cm)
0.689	25	0.7384	0.3898
0.689	25	0.6882	0.3418
0.689	25	0.6917	0.3682
2.068	25	0.6121	0.3644
2.068	25	0.6024	0.4016
2.068	25	0.6331	0.3238
3.447	25	0.5249	0.3510
3.447	25	0.6448	0.3203
3.447	25	0.5933	0.1947
0.689	250	2.1825	0.3063
0.689	250	1.4096	0.1603
0.689	250	1.4948	0.2776
2.068	250	0.9055	0.1605
2.068	250	1.0286	0.1748
2.068	250	0.9518	0.2937
3.447	250	0.6772	0.1408
3.447	250	0.7308	0.1671
3.447	250	0.7058	0.1850
0.689	500	0.4449	0.1934
0.689	500	0.3550	0.3055
0.689	500	0.3671	0.2032
2.068	500	0.3646	0.1922
2.068	500	0.3508	0.1769
2.068	500	0.3279	0.1651
3.447	500	0.3264	0.1485
3.447	500	0.3282	0.1602
3.447	500	0.3442	0.1655

Table 25: Individual experimental leakage study results determined for the elastic-plastic metal-metal compressive seal study.

Stress (MPa)	Temp. (°C)	100 µgrit (sccm/cm)	600 µgrit (sccm/cm)
0.689	25	0.7047	0.6970
0.689	25	0.8690	0.7535
0.689	25	0.6913	0.7407
0.689	25	0.6876	0.8772
0.689	25	0.7105	0.7829
0.689	25	0.9742	0.7290
0.689	25	0.7485	1.0066
2.068	25	0.6987	0.5568
2.068	25	0.7208	0.6217
2.068	25	0.5745	0.5554
2.068	25	0.6701	0.6937
2.068	25	0.6505	0.5873
2.068	25	0.5899	0.6302
2.068	25	0.6085	0.5816
3.447	25	0.6184	0.6043
3.447	25	0.5651	0.5599
3.447	25	0.7390	0.5488
3.447	25	0.6484	0.5509
3.447	25	0.6595	0.5245
3.447	25	0.5625	0.5135
3.447	25	0.5429	0.4762
0.689	250	0.4012	0.2007
0.689	250	0.5214	0.3410
0.689	250	0.5600	0.3465
0.689	250	0.4012	0.3734
0.689	250	0.3710	0.3393
0.689	250	0.3515	0.3869
2.068	250	0.3896	0.3330
2.068	250	0.5223	0.3364
2.068	250	0.3480	0.3590
2.068	250	0.3986	0.3434
2.068	250	0.3634	0.3626
2.068	250	0.3174	0.3019
2.068	250	0.1532	0.3481
3.447	250	0.3324	0.3540
3.447	250	0.3023	0.2825
3.447	250	0.3966	0.3384
3.447	250	0.1816	0.1721
3.447	250	0.3523	0.3404
3.447	250	0.3380	0.2811
3.447	250	0.4092	0.3074
3.447	250	0.3867	0.1801
0.689	500	0.3557	0.1481
0.689	500	0.1627	0.2005
0.689	500	0.3493	0.2786
0.689	500	0.1797	0.1831
0.689	500	0.1692	0.3064
0.689	500	0.2686	0.1830
0.689	500	0.3339	0.1464
2.068	500	0.1319	0.2727
2.068	500	0.2072	0.1354
2.068	500	0.1949	0.1922
2.068	500	0.2820	0.1982
2.068	500	0.1646	0.1348
2.068	500	0.2956	0.1577
2.068	500	0.1647	0.2784
3.447	500	0.2607	0.1887
3.447	500	0.2590	0.1849
3.447	500	0.2761	0.1965
3.447	500	0.1724	0.2029
3.447	500	0.2154	0.1809
3.447	500	0.2820	0.1756
3.447	500	0.2933	0.1932

Table 26: Individual experimental average gap results determined for the elastic-plastic metal-metal compressive seal study.

Stress (MPa)	Temp. (°C)	100 μgrit h_{eff}(μm)	600 μgrit h_{eff}(μm)
0.689	25	7.1808	7.0128
0.689	25	7.6711	7.1952
0.689	25	7.1376	7.1547
0.689	25	7.1256	7.5653
0.689	25	7.1993	7.2866
0.689	25	7.9539	7.1173
0.689	25	7.3182	7.9174
2.068	25	7.1615	6.5139
2.068	25	7.2319	6.7540
2.068	25	6.7360	6.5085
2.068	25	7.0682	7.0019
2.068	25	7.0027	6.6289
2.068	25	6.7918	6.7842
2.068	25	6.8580	6.6077
3.447	25	6.8927	6.6913
3.447	25	6.7014	6.5257
3.447	25	7.2888	6.4830
3.447	25	6.9957	6.4911
3.447	25	7.0330	6.3875
3.447	25	6.6918	6.3433
3.447	25	6.6182	6.1886
0.689	250	8.5530	6.9422
0.689	250	9.2670	8.1408
0.689	250	9.4729	8.1804
0.689	250	8.5530	8.3682
0.689	250	8.3518	8.1285
0.689	250	8.2160	8.4590
0.689	250	8.4770	8.0825
2.068	250	9.2719	8.1074
2.068	250	8.1911	8.2688
2.068	250	8.5361	8.1581
2.068	250	8.2995	8.2939
2.068	250	7.9660	7.8464
2.068	250	6.4074	8.1918
2.068	250	8.0781	8.2337
3.447	250	7.8496	7.6909
3.447	250	8.5230	8.1220
3.447	250	6.7386	6.6320
3.447	250	8.2217	8.1365
3.447	250	8.1191	7.6794
3.447	250	8.6046	7.8893
3.447	250	8.4577	6.7220
0.689	500	10.3587	7.9240
0.689	500	8.1521	8.6855
0.689	500	10.3005	9.6055
0.689	500	8.4012	8.4491
0.689	500	8.2493	9.8912
0.689	500	9.4981	8.4477
0.689	500	10.1576	7.8965
2.068	500	7.6526	9.5424
2.068	500	8.7729	7.7130
2.068	500	8.6109	8.5745
2.068	500	9.6414	8.6550
2.068	500	8.1808	7.7027
2.068	500	9.7823	8.0756
2.068	500	8.1823	9.6034
3.447	500	9.4114	8.5267
3.447	500	9.3925	8.4742
3.447	500	9.5789	8.6324
3.447	500	8.2962	8.7170
3.447	500	8.8773	8.4182
3.447	500	9.6414	8.3426
3.447	500	9.7588	8.5880

Table 27: Summary of elastic-plastic study leakage results determined for the 100 grit metal-metal compressive seal.

100-grit Leakage Results (sccm/cm)				
Stress(MPa)	Temp (°C)	experiment	elastic model	elasto-plastic model
0.689	25	0.7694	0.7981	0.8830
2.068	25	0.6447	0.6038	0.8828
3.447	25	0.6194	0.5397	0.8829
0.689	250	0.4325	0.3315	0.5579
2.068	250	0.3479	0.3436	0.5577
3.447	250	0.3381	0.2717	0.5578
0.689	500	0.2599	0.2066	0.3943
2.068	500	0.2058	0.1956	0.3942
3.447	500	0.2513	0.1889	0.3943

Table 28: Summary of elastic-plastic study leakage results determined for the 600 grit metal-metal compressive seal.

600-grit Leakage Results (sccm/cm)				
Stress(MPa)	Temp(°C)	experiment	elastic model	elasto-plastic model
0.689	25	0.7981	0.6046	0.4970
2.068	25	0.6038	0.5827	0.4882
3.447	25	0.5397	0.5709	0.4828
0.689	250	0.3315	0.3820	0.3139
2.068	250	0.3436	0.3682	0.3083
3.447	250	0.2717	0.3607	0.3049
0.689	500	0.2066	0.2700	0.2218
2.068	500	0.1956	0.2602	0.2178
3.447	500	0.1889	0.2549	0.2154

Table 29: Standard error associated with experimental leakage results during the elastic-plastic metal-metal compressive seal study.

Standard error of experimental mean, σ_u (sccm/cm)			
Stress(MPa)	Temp (°C)	100 grit	600 grit
0.689	25	0.042	0.041
2.068	25	0.021	0.019
3.447	25	0.026	0.015
0.689	250	0.033	0.023
2.068	250	0.042	0.008
3.447	250	0.030	0.026
0.689	500	0.033	0.024
2.068	500	0.023	0.023
3.447	500	0.016	0.004

Table 30: Summary of the 100 grit effective gap results determined for the elastic-plastic metal-metal compressive seal study.

100-grit Effective Gap Results (μm)				
Stress(MPa)	Temp(°C)	experiment	elastic model	elasto-plastic model
0.689	25	7.3695	9.4676	9.1133
2.068	25	6.9786	9.3907	9.1124
3.447	25	6.8888	9.3360	9.1129
0.689	250	8.6987	9.4676	9.1132
2.068	250	8.1072	9.3907	9.1125
3.447	250	8.0735	9.3360	9.1130
0.689	500	9.3025	9.4676	9.1132
2.068	500	8.6890	9.3907	9.1125
3.447	500	9.2795	9.3360	9.1130

Table 31: Summary of the 600 grit effective gap results determined during the elastic-plastic metal-metal compressive seal study.

600-grit Effective Gap Results (μm)				
Stress(MPa)	Temp(°C)	experiment	elastic model	elasto-plastic model
0.689	25	7.3214	8.1811	7.6986
2.068	25	6.6856	8.0891	7.6564
3.447	25	6.4444	8.0379	7.6303
0.689	250	8.0431	8.1811	7.6979
2.068	250	8.1572	8.0891	7.6551
3.447	250	7.5532	8.0379	7.6289
0.689	500	8.6999	8.1811	7.6974
2.068	500	8.5524	8.0891	7.6543
3.447	500	8.5284	8.0379	7.6281

Table 32: Standard error associated with experimental effective gap during the elastic-plastic metal-metal compressive seal study

Standard error of experimental gap mean, σ_u (μm)			
Stress(MPa)	Temp (°C)	100 grit	600 grit
0.689	25	0.121	0.119
2.068	25	0.071	0.066
3.447	25	0.090	0.060
0.689	250	0.180	0.191
2.068	250	0.327	0.057
3.447	250	0.243	0.237
0.689	500	0.382	0.293
2.068	500	0.297	0.299
3.447	500	0.196	0.049

Table 33: Individual experimental leakage study results determined for the elastic only mica-based compressive seal study.

Temp. (°C)	Stress (MPa)	Mica layers	q(sccm/cm)
25	2.068	1	0.5511
25	2.068	1	1.1906
25	2.068	1	2.1399
25	2.068	1	1.9588
25	2.068	1	2.0336
25	2.068	2	0.6185
25	2.068	2	0.5983
25	2.068	2	0.7044
25	2.068	2	0.6739
25	2.068	2	0.6916
25	2.068	5	0.4816
25	2.068	5	0.6713
25	2.068	5	0.6387
25	2.068	5	0.6510
25	2.068	5	0.6983
250	2.068	1	0.4411
250	2.068	1	0.3614
250	2.068	1	0.3994
250	2.068	1	0.3993
250	2.068	1	1.5175
250	2.068	2	0.3446
250	2.068	2	0.3490
250	2.068	2	0.5012
250	2.068	2	0.3376
250	2.068	2	0.3640
250	2.068	5	0.3960
250	2.068	5	0.5167
250	2.068	5	0.4427
250	2.068	5	0.3760
250	2.068	5	0.5237
500	2.068	1	0.1721
500	2.068	1	0.1748
500	2.068	1	0.6015
500	2.068	1	0.6491
500	2.068	1	0.4553
500	2.068	2	0.3330
500	2.068	2	0.3154
500	2.068	2	0.2724
500	2.068	2	0.2850
500	2.068	2	0.2382
500	2.068	5	0.2182
500	2.068	5	0.1896
500	2.068	5	0.3062
500	2.068	5	0.1706
500	2.068	5	0.2031

APPENDIX B – SURFACE ROUGHNESS SCANS

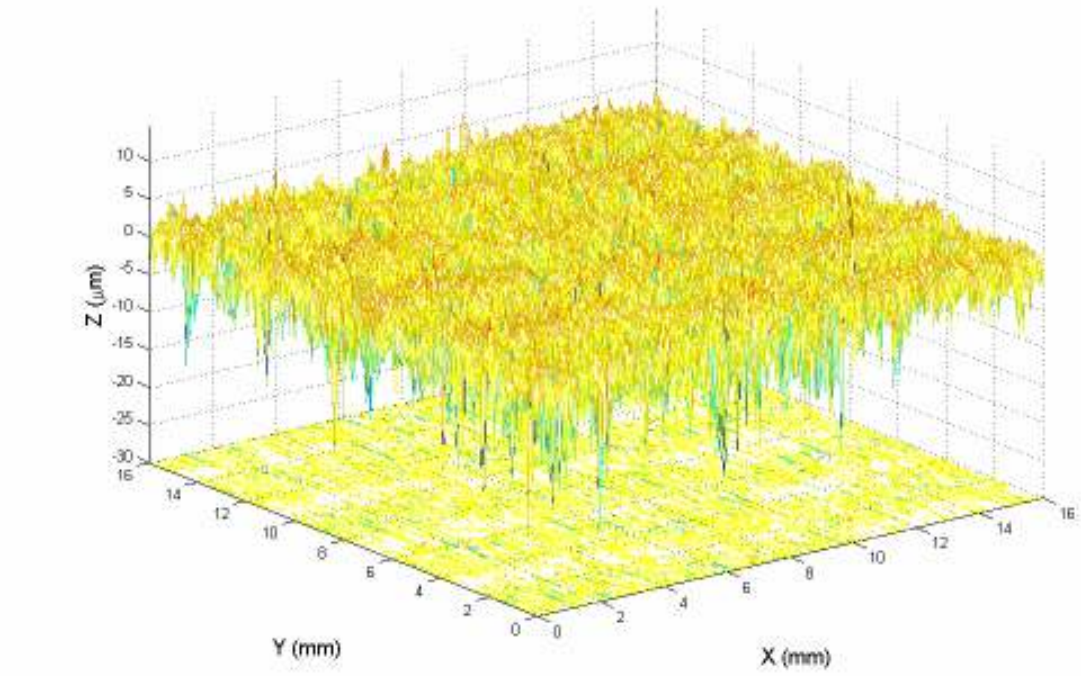

Figure 59: Surface roughness scan of 100 grit reference surface analyzed in surface characterization study.

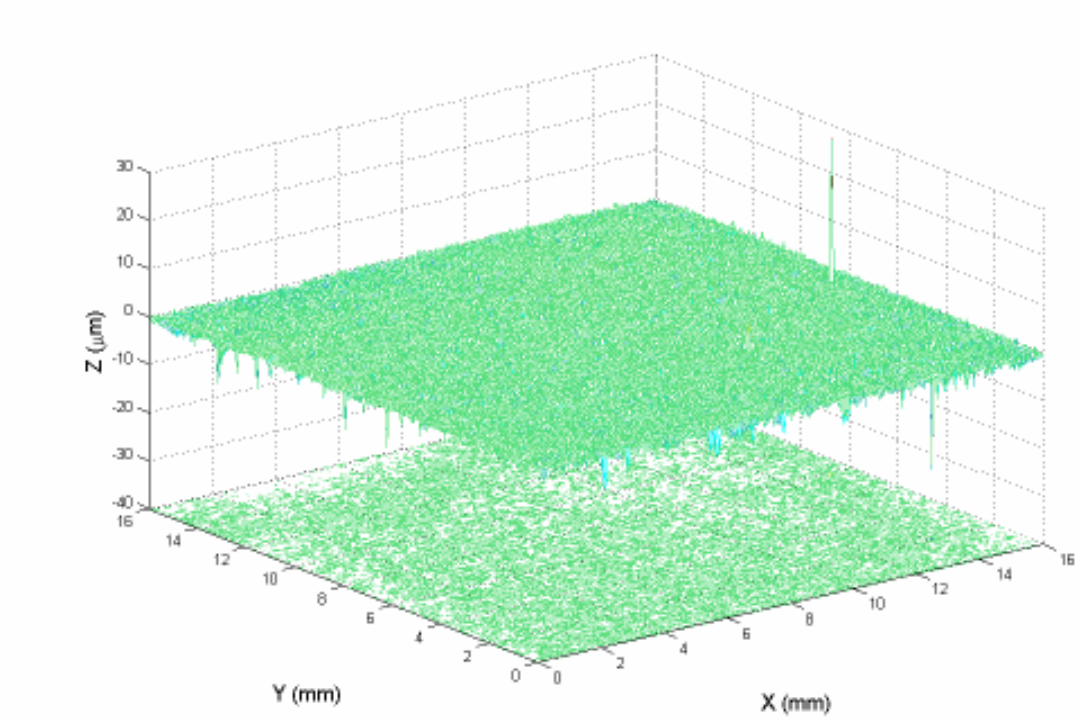

Figure 60: Surface roughness scan of 600 grit reference surface analyzed in surface characterization study.

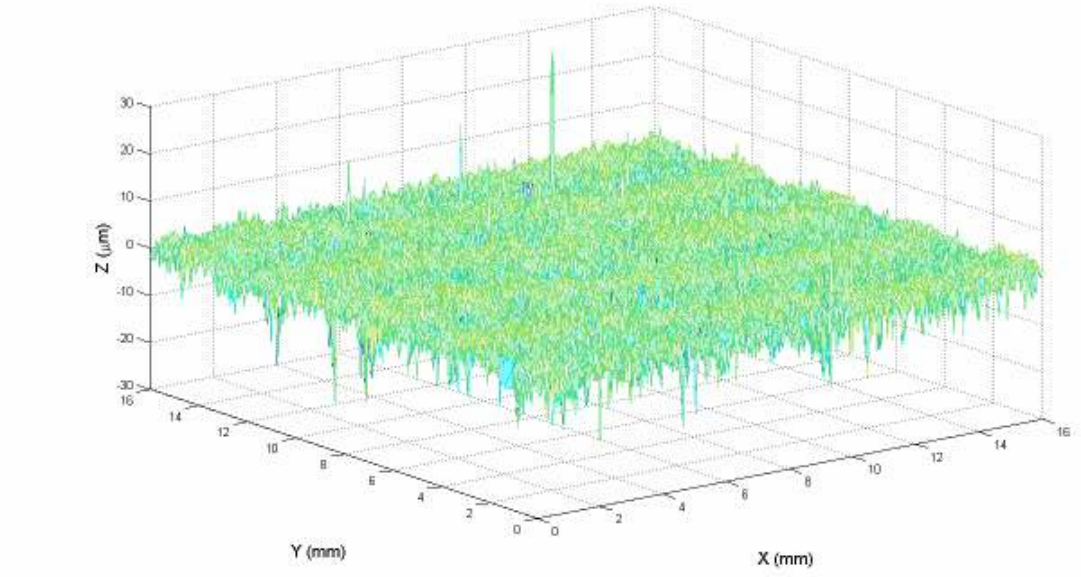

Figure 61: Surface scan of 100 grit stainless steel substrate after 0.689 MPa (100 psi) compressive stress.

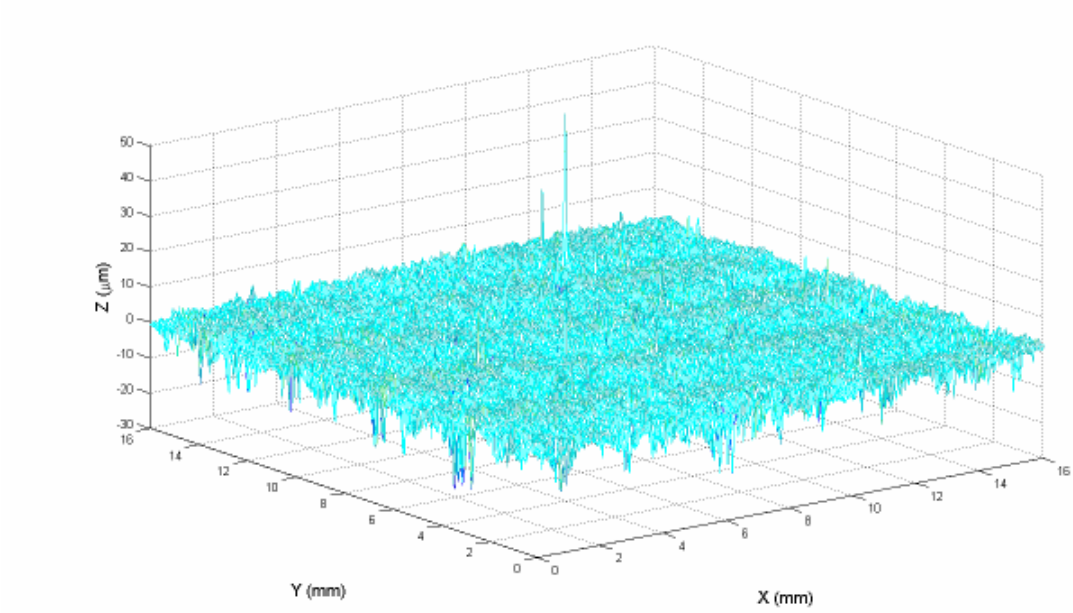

Figure 62: Surface scan of 100 grit stainless steel substrate after 2.068 MPa (300 psi) compressive stress.

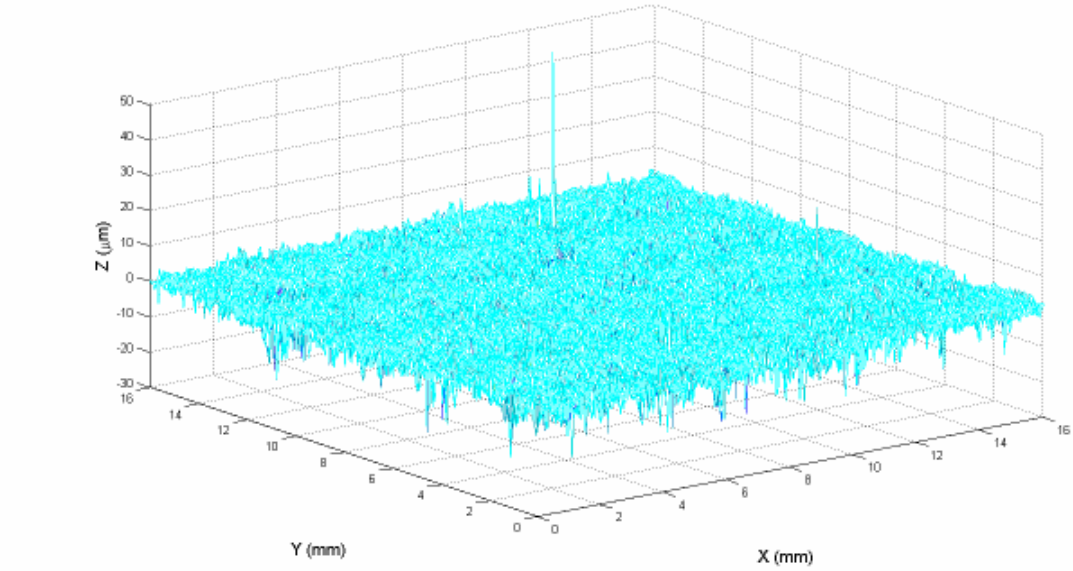

Figure 63: Surface scan of 100 grit stainless steel substrate after 3.447 MPa (500 psi) average compressive stress.

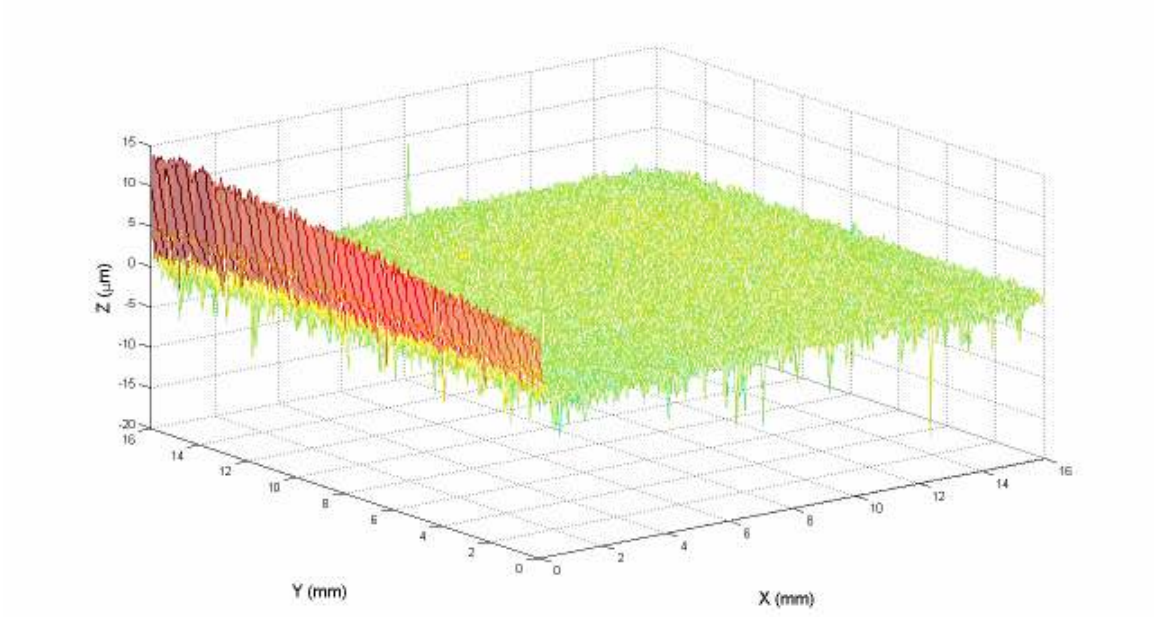

Figure 64: Surface scan of 600 grit stainless steel substrate after 0.689 MPa (100 psi) average compressive stress.

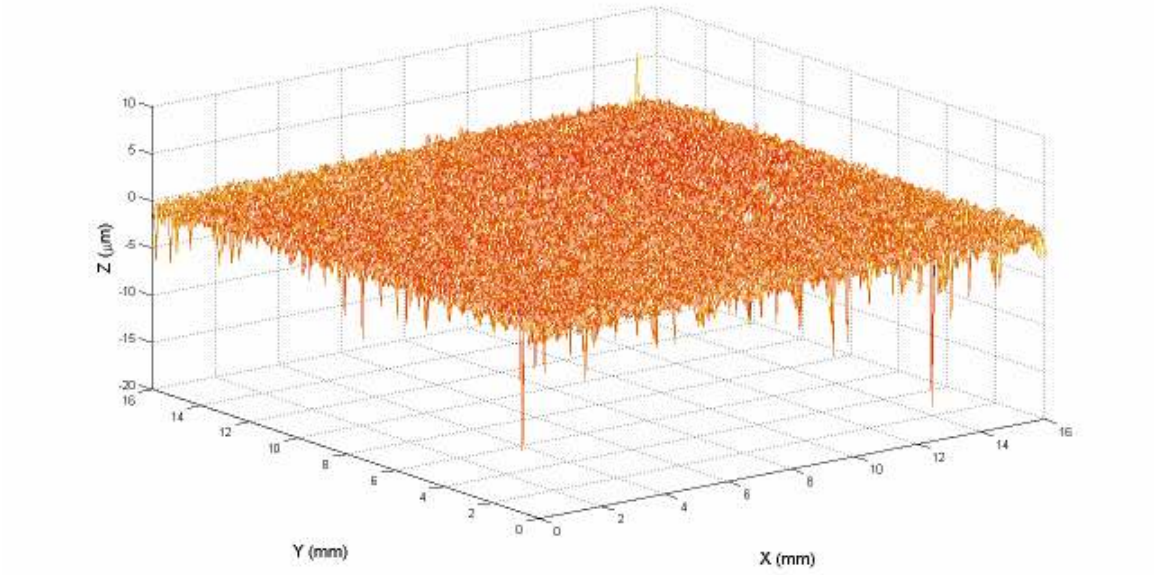

Figure 65: Surface scan of 600 grit stainless steel substrate after 2.068 MPa (300 psi) average compressive stress.

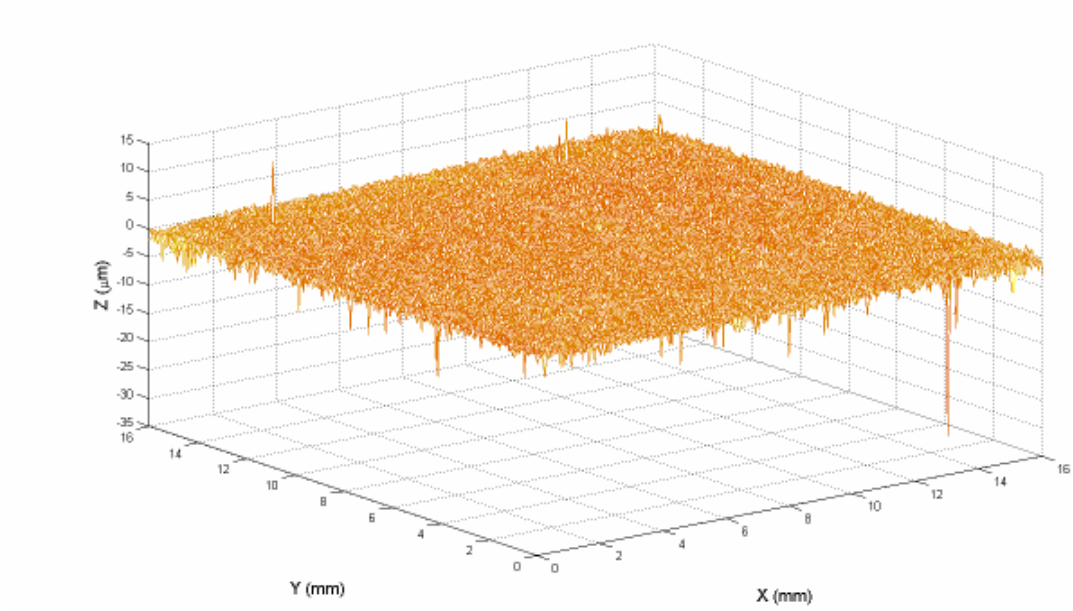

Figure 66: Surface scan of 600 grit stainless steel substrate after 3.447 MPa (500 psi) compressive stress.

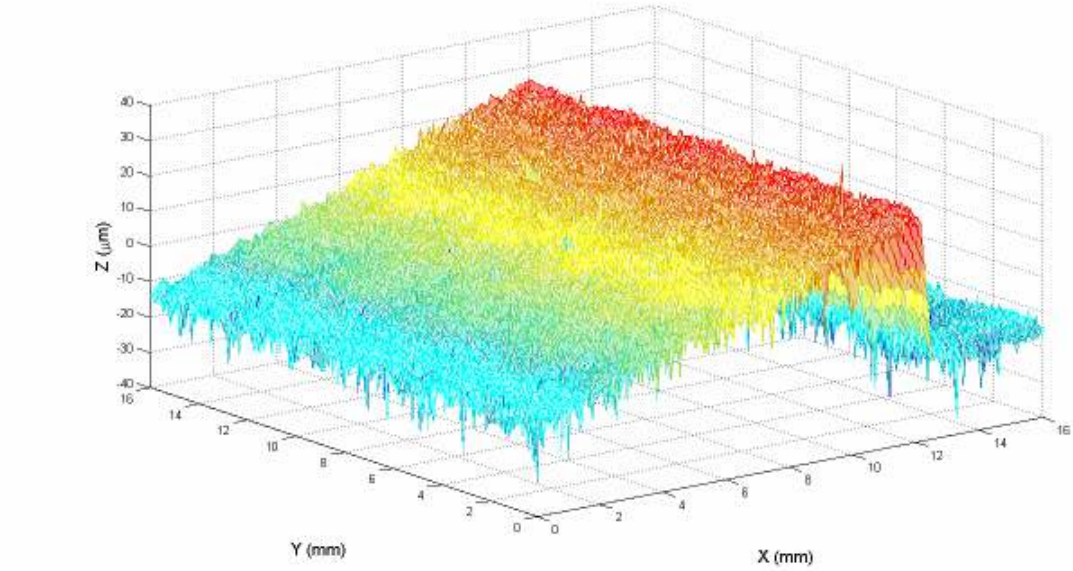

Figure 67: Surface scan of 100 grit stainless steel substrate after elevated temperature exposure at 250 °C.

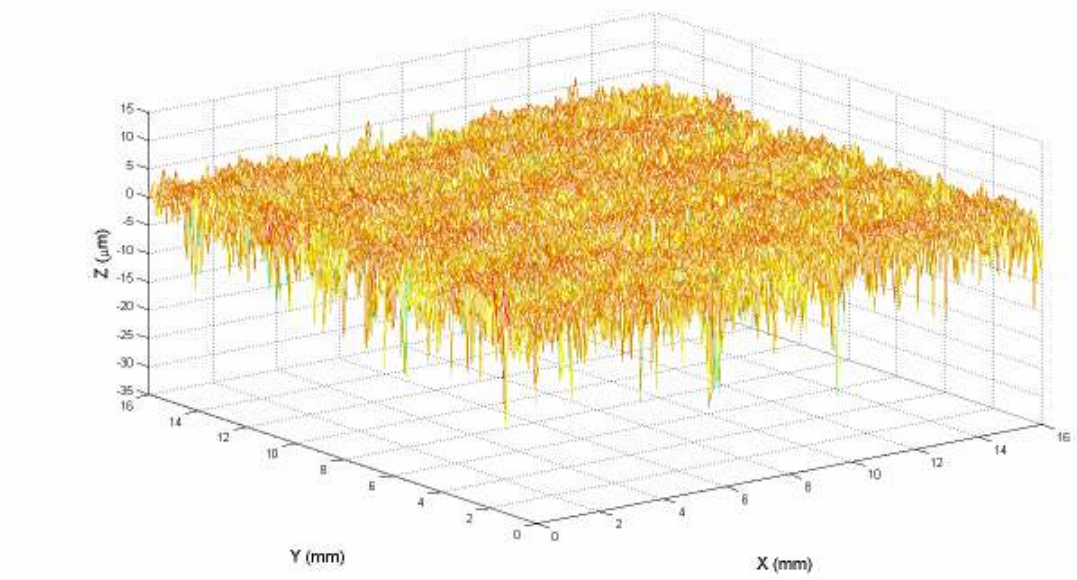

Figure 68: Surface scan of 100 grit stainless steel substrate after elevated temperature exposure at 500 °C.

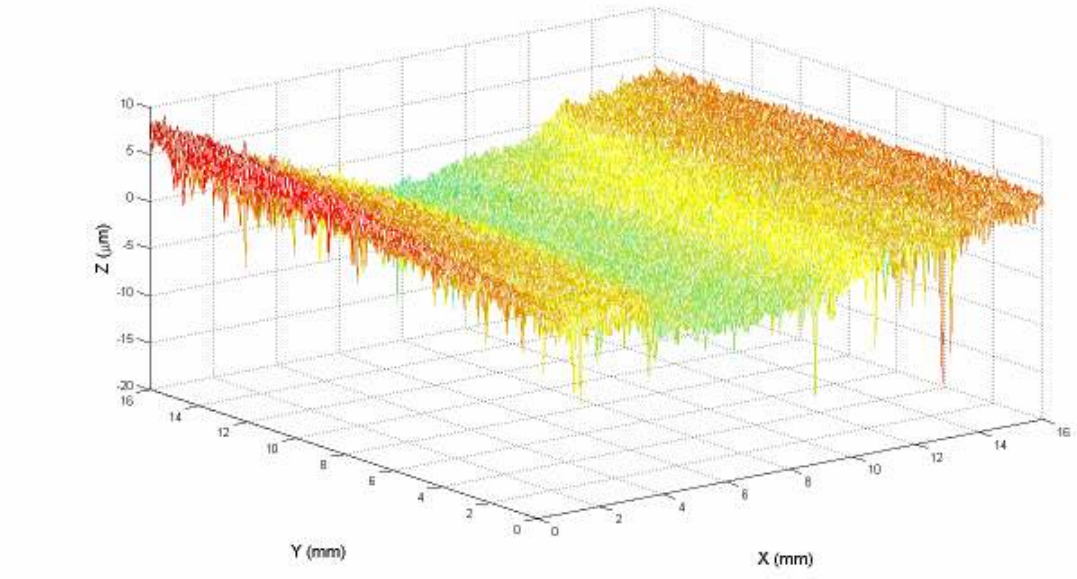

Figure 69: Surface scan of 600 grit stainless steel substrate after elevated temperature exposure at 250 °C.

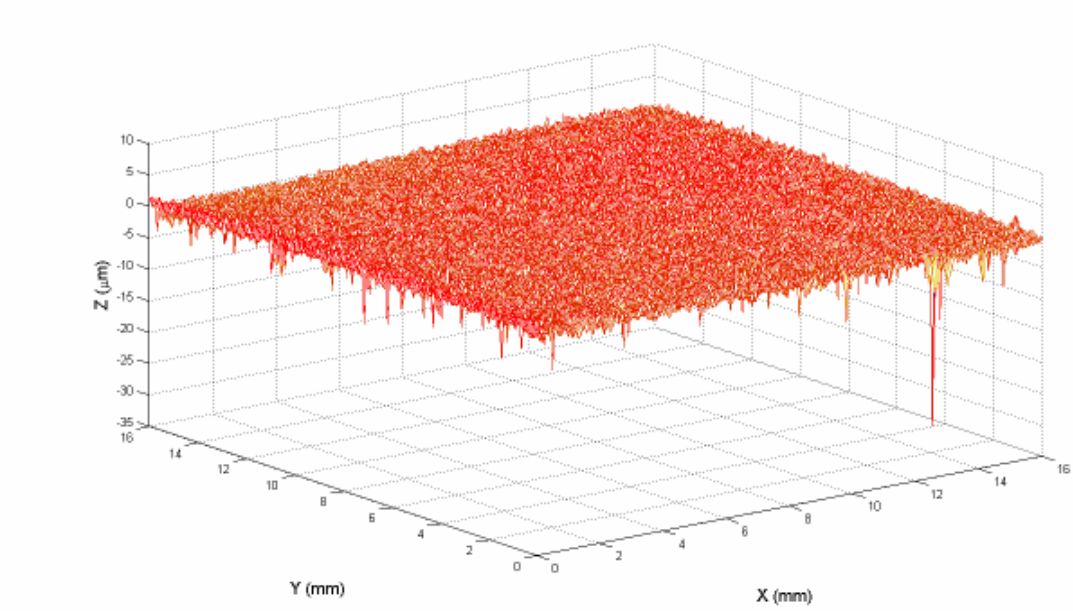

Figure 70: Surface scan of 600 grit stainless steel substrate after elevated temperature exposure at 500 °C.

REFERENCES

1. FuelCell Energy, I., *FuelCell Energy and U.S. Department of Energy Finalize Award to Develop Clean Coal-Fueled Multi-Megawatt Solid Oxide Fuel Cell System*. 2006, Business Wire.

2. Minh, N.Q., *Ceramic fuel cells.* Journal of the American Ceramic Society, 1993. **76**(3): p. 563-588.

3. "Hydrogren, Fuel Cells and Infrastructure Technologies Program - Fuel Cells." U.S. Department of Energy. 5 May 2005. <http://www1.eere.energy.gov/hydrogenandfuelcells/fuelcells/printable_versions/fc_types.html>

4. Minh, N.Q., *Solid oxide fuel cell technology - Features and applications.* Solid State Ionics, 2004. **174**(1-4): p. 271-277.

5. (U.S.), S.C.f.N.G., *Fuel Cell Handbook*. Seventh ed. 2002: Morgantown, W.Va. : U.S. Dept. of Energy, National Energy Technology Laboratory, Strategic Center for Natural Gas.

6. Singh, R.N., *High-temperature seals for Solid Oxide Fuel Cells (SOFC).* Journal of Materials Engineering and Performance, 2006. **15**(4): p. 422-426.

7. Chou, Y.-S. and J.W. Stevenson. *Compressive mica seals for solid oxide fuel cells*. in *Joining of Advanced and Specialty Materials VII, Oct 18-20 2004*. 2005. Columbus, OH, United States: ASM International, 9639 Kinsman Road, OH 44073-0002, United States.

8. Chou, Y.-S. and J.W. Stevenson, *Long-term thermal cycling of Phlogopite mica-based compressive seals for solid oxide fuel cells.* Journal of Power Sources, 2005. **140**(2): p. 340-5.

9. Chou, Y.-S. and J.W. Stevenson, *Novel infiltrated Phlogopite mica compressive seals for solid oxide fuel cells.* Journal of Power Sources, 2004. **135**(1-2): p. 72-8.

10. Chou, Y.-S. and J.W. Stevenson, *Phlogopite mica-based compressive seals for solid oxide fuel cells: effect of mica thickness.* Journal of Power Sources, 2003. **124**(2): p. 473-8.

11. Chou, Y.-S. and J.W. Stevenson, *Mid-term stability of novel mica-based compressive seals for solid oxide fuel cells.* Journal of Power Sources, 2003. **115**(2): p. 274-8.

12. Chou, Y.-s. and J.W. Stevenson, *Thermal cycling and degradation mechanisms of compressive mica-based seals for solid oxide fuel cells.* Journal of Power Sources, 2002. **112**(2): p. 376-83.

13. Chou, Y.-S. and J.W. Stevenson, *Novel silver/mica multilayer compressive seals for solid-oxide fuel cells: The effect of thermal cycling and material degradation on leak behavior.* Journal of Materials Research, 2003. **18**(9): p. 2243-2250.

14. Chou, Y.-S. and J.W. Stevenson, *Compressive mica seals for solid oxide fuel cells.* Journal of Materials Engineering and Performance, 2006. **15**(4): p. 414-421.

15. Chou, Y.-S., J.W. Stevenson, and L.A. Chick, *Novel compressive mica seals with metallic interlayers for solid oxide fuel cell applications.* Journal of the American Ceramic Society, 2003. **86**(6): p. 1003-7.

16. Chou, Y.-S., J.W. Stevenson, and L.A. Chick, *Ultra-low leak rate of hybrid compressive mica seals for solid oxide fuel cells.* Journal of Power Sources, 2002. **112**(1): p. 130-6.

17. Chou, Y.-S., J.W. Stevenson, and P. Singh, *Thermal cycle stability of a novel glass-mica composite seal for solid oxide fuel cells: Effect of glass volume fraction and stresses.* Journal of Power Sources, 2005. **152**: p. 168-74.

18. Chou, Y.-S., J.W. Stevenson, and P. Singh. *Combined ageing and thermal cycling of compressive mica seals for solid oxide fuel cells*. in *29th International Conference on Advanced Ceramics and Composites, 23-28 Jan. 2005 Ceramic Engineering and Science Proceedings*. 2005. Cocoa Beach, FL, USA: American Ceramic Soc.

19. Chou, Y.-S., J.W. Stevenson, and P. Singh. *Glass mica composite seals for solid oxide fuel cells*. in *29th International Conference on Advanced Ceramics and Composites, 23-28 Jan. 2005 Ceramic Engineering and Science Proceedings*. 2005. Cocoa Beach, FL, USA: American Ceramic Soc.

20. Simner, S.P. and J.W. Stevenson, *Compressive mica seals for SOFC applications.* Journal of Power Sources, 2001. **102**(1-2): p. 310-16.

21. Koeppel, B.J., et al. *Mechanical property characterizations and performance modeling of SOFC seals*. in *Advances in Solid Oxide Fuel Cells II. A Collection of Papers Presented at the 30th International Conference on Advanced Ceramics and Composites*. 2006. Cocoa Beach, FL, United States: American Ceramic Society, Westerville, OH 43081, United States.

22. Nguyen, B.N., et al. *On the nonlinear behavior of a glass-ceramic seal and its application in planar SOFC systems*. in *4th International ASME Conference on Fuel Cell Science, Engineering and Technology*. 2006. Irvine, CA, United States: American Society of Mechanical Engineers, New York, NY 10016-5990, United States.

23. Wuillemin, Z., et al. *Modeling and study of the influence of sealing on a solid oxide fuel cell*. in *EFC2005*. 2005. Rome, Italy: American Society of Mechanical Engineers, New York, NY 10016-5990, United States.

24. Jackson, R.L. and J.L. Streator, *A multi-scale model for contact between rough surfaces.* Wear, 2006. **261**(11-12): p. 1337-1347.

25. Etsion, I. and I. Front, *Model for static sealing performance of end face seals.* S T L E Tribology Transactions, 1994. **37**(1): p. 111-119.

26. Chou, Y.-S., et al., *Material degradation during isothermal ageing and thermal cycling of hybrid mica seals under solid oxide fuel cell exposure conditions.* Journal of Power Sources, 2006. **157**(1): p. 260-270.

27. Chou, Y.-S., J.W. Stevenson, and R.N. Gow, *Novel alkaline earth silicate sealing glass for SOFC. Part I. The effect of nickel oxide on the thermal and mechanical properties.* Journal of Power Sources, 2007. **168**(2): p. 426-433.

28. Chou, Y.-S., J.W. Stevenson, and R.N. Gow, *Novel alkaline earth silicate sealing glass for SOFC. Part II. Sealing and interfacial microstructure.* Journal of Power Sources, 2007. **170**(2): p. 395-400.

29. Patir, N. and H.S. Cheng, *Average flow model for determining effects of three-dimensioinal roughness on partial hydrodynamic lubrication.* 1978. **100**(1): p. 12-17.

30. Tripp, J.H., *Surface roughness effects in hydrodynamic lubrication: the flow factor method.* . 1983. **105**(3): p. 458-465.

31. Teale, J.L. and A.O. Lebeck, *An evaluation of the average flow model for surface roughness effects in lubrication.* Transactions of the ASME. Journal of Lubrication Technology, 1980. **102**(3): p. 360-6.

32. Tonder, K., *Simulation of the lubrication of isotropically rough surfaces.* ASLE Transactions, 1980. **23**(3): p. 326-33.

33. Yuanzhong, H. and Z. Lingqing, *Some aspects of determining the flow factors.* Journal of Tribology, Transactions of the ASME, 1989. **111**(3): p. 525-531.

34. Elrod, H.G., *A general theory for laminar lubrication with Reynolds roughness.* Transactions of the ASME. Journal of Lubrication Technology, 1979. **101**(1): p. 8-14.

35. Peeken, H.J., et al. *On the numerical determination of flow factors*. 1996. San Francisco, CA, USA: ASME, New York, NY, USA.

36. Etsion, I. and I. Front, *A Model for Static Sealing Performance of End Face Seals.* S T L E Tribology Transactions, 1993. **37**(1): p. 111-119.

37. Polycarpou, A.A. and I. Etsion, *A Model for the Static Sealing Performance of Compliant Metallic Gas Seals Including Surface Roughness and Rarefaction Effects.* Tribology Transactions, 1999. **43**(2): p. 237-244.

38. Ruan, B., R.F. Salant, and I. Green, *A Mixed lubrication model of liquid/gas mechanical face seals.* Tribology Transactions, 1997. **40**(4): p. 647-657.

39. Harp, S.R. and R.F. Salant, *An average flow model of rough surface lubrication with inter-asperity cavitation.* Journal of Tribology, 2001. **123**(1): p. 134-143.

40. Harp, S.R. and R.F. Salant, *Inter-asperity cavitation and global cavitation in seals: An average flow analysis.* Tribology International, 2002. **35**(2): p. 113-121.

41. Greenwood, J.A. and J.B.P. Williamson, *Contact of Nominally Flat Rough Surfaces.* Proceedings of the Royal Society of London, 1966. **A295**: p. 300-319.

42. Jackson, R.L. and J.L. Streator, *A multi-scale model for contact between rough surfaces.* Wear, 2006. **261**(11-12): p. 1337-47.

43. Green, C.K., J.L. Streator, and C. Haynes. *Modeling Leakage with Mica-Based Compressive Seals For Solid Oxide Fuel Cells*. in *International Mechanical Engineering Conference and Exposition 2006*. 2006. Chicago , IL: ASME.

44. Pao, Y.-H., et al., *A Note on the Implementation of Temperature Dependent Coefficient of Thermal Expansion (CTE) in ABAQUS.* Journal of Electronic Packaging, 1992. **114**(4): p. 470-472.

45. Whitehouse, D.J. and J.F. Archard, *The properties of random surface of significance in their contact.* Proceedings of the Royal Society of London, 1970. **316**(1524): p. 97-121.

46. McCool, J.I., *COMPARISON OF MODELS FOR THE CONTACT OF ROUGH SURFACES.* Wear, 1986. **107**(1): p. 37-60.

47. Persson, B.N.J., *Theory of rubber friction and contact mechanics.* Journal of Chemical Physics, 2001. **115**(8): p. 3840-61.

48. Majumdar, A. and B. Bhushan, *Role of fractal geometry in roughness characterization and contact mechanics of surfaces.* Journal of Tribology, 1990. **112**(2): p. 205-216.

49. Zilberman, S. and B.N.J. Persson, *Nanoadhesion of elastic bodies: roughness and temperature effects.* Journal of Chemical Physics, 2003. **118**(14): p. 6473-80.

50. Chang, W.R., I. Etsion, and D.B. Bogy, *An Elastic-Plastic Model for the Contact of Rough Surfaces.* Journal of Tribology 1987. **109**(2): p. 257-63.

51. Dong, W.P., P.J. Sullivan, and K.J. Stout, *Comprehensive study of parameters for characterising three- dimensional surface topography: III: Parameters for characterising amplitude and some functional properties.* Wear, 1994. **178**(1-2): p. 29-43.

52. Westergaard, H.M., *Bearing Pressures and Cracks.* Journal of Applied Mechanics, 1939. **6**(2): p. 49-53.

53. Johnson, K.L., J.A. Greenwood, and J.G. Higginson, *The Contact of Elastic Regular Wavy Surfaces.* International Journal of Mechanical Sciences, 1985. **27**(6): p. 383-396.

54. Hamrock, B.J., S.R. Schmid, and B.O. Jacobson, *Fundamentals of fluid film lubrication* 2nd ed. 2004, New York Marcel Dekker, c2004. 699.

55. Krithivasan, V. and R.L. Jackson, *An analysis of three-dimensional elasto-plastic sinusoidal contact.* Tribology Letters, 2007. **27**(1): p. 31-43.

56. Kogut, L. and I. Etsion, *Elastic-plastic contact analysis of a sphere and a rigid flat.* Journal of Applied Mechanics, 2002. **69**(5): p. 657-662.

57. Schweitzer, P.A., *Metallic materials : physical, mechanical, and corrosion properties*. 2003, New York: M. Dekker. 702.

58. Stubbins, J.F., et al., *The role of deformation mechanisms in flow localization of 316L stainless steel.* Journal of Nuclear Materials, 2006. **356**(1-3): p. 70-7.

59. Greenwood, J.A. and J.H. Tripp, *The contact of two nominally flat rough surfaces.* Proceedings of the Institution of Mechanical Engineers, 1970. **185**(48): p. 625-33.

60. Jackson, R., I. Chusoipin, and I. Green, *A finite element study of the residual stress and deformation in hemispherical contacts.* Journal of Tribology, 2005. **127**(3): p. 484-493.

61. Makino, T., S. Morohoshi, and S. Taniguchi, *Application of average flow model to thin film gas lubrication.* Journal of Tribology, Transactions of the ASME, 1993. **115**(1): p. 185-190.

62. Chapkov, A.D., C.H. Venner, and A.A. Lubrecht, *Roughness amplitude reduction under non-Newtonian EHD lubrication conditions.* Journal of Tribology, Transactions of the ASME, 2006. **128**(4): p. 753-760.

63. Venner, C.H. and A.A. Lubrecht, *An engineering tool for the quantitative prediction of general roughness deformation in EHL contacts based on harmonic waviness attenuation.* Proceedings of the Institution of Mechanical Engineers, Part J: Journal of Engineering Tribology, 2005. **219**(5): p. 303-312.

VITA

Christopher Green, son of Beatrice and the Reverend Timothy R. Green Jr, was born in Decatur, GA in 1978. He grew up in Augusta, GA, and was the 1996 Valedictorian of George P. Butler Comprehensive High School. After being recognized as the Most Outstanding Dual Degree Engineering Program graduate in 2001, he received a Bachelor of Science in Mathematics from Morehouse College, and a Bachelor of Science in Mechanical Engineering from the Georgia Institute of Technology. Subsequent to graduation, he received several fellowships to pursue his doctoral Degree, and ultimately decided to return to Georgia Tech to pursue a Masters and Ph.D. under the guidance of Dr. Jeffrey Streator and Dr. Comas Haynes with an emphasis on contact mechanical modeling.